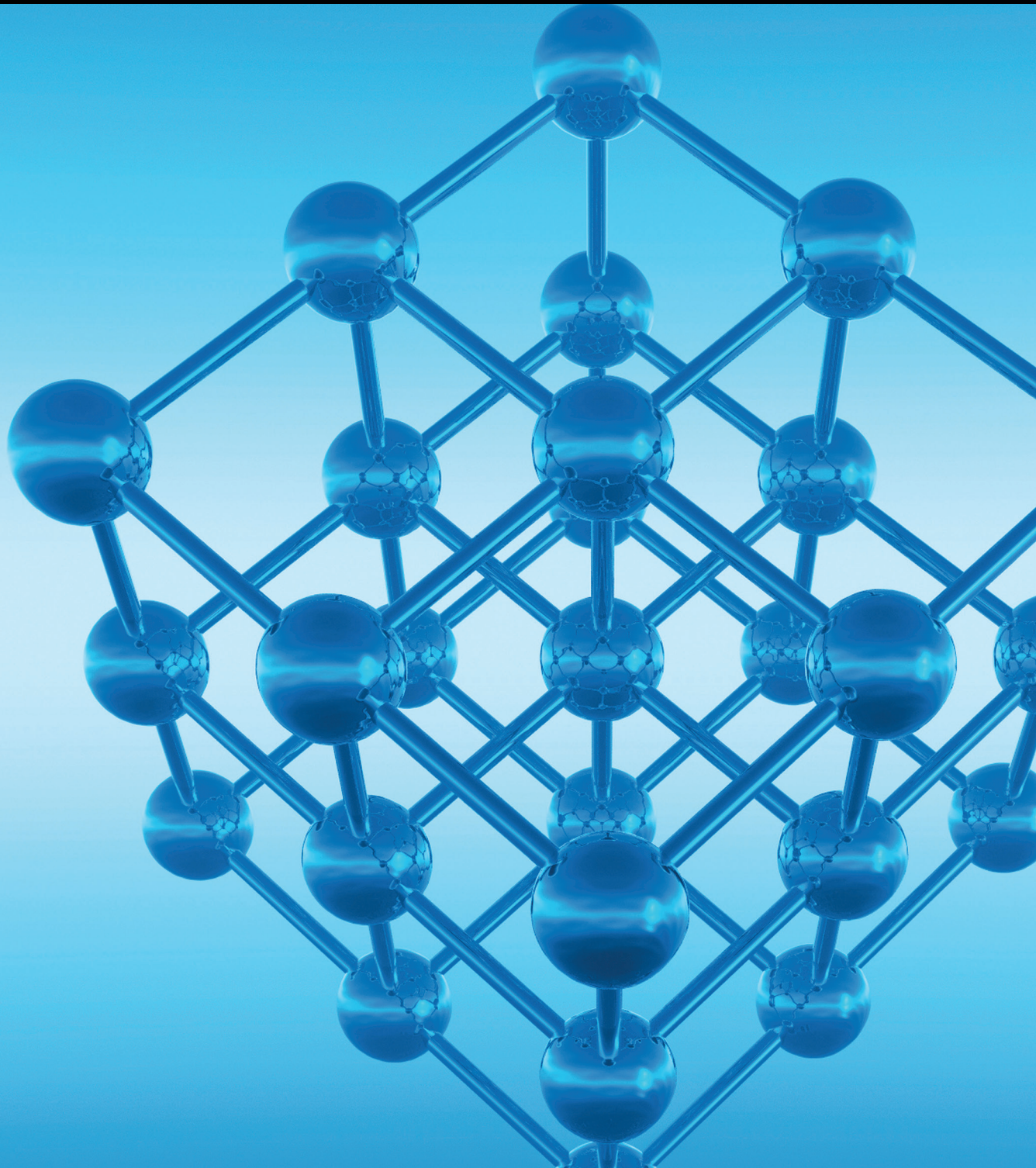


Advances in Condensed Matter Physics

Defects in Solid-State Physics

Guest Editors: Haiyan Xiao, Liang Qiao, Xia Xiang, and Safdar Nazir





Defects in Solid-State Physics

Advances in Condensed Matter Physics

Defects in Solid-State Physics

Guest Editors: Haiyan Xiao, Liang Qiao, Xia Xiang,
and Safdar Nazir



Copyright © 2013 Hindawi Publishing Corporation. All rights reserved.

This is a special issue published in “Advances in Condensed Matter Physics.” All articles are open access articles distributed under the Creative Commons Attribution License, which permits unrestricted use, distribution, and reproduction in any medium, provided the original work is properly cited.

Editorial Board

Dario Alfe, UK
Bohdan Andraka, USA
Daniel Arovas, USA
Veer P. S. Awana, India
Arun Bansil, USA
Ward Beyermann, USA
Golam M. Bhuiyan, Bangladesh
Rudro R. Biswas, USA
Luis L. Bonilla, Spain
Gang Cao, USA
Ashok Chatterjee, India
Ram N. P. Choudhary, India
Kim Chow, Canada
Oleg Derzhko, Ukraine
Hiromi Kitahara Eba, Japan
Gayanath Fernando, USA

Jörg Fink, Germany
Yuri Galperin, Norway
Russell Giannetta, USA
James L. Gole, USA
Prasenjit Guptasarma, USA
Da-Ren Hang, Taiwan
Yurij Holovatch, Ukraine
Chia-Ren Hu, USA
David Huber, USA
Johannes Jobst, Netherlands
Jan A. Jung, Canada
Feo V. Kusmartsev, UK
Rosa Lukaszew, USA
Victor V. Moshchalkov, Belgium
Vladimir A. Osipov, Russia
Rolfe Petschek, USA

Joseph S. Poon, USA
Ruslan Prozorov, USA
Leonid Pryadko, USA
Charles Rosenblatt, USA
Omid Saremi, Canada
Mohindar S. Seehra, USA
Sergei Sergeenkov, Brazil
Daniel L. Stein, USA
Michael C. Tringides, USA
Sergio E. Ulloa, USA
Attila Virosztek, Hungary
Markus R. Wagner, Germany
Gary Wysin, USA
Kiyokazu Yasuda, Japan
Fajun Zhang, Germany

Contents

Modelling of Dual-Junction Solar Cells including Tunnel Junction, Abdelaziz Amine, Yamina Mir, and Mimoun Zazoui
Volume 2013, Article ID 546362, 5 pages

Electrical Properties of Amorphous Titanium Oxide Thin Films for Bolometric Application, Yongfeng Ju, Mahua Wang, Yunlong Wang, Shihu Wang, and Chengfang Fu
Volume 2013, Article ID 365475, 5 pages

Surface-Assisted Luminescence: The PL Yellow Band and the EL of n-GaN Devices, José Ignacio Izpura
Volume 2013, Article ID 597265, 10 pages

Electronic Structure Calculations of $A_2Ti_2O_7$ (A = Dy, Ho, and Y), H. Y. Xiao
Volume 2013, Article ID 675410, 8 pages

Catalytic Mechanism of Pd Adsorption on S-Terminated GaAs(001)-(2 × 6) Surface, Deng-feng Li, Zhi-cheng Guo, Bo-Lin Li, and Ming Luo
Volume 2013, Article ID 130868, 4 pages

Low-Resistivity p-Type Doping in Wurtzite ZnS Using Codoping Method, Deng-Feng Li, Min Luo, Bo-Lin Li, Cheng-Bing Wu, Bo Deng, and Hui-Ning Dong
Volume 2013, Article ID 739078, 4 pages

Studies on AC Electrical Conductivity of CdCl₂ Doped PVA Polymer Electrolyte, M. B. Nanda Prakash, A. Manjunath, and R. Somashekar
Volume 2013, Article ID 690629, 6 pages

Research Article

Modelling of Dual-Junction Solar Cells including Tunnel Junction

Abdelaziz Amine, Yamina Mir, and Mimoun Zazoui

Laboratory of Condensed Matter and renewable energy, University Hassan II Mohammedia-Casablanca, Faculty of Sciences and Techniques, BP 146, Boulevard Hassan II, Mohammedia 28800, Morocco

Correspondence should be addressed to Mimoun Zazoui; zazouimimoun@yahoo.fr

Received 8 May 2013; Revised 5 August 2013; Accepted 15 August 2013

Academic Editor: Xia Xiang

Copyright © 2013 Abdelaziz Amine et al. This is an open access article distributed under the Creative Commons Attribution License, which permits unrestricted use, distribution, and reproduction in any medium, provided the original work is properly cited.

Monolithically stacked multijunction solar cells based on III-V semiconductors materials are the state-of-art of approach for high efficiency photovoltaic energy conversion, in particular for space applications. The individual subcells of the multi-junction structure are interconnected via tunnel diodes which must be optically transparent and connect the component cells with a minimum electrical resistance. The quality of these diodes determines the output performance of the solar cell. The purpose of this work is to contribute to the investigation of the tunnel electrical resistance of such a multi-junction cell through the analysis of the current-voltage (J - V) characteristics under illumination. Our approach is based on an equivalent circuit model of a diode for each subcell. We examine the effect of tunnel resistance on the performance of a multi-junction cell using minimization of the least squares technique.

1. Introduction

Currently, multijunction III-V solar cells have the highest solar cell energy conversion efficiencies (40%) [1, 2], and they are still under investigation for even higher values. Stacked p-n junctions with different band gap energies, such as dual junctions GaInP/GaAs, can pave the way for the solar spectrum efficiently. In a multijunction solar cell, the subcells are interconnected through tunnel junctions [3, 4], in order to align Fermi levels. These tunnel junctions must have a low electrical resistivity [5–8], a high optical transmission, and a high peak tunnelling current density [4, 9, 10].

Due to the complexity of the electrical and optical interaction between different layers [11, 12], pure experimental optimization of these structures is expensive and time consuming. A suitable simulation is desirable to help accelerating the experimental optimization. During simulation, different physical processes beyond the standard drift equations of electrical transport have to be considered as follows: existence of hetero-interfaces and interference effects. These processes have been partly implemented in most of simulation programs. There exist commercial semiconductor simulation programs which give excellent results

for modelling single-junction solar cell [3, 8]. However, taking into consideration the mentioned physical process, a correction of description for the series interconnection of individual subcells must be included [5, 6, 13].

The current-voltage (J - V) characteristic under illumination is the most important parameter of any solar cell [5, 7, 14]. This characteristic allows determining the parameters of the cell and thus predicting its performances. This is done by fitting the illumination (J - V) curve into a model containing the parameters.

There are two basic models to describe the J - V characteristics of a solar cell: a simple one, which considers the solar cell as a single p-n junction diode with parasitic resistances, and a more elaborated model which takes into account the recombination centres present in the solar cell junction.

There are several methods to extract the solar cell parameters. A relatively simple one exists to estimate the series and shunt resistances of the cell using the slope of the current-voltage (J - V) curve in conditions of open-circuit voltage and short-circuit current, respectively. Other methods use complicated numerical analysis based on Lambert's W function, calculating the resistance from the difference between the diode characteristics in dark and under illumination

[15]. These methods necessitate accurate extraction of many parameters from a nonlinear equation. In most cases, the ideality factor is assumed to be equal to 1 (i.e., the parallel resistance is neglected) so that all parameters cannot be properly extracted. Moreover, in most studies, the (J - V) characteristics obtained from the extracted parameters are not compared with the measured (J - V) ones, making it difficult to evaluate the accuracy of the methods.

In this work, we present a method to extract the parameters of a dual junction solar cell, that is, including a tunnel junction. It uses the one diode model [16]. Taking into consideration current matching between subcells, we derive the analytical expression of the J - V curve using Lambert's W function. As approximation, we neglect the series resistance of each subcell, considering only the tunnel resistance r_{tun} .

The objective of this work is to compare the J - V characteristics derived from these parameters with experiment data available in the literature [7] in order to test the validity of our procedure. Then, we apply our method to extract different parameters of dualjunction such as the tunnel resistance of a particular cell.

2. Modelling a J - V Dual Junction

Introduction of tunnel junctions between subcells is the way of monolithically building a multijunction solar cell. These tunnel junctions must cause minimum losses of the conversion efficiency. This implies that they exhibit a low series resistance and a minimum optical absorption. A tunnel junction diode is a diode made of a wide band gap, highly doped material. This reduces the length of the depletion region so that electrons can easily tunnel through (the tunnel effect) [17].

In order to identify the relationship between the quality of a tunnel junction and the semiconductor parameters used to design its structure, necessary simplifications will be used. We employ the one exponential model, taking only the recombination current term into account. The tunnel junction will be considered ideal, meaning that it will always work in the ohmic region and its behaviour can be modelled as a voltage drop which depends linearly on the current flowing through it [18].

To calculate the J - V curve of GaInP/GaAs dual junction including AlGaAs tunnel junction, we start from the expressions for the voltages at each junction for a given current. In this case, both subcells in the dual junction solar cell are connected in a series configuration, and the device is accessed through two terminals, as shown schematically in Figure 1. The voltage at the whole dual-junction solar cell is given by

$$V_{\text{dual}} = V_{\text{top}} + V_{\text{tun}} + V_{\text{bot}}, \quad (1)$$

where V_{top} , V_{bot} , and V_{tun} are the voltages at GaInP top cell, GaAs bottom cell, and AlGaAs tunnel junction respectively.

The currents flowing through the two subcells as well as the tunnel diode are assumed to be current matched [10]; that is, the photogenerated current in both subcells is considered to be of equal value. It is determined by the subcell, delivering the lowest current, again that

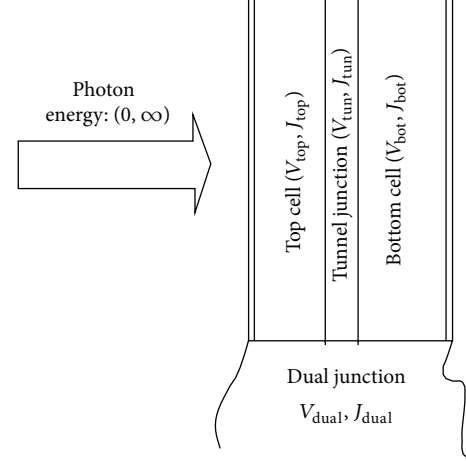


FIGURE 1: Scheme of the two terminals, of dual-junction solar cell.

the importance of the current matching is evident, the maximum efficiency (η) and the fill factor (FF)—that is, cells with a high fill factor, have a low equivalent series resistance and a high equivalent shunt resistance, and consequently the series and shunt resistances of each subcell top and bottom are neglected [5, 8, 9]. With these conditions, an analytical expression for the illumination J - V characteristic of the dual-junction solar cell can be developed. The general one-exponential model for each subcell [9] which is going to be used is as follows:

$$J = J_L - J_0 \exp\left(\frac{V - r_s J}{V_t}\right) \quad \text{where } V_t = \frac{k_B T}{q}, \quad (2)$$

where J_0 , J_L are saturation current density and photogenerated current density, respectively, r_s is series resistance, q is the charge, V is the bias voltage, k_B is the Boltzmann constant, and T is the temperature.

The voltages at each subcell and tunnel junction are as follows

$$\begin{aligned} V_{\text{top}} &= r_{\text{top}} \cdot J_{\text{top}} + V_t \ln\left(\frac{J_L^{\text{top}} - J_{\text{top}}}{J_0^{\text{top}}}\right), \\ V_{\text{bot}} &= r_{\text{bot}} \cdot J_{\text{bot}} + V_t \ln\left(\frac{J_L^{\text{bot}} - J_{\text{bot}}}{J_0^{\text{bot}}}\right), \\ V_{\text{tun}} &= r_{\text{tun}} \cdot J_{\text{tun}}. \end{aligned} \quad (3)$$

Since the current density through both subcells must be of equal value and assuming that the subcells are current matched at $T = 300$ K,

$$J_{\text{top}} = J_{\text{bot}} = J_{\text{tun}} = J_{\text{dual}}. \quad (4)$$

We neglect the series resistance of each subcell and consider only the tunnel resistance r_{tun} .

Hence, the expression of the current density of dual junction is

$$J_{\text{dual}} = J_L - \sqrt{J_0^{\text{top}} \cdot J_0^{\text{bot}}} \exp\left(\frac{V_{\text{dual}} - r_{\text{tun}} J_{\text{dual}}}{2V_t}\right). \quad (5)$$

This expression is similar to the general form of the single junction solar cell one exponential model, but using the geometric average of the recombination currents as the exponential prefactor and introducing a factor 2 in the denominator of the exponential term.

Accordingly, the open circuit voltage is

$$V_{OC} = 2V_t \ln \left(\frac{J_L}{\sqrt{J_{0top} \cdot J_{0bot}}} \right), \quad (6)$$

$$V_{OC} = V_{OCtop} + V_{OCbot},$$

where V_{OCtop} and V_{OCbot} are the open circuit voltages of each subcell top and bottom, respectively.

And short circuit current can be derived as follows:

$$J_{sc} = J_L - \sqrt{J_{0top} \cdot J_{0bot}} \exp \left(\frac{J_{sc} \cdot r_{tun}}{2V_t} \right). \quad (7)$$

From (5), the current J_{dual} can be derived as follows:

$$J_{dual} = \left(r_{tun} J_L + 2V_t \cdot \text{Lambert } W \right. \\ \left. \times \left(-\frac{\sqrt{J_{0top} J_{0bot}} \cdot r_{tun}}{2V_t} \exp \left(-\frac{-V_{dual} + r_{tun} J_L}{2V_t} \right) \right) \right) \\ \times (r_{tun})^{-1}. \quad (8)$$

The purpose of algorithm is to fit a nonlinear characteristic J - V (8) which suits the given data appropriately and subscribes to the minimization of the sum of the squared differences between the actual data and the predicted one. The error ε thus is defined as

$$\varepsilon = \sum_{i=1}^N (J_i - J(V_i, p))^2, \quad (9)$$

where N is the number of measured $J(V)$ pairs denoted by (V_i, J_i) ; $J(V, p)$ is the theoretical current for voltage V as predicted by a model containing several parameters, represented by p , that are the variables used to minimize the error.

Being put into effect with Matlab Software, we have shown the experimental data and simulation J - V characteristic under illumination of the dual-junction solar cell using the one-diode model program to extract the important features parameters of each subcell (top and bottom) such as recombination current J_{0top} , J_{0bot} and resistance tunnel r_{tun} (so as to give more information about the electrical performance dual junction) restricted solely in domain boundaries definition. For so doing, we have chosen the minimum and maximum limit: $L_b < p < U_b$ with $p = (J_{0top}, J_{0bot}, r_{tun})$.

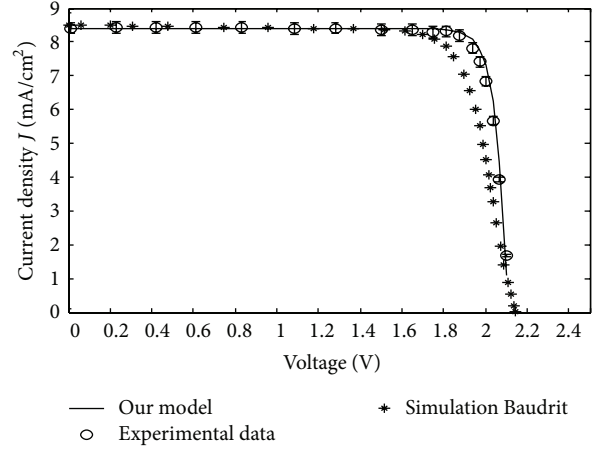


FIGURE 2: The experimental and simulation data for dual junction current density versus voltage. Circles correspond to experimental data, stars to results of Baudrit and Algora [7] and line to our model.

3. Analysis of Experimental Data

We applied our model to results given by Baudrit and Algora [7]. The sample consists of GaInP/GaAs dual solar cell in presence of a p^{++} GaAs- n^{++} GaAs tunnel junction. Parameters of the one-diode model were extracted using a program that employed the iterative method. Matlab was used to create a program that made use of a user-defined parameter initialization scheme to set the boundaries of the iteration and minimize computing time. The algorithm used to extract the parameters such as the resistance tunnel r_{tun} of the one-diode model utilized both approximations and iterative techniques.

In Figure 2, we show the measured and simulated J - V characteristic under illumination of the dual solar cell using the one-diode model parameter extraction program. We can see clearly that the curve from our model fit very well the experimental data in comparison with the simulation [7]. Consequently, simulation is not taken into consideration the resistance tunnel r_{tun} .

In Table 1, we give the values of the characteristics of the dual junction compared with experience and simulation. The parameters J_{max} and V_{max} are the maximum current density and voltage, respectively.

The obtained parameters are in good accordance with the growth condition and technological process data [7, 12, 17]. Unlike precedent research conducted on this ground [7], we have come up with method for extracting the resistance tunnel r_{tun} , the recombination current density J_{0top} and J_{0bot} .

In order to validate our model, we analyse dual-junction solar cell including tunnel junction, the sample consists of GaInP/GaAs on Ge substrate grown by MOCVD, which is n^+ (emitter) on p (base) structures. The AlInP windows are n -type doped at level of $7 \times 10^{18} \text{ cm}^{-3}$. The GaAs and GaInP emitters and bases, respectively, doped at $1 \times 10^{18} \text{ cm}^{-3}$ and $3 \times 10^{17} \text{ cm}^{-3}$. The dopants are Si(n) and C(n) in AlGaAs tunnel junction and Si(n) and Zn(p) in GaAs and GaInP. The GaInP and GaAs are, respectively, 500 nm and 3, 15 μm thick.

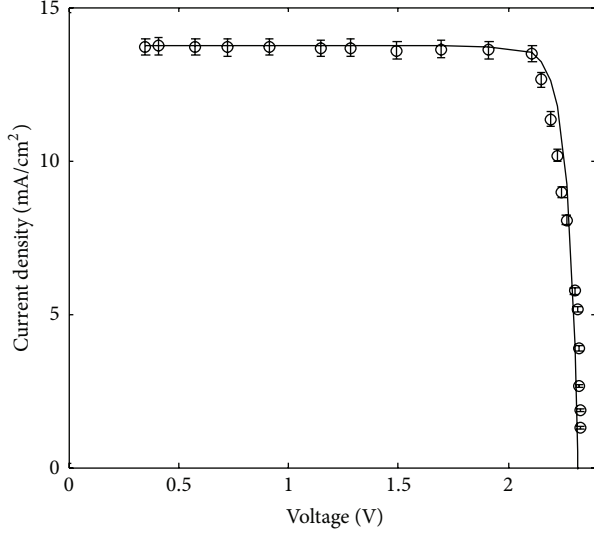


FIGURE 3: Experimental data (circle) and simulated (continuous line) for dual junction GaInP/GaAs.

TABLE 1: Parameters extracted from the experience and simulation by Baudrit and Algora [7] and comparison with our extracted parameters.

Parameters	Experience [7]	Baudrit and Algora [7]	Our model
J_{sc} ($\text{mA}\cdot\text{cm}^{-2}$)	8.4	8.4	8.4
V_{oc} (V)	2.12	2.12	2.12
J_{max} ($\text{mA}\cdot\text{cm}^{-2}$)	7.9	7.66	8.06
V_{max} (V)	1.9	1.82	1.94
FF (%)	84	78	87.8
η	15	13.9	15.63
$J_{0\text{top}}$ ($\text{mA}\cdot\text{cm}^{-2}$)	—	—	6.72×10^{-21}
$J_{0\text{bot}}$ ($\text{mA}\cdot\text{cm}^{-2}$)	—	—	4.72×10^{-14}
r_{tun} ($\Omega\cdot\text{cm}^2$)	—	—	4.9×10^{-4}

TABLE 2: Parameters extracted from our model and comparison with experience.

Parameters	Experience	Our model
J_{sc} (mA/cm^2)	13.73	13.73
V_{oc} (V)	02.32	02.32
J_{max} (mA/cm^2)	13.49	13.50
V_{max} (V)	02.11	02.12
FF (%)	89.34	89.84
η	28.46	28.62
$J_{0\text{top}}$ (mA/cm^2)	—	4.60×10^{-23}
$J_{0\text{bot}}$ (mA/cm^2)	—	4.83×10^{-15}
r_{tun} ($\Omega\cdot\text{cm}^2$)	—	4.48×10^{-4}

In Figure 3, we show the experimental data and simulation J - V characteristic under illumination of the dual-junction solar cell using the one-diode model program to extract the important features of each subcell. In Table 2,

we give the values of the characteristics of the dual junction compared with experience.

In Table 2, resuming the main characteristics of dual junction at 1 Sun, the simulation shows a very good fit with the experimental data on the J - V prediction. Further, we have come up with other extractions of each subcells (top and bottom) precisely $J_{0\text{top}}$ and $J_{0\text{bot}}$ and r_{tun} which intersect with other researchers' findings [7, 18].

4. Conclusion

Based on a modelling of dual-junction solar cells including tunnel junction and J - V characterization of multijunction, solar cells were established and applied to semiconductor junctions and devices. In this work, we have given much importance to extract the parameters which are characteristics of the dual junction, using the simulation through fitting by Matlab software. Measurements have been carried on double junction III-V solar cells (GaInP/GaAs) including the AlGaAs tunnel junction, and results have been exploited to extract the parameters to give more information about the electrical performance of dual junction.

References

- [1] R. R. King, D. C. Law, K. M. Edmondson et al., "40% efficient metamorphic GaInP/GaInAsGe multijunction solar cells," *Applied Physics Letters*, vol. 90, no. 18, Article ID 183516, 2007.
- [2] W. Guter, F. Dimroth, M. Meusel, and A. W. Bett, "Tunnel diodes for III-V multi-junction solar cells," in *Proceedings of the 20th European Photovoltaic Solar Energy Conference*, pp. 515–518, Barcelona, Spain, June 2005.
- [3] G. Letay, M. Hermle, and A. W. Bett, "Simulating single-junction GaAs solar cells including photon recycling," *Progress in Photovoltaics*, vol. 14, no. 8, pp. 683–696, 2006.
- [4] G. A. M. Hurkx, D. B. M. Klaassen, and M. P. G. Knuvers, "A new recombination model for device simulation including tunneling," *IEEE Transactions on Electron Devices*, vol. 39, no. 2, pp. 331–338, 1992.
- [5] T. Takamoto, M. Yamaguchi, and E. Ikeda, "Mechanism of Zn and Si diffusion from a highly doped tunnel junction for InGaP/GaAs tandem solar cells," *Journal of Applied Physics*, vol. 85, no. 3, p. 14816, 1999.
- [6] I. Garcia, I. Rey-Stolle, B. Galiana, and C. Algora, "A 32.6% efficient lattice-matched dual-junction solar cell working at 1000 suns," *Applied Physics Letters*, vol. 94, no. 5, Article ID 053509, 2009.
- [7] M. Baudrit and C. Algora, "Modeling of GaInP/GaAs dual-junction solar cells including tunnel junction," in *Proceedings of the 33rd IEEE Photovoltaic Specialists Conference (PVSC '08)*, pp. 1–5, May 2008.
- [8] H. Shivaganaik and S. H. Jangamshetti, "Modeling and analysis of multi-junction solar cells," in *Proceedings of the International Conference on Emerging Trends in Electrical and Computer Technology (ICETECT '11)*, pp. 174–179, March 2011.
- [9] S. M. Sze, *Semiconductor Devices, Physics and Technology*, John Wiley & Sons, New York, NY, USA, 2nd edition, 2001.
- [10] M. Hermle, S. P. Philipps, G. Letay, and A. W. Bett, "Numerical simulation of tunnel diodes and multi-junction solar cells," in

- Proceedings of the 33rd IEEE Photovoltaic Specialists Conference*, pp. 1–4, San Diego, Calif, USA, 2008.
- [11] M. Baudrit, C. Algora, I. Rey-Stolle, I. García, and B. Galiana, “Numerical analysis of GaInP solar cells: toward advanced photovoltaic devices modeling,” in *Proceedings of the 5th International Conference on Numerical Simulation of Optoelectronic Devices*, pp. 41–42, Berlin, Germany, September 2005.
- [12] S. Adachi, *Properties of Group-IV, III-V and II-VI Semiconductors*, John Wiley & Sons, Chichester, UK, 2009.
- [13] F. Dimroth, U. Schubert, A. W. Bett et al., “Next generation GaInP/GaInAs/Ge multi-junction space solar cells + Fig1, Fig2,” in *Proceedings of the 17th European Space Power Conference*, 2001.
- [14] S. P. Philipps, W. Guter, E. Welsler et al., “Present status in the development of III–V multi-junction solar cells,” in *Next Generation of Photovoltaics*, vol. 165 of *Springer Series in Optical Sciences Volume*, pp. 1–21, 2012.
- [15] Z. Ouennoughi and M. Chegaar, “Simpler method for extracting solar cell parameters using the conductance method,” *Solid-State Electronics*, vol. 43, no. 11, pp. 1985–1988, 1999.
- [16] M. Chegaar, Z. Ouennoughi, F. Guechi, and H. Langueur, “Determination of solar cells parameters under illuminated conditions,” *Journal of Electron Devices*, vol. 2, pp. 17–21, 2003.
- [17] Z. Q. Li and S. Li, “Sophisticated models replicate the effects of tunnel junctions,” *Compound Semiconductor*, vol. 13, no. 6, pp. 29–31, 2007.
- [18] J. F. Wheeldon, C. E. Valdivia, A. Walker et al., “AlGaAs tunnel junction for high efficiency multi-junction solar cells: simulation and measurement of temperature-dependent operation,” in *Proceedings of the 34th IEEE Photovoltaic Specialists Conference (PVSC '09)*, pp. 000106–000111, June 2009.

Research Article

Electrical Properties of Amorphous Titanium Oxide Thin Films for Bolometric Application

Yongfeng Ju, Mahua Wang, Yunlong Wang, Shihu Wang, and Chengfang Fu

Faculty of Electronic and Electrical Engineering, Huaiyin Institute of Technology, Huaian 223003, China

Correspondence should be addressed to Yongfeng Ju; yfju_ha@163.com

Received 1 August 2013; Accepted 15 October 2013

Academic Editor: Xia Xiang

Copyright © 2013 Yongfeng Ju et al. This is an open access article distributed under the Creative Commons Attribution License, which permits unrestricted use, distribution, and reproduction in any medium, provided the original work is properly cited.

We report the electrical conduction mechanism of amorphous titanium oxide thin films applied for bolometers. As the O/Ti ratio varies from 1.73 to 1.97 measured by rutherford backscattering spectroscopy, the resistivity of the films increases from 0.26 Ω cm to 10.1 Ω cm. At the same time, the temperature coefficient of resistivity and activation energy vary from -1.2% to -2.3% and from 0.09 eV to 0.18 eV, respectively. The temperature dependence of the electrical conductivity illustrates a thermally activated conduction behavior and the carrier transport mechanism in the titanium oxide thin films is found to obey the normal Meyer-Neldel Rule in the temperature range from 293 K to 373 K.

1. Introduction

Titanium dioxide (TiO_2) is one of the most widely studied transition metal oxide semiconductors due to its nontoxic nature, chemical stability, and commercial availability at a low cost, robust, and general reactivity. During the past decades, TiO_2 thin films have attracted much interest because it has a wide range of promising energy and environmental applications, such as hydrogen generation by water splitting [1], photocatalytic water purification [2], dye-sensitized solar cells [3], and gas sensors [4]. Recently, few people have fabricated amorphous nonstoichiometric titanium dioxide, (a-TiO_x , where x is smaller than 2) thin films by different methods and pointed out that a-TiO_x thin films are potential thermal sensing material for an uncooled IR bolometer imager [5]. However, the effect of the deposition process on the film structure, composition and electrical properties of this material such as resistivity, temperature coefficient of resistivity (TCR), and activation energy, have not been illustrated up to now, and these factors are very crucial for the detectivity of thermal IR detectors.

TiO_x thin films can be prepared by sol-gel [6], hydrothermal [7], chemical and physical vapor deposition [8]. Reactive sputtering is a commonly used physical vapor deposition method to grow dense and uniform metal oxide films for

industrial application [9, 10]. In this process, a metal target is sputtered in an atmosphere consisting of argon and oxygen, this allows higher deposition rates than does the sputtering of an oxide target [10]. It has been experimentally established that the oxygen partial pressure (p_{O_2}) during sputtering has the most significant effect on the structure, phase composition, and electrical properties of TiO_x thin films [11].

TiO_2 is electrically insulating with an extremely high resistivity above $10^8 \Omega$ cm, but the suboxidized TiO_2 with an excess of titanium is an n type semiconductor with unique properties [12], indicating the defect disorder and O/Ti stoichiometry play an important role in the electrical properties of TiO_x [13]. In this work, we have mainly investigated the electrical properties and electron transport mechanism of a-TiO_x thin films applied for uncooled IR thermal detectors.

2. Experimental

TiO_x thin films were deposited on K9 glass and p-silicon (100) substrates simultaneously at room temperature by a dc reactive sputtering technique. Oxygen and argon were used as reactive gas and sputtering gas, respectively. The total pressure was kept at 1 Pa and the other characteristic parameters of the investigated samples are summarized in Table 1.

TABLE 1: Experimental parameters of reactive sputtering and the results of measurements. (SCCM is an abbreviation of standard cubic centimeter per minute).

Samples	Ar (SCCM)	O ₂ /(O ₂ + Ar) (pO ₂)	Thickness <i>d</i> (nm)	O/Ti ratio	Resistivity ρ (Ω cm)	Conductivity σ (Ω^{-1} cm ⁻¹)	Activation energy E_a (eV)	TCR (%)
S10	80	1.0%	101	1.73	0.26	3.85	0.09	1.2
S25	80	2.5%	100	1.84	1.9	0.53	0.15	1.9
S40	80	4.0%	98	1.91	3.1	0.32	0.16	2.0
S55	80	5.5%	99	1.97	10.1	0.01	0.18	2.3

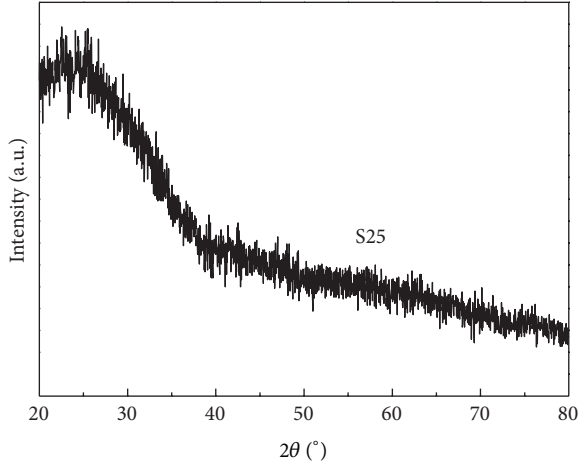


FIGURE 1: XRD pattern of TiO_x thin film (S25) deposited at the pO₂ of 1.5%.

The thickness and surface morphology of the films were characterized by field emission scanning electron microscopy (FESEM, Hitachi S4800). Glancing incidence X-ray diffraction (GIXRD, PANalytical X'Pert PRO) was performed by using Cu *K* α radiation (0.1564 nm) with a glancing incidence of 2°, $U = 40$ kV and $I = 35$ mA. The O/Ti stoichiometry of the films was measured by rutherford backscattering spectrometry (RBS, NEC 5SDH-2) performed with a 2.023 MeV ⁴He⁺ beam from a 2 \times 1.7 MV tandem accelerator. The temperature dependent electrical measurements were performed with a semiconductor characterization system (Keithley, 4200-SCS) in a temperature controller (Sigma Systems, Sigma C4) with an accuracy of 0.1°.

3. Results and Discussion

The GIXRD pattern for sample S25 is shown in Figure 1. The patterns of the other three samples have similar characteristics as S25. No sharp diffraction peak of any crystalline phase is observed, which indicates all the films deposited at room temperature have amorphous structure, with no preferred orientation as demonstrated in the previous studies [5, 14, 15].

Figure 2 presents the cross-sectional and surface morphological micrographs of sample S25, which shows that the thickness of the TiO_x film is about 100 nm, and the film is dense and smooth, which is the advantage of sputtering technique compared with other deposition methods [10].

Furthermore, no grain or cluster appears in the films, this confirms the amorphous structure of the films.

Figure 3 shows a typical experimental RBS spectrum of titanium oxide films (S25) deposited on p-silicon (100) substrate with the simulated spectrum using the program SIMNRA [16]. The O/Ti stoichiometry across the films have been obtained by simulating the experimental spectrum (circle) and theoretical spectrum (line). The results presented in Table 1 show the O/Ti ratio is in accordance with the pO₂, and all the films have nonstoichiometry compositions.

Figure 4 shows the electrical resistivity (ρ) of TiO_x films as a function of temperature. As is seen, the resistivity is significantly influenced by the pO₂ during the deposition process. The resistivity measured at room temperature increases from 0.26 Ω cm to 10.1 Ω cm as the pO₂ increases from 1% to 5.5%. This can be explained by the decrease of oxygen vacancies in the TiO_x films with the increasing pO₂ [17], resulting in an increase of O/Ti ratio as illustrated by RBS analysis. Thus the larger resistivity is obtained [12]. The electrical resistivity (ρ) or conductivity (σ) of the broad-band semiconductors can be expressed as follows [18]:

$$\rho = \rho_a \exp\left(\frac{E_a}{kT}\right), \quad (1a)$$

$$\sigma = \sigma_a \exp\left(-\frac{E_a}{kT}\right), \quad (1b)$$

where E_a is the thermal activation energy, k is the Boltzmann constant, T is the absolute temperature, and the preexponential factors ρ_a and σ_a are the resistivity at $T \rightarrow \infty$ and conductivity at $T \rightarrow 0$, respectively. As can be seen in Figure 4, the curves exhibit Arrhenius characteristics in accordance with equation (1a) [19].

From the temperature dependence of electrical conductivity plotted as $\ln\sigma$ versus $10^3/T$ shown in Figure 5, the activation energies of TiO_x films can be calculated from the slopes of the fitted lines by equation (1b), and the results are presented in Table 1 show that the activation energy increases from 0.09 eV to 0.18 eV with the increasing resistivity. With the activation energies, the temperature coefficient of resistivity (TCR) can be obtained and TCR is extensively exploited as one of the most important parameters characterizing the detectivity of uncooled IR sensors, defined as the slope of natural logarithm resistivity [20]:

$$\text{TCR} = \left(\frac{1}{\rho}\right) \times \left(\frac{d\rho}{dT}\right). \quad (2)$$

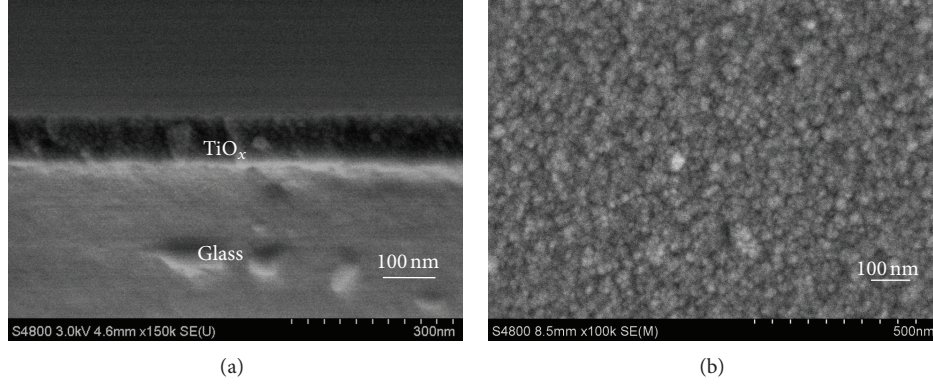


FIGURE 2: FESEM micrographs of sample S25 (the other samples are alike): (a) cross-section and (b) surface morphology.

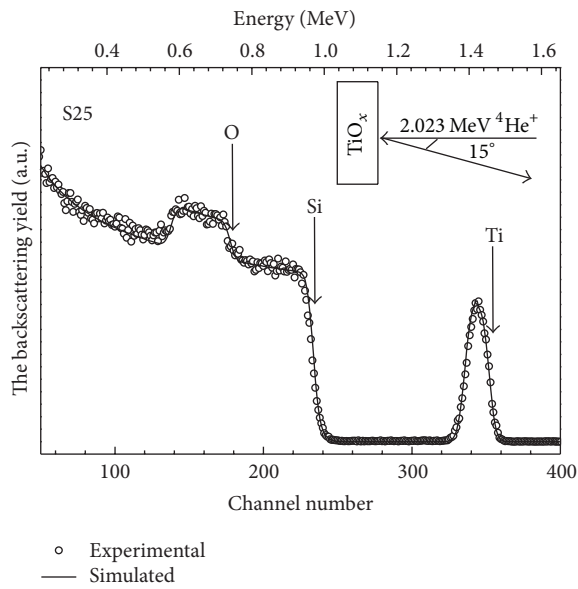


FIGURE 3: RBS spectrum of TiO_x thin film (S25) on p-Si (100) substrate.

Combining equation (1a) and equation (2), we can yield

$$E_a = -kT^2 \times \text{TCR}. \quad (3)$$

This relation links the activation energy E_a to TCR. With the calculated values of E_a , the TCR of the TiO_x films can be deduced from equation (3), and the absolute values of TCR are found to increase from 1.2% for to 2.3% as the pO_2 increase from 1% to 5.5%, respectively. This is due to the fact that the increase in oxygen during deposition can result in its direct incorporation into the films. Accordingly, an increased oxidation state could be expected to compensate the oxygen deficiency in the TiO_x films, and the electron concentration in the film decreases, which will cause an increase of the activation. As a result, absolute value of TCR increases [21].

In fact, for TiO_2 semiconductor thin films having broad energy gap about 3.0 eV, the contribution of impurity band conduction may become significant [22]. Mardare et al. have investigated the electrical properties of polycrystalline

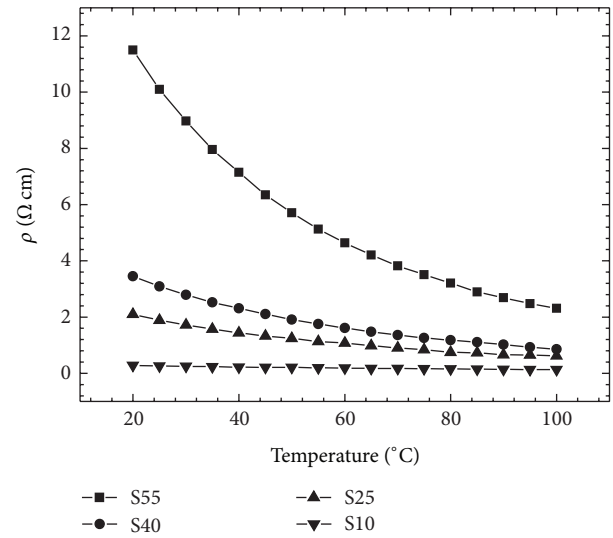


FIGURE 4: Temperature dependence of resistivity ρ in the temperature range from 20°C to 100°C.

TiO_x thin films containing a mixed phase of anatase and rutile, and they point out that at high temperatures ($T > 300$ K), the measured conductivity of TiO_x thin films can also be explained in terms of the simple thermally activated conduction mechanism, but at low temperatures ($T < 300$ K), the conductivity takes place through the electrons' variable range of hopping (VRH) between the localized states, and the activation energy of hopping is much smaller than that of the simple activated conduction [18]. However, they did not investigate the electrical transport properties of the a- TiO_x thin films, and the conduction mechanism is not clear yet. From the linear characteristics of the curves plotted as $\ln \sigma$ versus $10^3/T$ in Figure 5, the mechanism of electrical conduction in a- TiO_x thin films can be explained according to the thermally activated mode in the temperature domain 293 K to 373 K, as illustrated by equation (1b).

Furthermore, we have found that the pre-exponential factors σ_a of TiO_x thin films exhibits an exponential dependence as functions of the activation energies, as presented

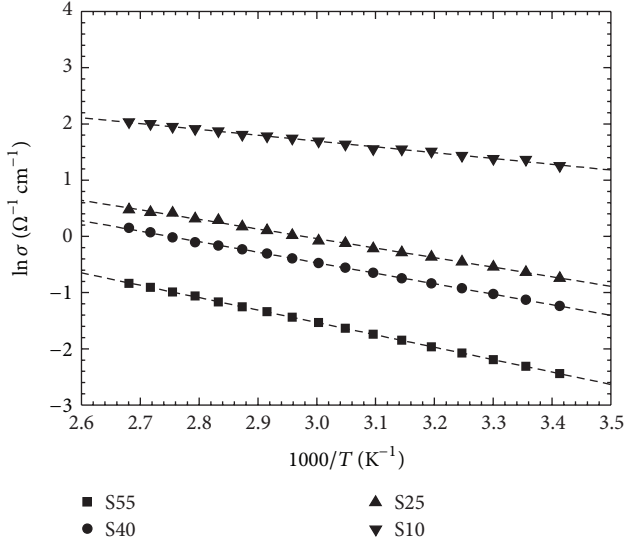


FIGURE 5: Temperature dependence of conductivity σ plotted as $\ln \sigma$ versus $10^3/T$ in the range between 293 K and 373 K.

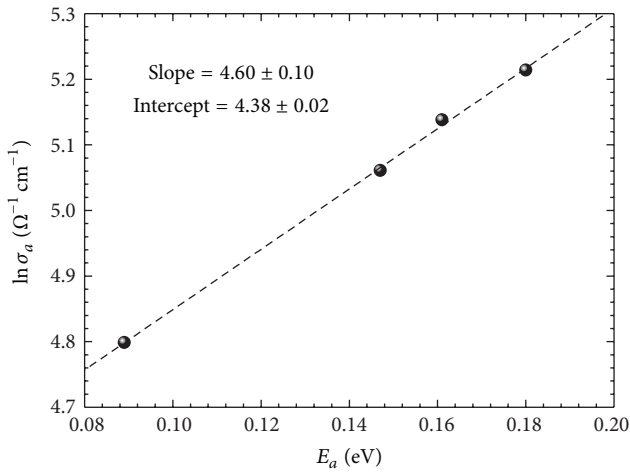


FIGURE 6: Preexponential factors σ_a as a function of activation energies E_a of TiO_x films deposited at various $p\text{O}_2$.

in Figure 6. The data can be fitted linearly by the following function:

$$\ln \sigma_a = \ln \sigma_{a0} + \frac{E_a}{E_{MN}}, \quad (4a)$$

where σ_{a0} and E_{MN} are constants, called the Meyer-Nedel pre-exponential factor and characteristic energy, respectively. This relation can also be written as

$$\sigma_a = \sigma_{a0} \exp\left(\frac{E_a}{E_{MN}}\right). \quad (4b)$$

This is called the Meyer-Neldel Rule (MNR) because it was first pointed out by Meyer and Neldel in 1937 [23], and the relation gives the dependence of the pre-exponential factor σ_a on the activation energy E_a . Although it is an empirical relation (also called as the compensation rule), the MNR

has been frequently observed in a wide variety of condensed matter, particularly in disordered, amorphous, and nanocrystalline materials that exhibit a thermally activated behavior, such as amorphous silicon [24], chalcogenide glasses [25, 26], liquid semiconductors [27], and polymers [28]. As shown in Figure 6, the σ_a increases with the increasing E_a , indicating the electrical conductivity in amorphous TiO_x thin films deposited obeys the normal MNR but not inverse MNR [29].

4. Conclusion

Amorphous TiO_x (a- TiO_x) thin films for bolometric application have been fabricated at room temperature using a dc reactive sputtering technique. The O/Ti ratio changes from 1.73 to 1.97, and the resistivity of the samples varies from $0.26 \Omega \text{ cm}$ to $10.1 \Omega \text{ cm}$ and TCR from -1.2% to -2.3% with different oxygen partial pressures. It has been demonstrated that the dependence of electrical conductivity of the films exhibits a thermally activated behavior in the temperature range from 293 K to 373 K. Furthermore, it is also found that the electron transport mechanism in the a- TiO_x obeys the well-known normal Meyer-Neldel Rule.

References

- [1] A. Fujishima and K. Honda, "Electrochemical photolysis of water at a semiconductor electrode," *Nature*, vol. 238, no. 5358, pp. 37–38, 1972.
- [2] M. R. Hoffmann, S. T. Martin, W. Choi, and D. W. Bahnemann, "Environmental applications of semiconductor photocatalysis," *Chemical Reviews*, vol. 95, no. 1, pp. 69–96, 1995.
- [3] B. O'Regan and M. Grätzel, "A low-cost, high-efficiency solar cell based on dye-sensitized colloidal TiO_2 films," *Nature*, vol. 353, no. 6346, pp. 737–740, 1991.
- [4] B. Karunakaran, P. Uthirakumar, S. J. Chung, S. Velumani, and E.-K. Suh, " TiO_2 thin film gas sensor for monitoring ammonia," *Materials Characterization*, vol. 58, no. 8–9, pp. 680–684, 2007.
- [5] A. L. Lin, "Bolometer having an amorphous titanium oxide layer with high resistance stability," U.S. Patent 7442933, 2008.
- [6] A. Verma, A. Basu, A. K. Bakhshi, and S. A. Agnihotry, "Structural, optical and electrochemical properties of sol-gel derived TiO_2 films: annealing effects," *Solid State Ionics*, vol. 176, no. 29–30, pp. 2285–2295, 2005.
- [7] A. Testino, I. R. Bellobono, V. Buscaglia et al., "Optimizing the photocatalytic properties of hydrothermal TiO_2 by the control of phase composition and particle morphology. A systematic approach," *Journal of the American Chemical Society*, vol. 129, no. 12, pp. 3564–3575, 2007.
- [8] X. Chen and S. S. Mao, "Titanium dioxide nanomaterials: synthesis, properties, modifications and applications," *Chemical Reviews*, vol. 107, no. 7, pp. 2891–2959, 2007.
- [9] T. Kubart, O. Kappertz, T. Nyberg, and S. Berg, "Dynamic behaviour of the reactive sputtering process," *Thin Solid Films*, vol. 515, no. 2, pp. 421–424, 2006.
- [10] S. Berg and T. Nyberg, "Fundamental understanding and modeling of reactive sputtering processes," *Thin Solid Films*, vol. 476, no. 2, pp. 215–230, 2005.
- [11] D. Wicaksana, A. Kobayashi, and A. Kinbara, "Process effects on structural properties of TiO_2 thin films by reactive sputtering,"

- Journal of Vacuum Science and Technology A*, vol. 10, pp. 1479–1482, 1992.
- [12] R. G. Breckenridge and W. R. Hosler, “Electrical properties of titanium dioxide semiconductors,” *Physical Review*, vol. 91, no. 4, pp. 793–802, 1953.
- [13] J. Nowotny, T. Bak, M. K. Nowotny, and L. R. Sheppard, “Titanium dioxide for solar-hydrogen II. Defect chemistry,” *International Journal of Hydrogen Energy*, vol. 32, no. 14, pp. 2630–2643, 2007.
- [14] P. Löbl, M. Huppertz, and D. Mergel, “Nucleation and growth in TiO₂ films prepared by sputtering and evaporation,” *Thin Solid Films*, vol. 251, no. 1, pp. 72–79, 1994.
- [15] L.-J. Meng, M. Andriitschky, and M. P. dos Santos, “The effect of substrate temperature on the properties of d.c. reactive magnetron sputtered titanium oxide films,” *Thin Solid Films*, vol. 223, no. 2, pp. 242–247, 1993.
- [16] M. Mayer, “SIMNRA, a simulation program for the analysis of NRA, RBS and ERDA,” in *AIP Conference Proceedings*, vol. 475, pp. 541–544, 1999.
- [17] L.-J. Meng and M. P. dos Santos, “The influence of oxygen partial pressure on the properties of DC reactive magnetron sputtered titanium oxide films,” *Applied Surface Science*, vol. 68, no. 3, pp. 319–325, 1993.
- [18] D. Mardare, C. Baban, R. Gavrilă, M. Modreanu, and G. I. Rusu, “On the structure, morphology and electrical conductivities of titanium oxide thin films,” *Surface Science*, vol. 507–510, pp. 468–472, 2002.
- [19] K. J. Laidler, “The development of the arrhenius equation,” *Journal of Chemical Education*, vol. 61, no. 6, pp. 494–498, 1984.
- [20] K. C. Liddiard, “Thin-film resistance bolometer IR detectors,” *Infrared Physics*, vol. 24, no. 1, pp. 57–64, 1984.
- [21] M. Soltani, M. Chaker, E. Haddad, R. V. Kruzelecky, and J. Margot, “Effects of Ti-W codoping on the optical and electrical switching of vanadium dioxide thin films grown by a reactive pulsed laser deposition,” *Applied Physics Letters*, vol. 85, no. 11, pp. 1958–1960, 2004.
- [22] M. Vaziri, “Low-temperature conductivity of epitaxial ZnSe in the impurity band regime,” *Applied Physics Letters*, vol. 65, no. 20, pp. 2568–2570, 1994.
- [23] W. Meyer and H. Neldel, “A relation between the energy constant ϵ and the quantity constant a in the conductivity-temperature formula for oxide,” *Zeitschrift für Technische Physik*, vol. 18, pp. 588–593, 1937.
- [24] R. S. Crandall, “Defect relaxation in amorphous silicon: stretched exponentials, the Meyer-Neldel rule, and the Staebler-Wronski effect,” *Physical Review B*, vol. 43, no. 5, pp. 4057–4070, 1991.
- [25] N. Mehta, “Meyer-Neldel rule in chalcogenide glasses: recent observations and their consequences,” *Current Opinion in Solid State and Materials Science*, vol. 14, no. 5, pp. 95–106, 2010.
- [26] K. Shimakawa and F. Abdel-Wahab, “The Meyer-Neldel rule in chalcogenide glasses,” *Applied Physics Letters*, vol. 70, no. 5, pp. 652–654, 1997.
- [27] J. Fortner, V. G. Karpov, and M.-L. Saboungi, “Meyer-Neldel rule for liquid semiconductors,” *Applied Physics Letters*, vol. 66, pp. 997–999, 1995.
- [28] G. F. Myachina, T. G. Ermakova, and V. A. Lopyrev, “Compensation effect in the electric conduction in some conjugated polymers,” *Physica Status Solidi A*, vol. 81, no. 1, pp. 377–380, 1984.
- [29] K. L. Ngai, “Meyer-Neldel rule and anti Meyer-Neldel rule of ionic conductivity conclusions from the coupling model,” *Solid State Ionics*, vol. 105, no. 1–4, pp. 231–235, 1998.

Research Article

Surface-Assisted Luminescence: The PL Yellow Band and the EL of n-GaN Devices

José Ignacio Izpura

Department of Aerospace Systems, Infr. and Airports, Universidad Politécnica de Madrid, 28040 Madrid, Spain

Correspondence should be addressed to José Ignacio Izpura; joseignacio.izpura@upm.es

Received 7 May 2013; Accepted 2 September 2013

Academic Editor: Xia Xiang

Copyright © 2013 José Ignacio Izpura. This is an open access article distributed under the Creative Commons Attribution License, which permits unrestricted use, distribution, and reproduction in any medium, provided the original work is properly cited.

Although everybody should know that measurements are never performed directly on materials but on devices, this is not generally true. Devices are physical systems able to exchange energy and thus subject to the laws of physics, which determine the information they provide. Hence, we should not overlook device effects in measurements as we do by assuming naively that photoluminescence (PL) is bulk emission free from surface effects. By replacing this unjustified assumption with a proper model for GaN surface devices, their yellow band PL becomes surface-assisted luminescence that allows for the prediction of the weak electroluminescence recently observed in n-GaN devices when holes are brought to their surfaces.

1. Introduction

Some years ago, we published reports about the high gain of GaAs photoresistors at low illumination levels due to the optical modulation of depleted regions under the GaAs surface [1, 2]. This gain G_S , derived from the photo-FET devices that the naked surface and the bottom interface with the substrate created in GaAs epilayers, is inversely proportional to the illumination power P_L impinging on the photoresistor thus, it is orders of magnitude greater than the “photoconductive” gain G_B due to the conductivity modulation of the GaAs bulk by photogenerated electron-hole pairs at low illumination levels. Therefore, the changes ΔR in the resistance R of any GaAs photoresistor under weak illumination power P_L reflect modulations in the channel cross-section of this two-terminal device (2TD) rather than conductivity modulations of their inner material as it is commonly assumed.

By defining the gain of these photoresistors by the ratio $G_X = \Delta R / \Delta P_L$, where ΔP_L is the change in optical power (e.g., the optical signal) and G_X denotes G_S or G_B coming from the two different photoresponses described previously, we found that G_S was the dominant gain (e.g., $G_S > 10^4 G_B$) in these 2TDs at illumination levels typically used in photoconductance (PC) measurements, such as those reported in [3]. The title of this report, “*Study of defect states in GaN films by*

photoconductivity measurement,” is wrong or at least greatly misleading because nobody measures the conductivity of materials, only the conductance $G = 1/R$ of 2TDs containing these materials. To assume naively that conductance changes $\Delta G = 1/\Delta R$ of 2TDs mirror changes in the conductivity of their inner materials is wrong in general. This assumption, which suggests that G_B exists while G_S is null, is false, and there is evidence of this. One piece of evidence can be found in [1, 2], where we showed that the most likely situation is the opposite one, where G_S accounts well for the gain of the photoresistor because the G_B contribution is negligible. More striking proof is found in [4], which shows that the enigmatic $1/f$ “excess noise” of solid-state devices is simply the noise mechanism that corresponds to the gain G_S of these devices.

Given the low P_L values used in PC measurements, the situation $G_S \gg G_B$ is very likely to occur. This indicates that the authors of [3] presuppose a gain mechanism for their GaN photoresistors that is likely wrong, although their PC data applied to the gain G_S are excellent in explaining the yellow band (YB) found in the photoluminescence (PL) of n-GaN “samples,” which are the devices used in PL experiments because nobody measures the PL of materials but the luminescence of devices containing these materials. The devices required to measure PL do not need to have two terminals such as those 2TDs required in conductance measurements. In fact, they look like “simple” devices that

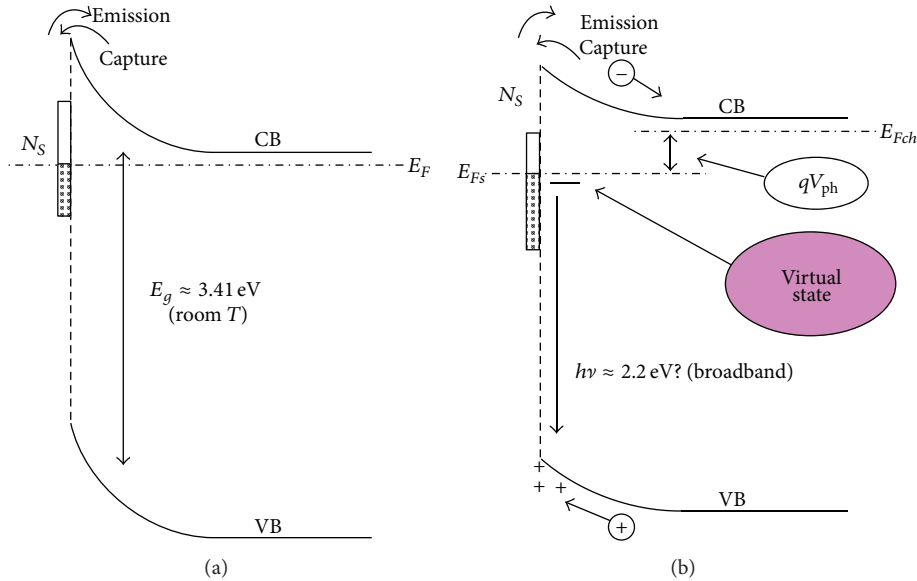


FIGURE 1: (a) Band diagram of n-GaN Device no. 1 near its surface in thermal equilibrium (TE). (b) Band diagram of Device no. 1 out of TE during a photoluminescence experiment.

only require their surface to be crossed by the laser light entering the material (n-GaN in this case) whose luminescent emission is then measured. A continuous medium such as an infinite volume of n-GaN material would be useless for PL measurements because it would not have the aforementioned surface separating the PL driver (laser) from the material driven (excited) by this laser that emits the luminescence we call the PL response or “PL spectrum” in general.

Therefore, there is no way to avoid testing a device in a measurement system because to extract information from the “device under test” (DUT) we need a system capable of exchanging the energy relevant to the experiment (e.g., photons in PL, electrical energy in conductance measurements, etc.). This demonstrates the essential role of the device in physics, of which not all scientists are aware. When we consider this device and its effects on measurements, enigmatic measurements such “excess noise” in solid-state devices [4], flicker noise in vacuum devices [5], and even the more complex oscillator phase noise [6] are easily understood. Concerning the PL of n-GaN “material”, its YB peak at approximately 2.2 eV [7] is enigmatic because it emits photons with energies below the bandgap $E_g \approx 3.41$ eV of this material at a temperature $T = 300$ K (room T). To solve this “enigma,” we must find a device capable of emitting photons with energies $h\nu < E_g$. Believing that the PL response is derived only from the bulk region, as most people do, we agreed that the solution presented in [7] (a handy trap in the volume of the n-GaN) was a good trial among the many fashionable theories on the subject, but one of us had another proposal for how this YB is generated, using the surface model used in [1, 2].

The GaN YB measured in [7] was assigned to transitions of electrons from the CB to a deep level lying at 1 eV from the VB. This “trap-based” model is a handy theory that is

well accepted in journals; it is based on a bulk defect that we denote as being “ad hoc” in explaining the enigmatic effect. This leads to “materials doped by traps” that are difficult to understand because these traps are technologically “elusive.” By this we mean that technology can provide two n-GaN materials with N_d and with $5N_d$ donors per cm^3 quite reliably but not n-GaN with some YB emission and n-GaN with YB emission that is five times as strong. This suggests that the YB cannot be a property of the n-GaN material but the emission from something that exists in each PL arrangement we use to exchange optical energy with the n-GaN material. Because a device is the system we have to use for this exchange of energy, let us look for possible devices we may have overlooked in this case. This is the other proposal we had envisaged from a careful set of PC measurements we had performed at that time [1, 2]. However, its radical departure from the most fashionable theories on the YB of n-GaN in 1997 and its immaturity (it was based on [2], which was about to be published, and on [1], which had just been published) made it inappropriate for journals in which “differential changes” in a fashionable theory are likely accepted but radical departures are rejected due to the dogmatic defence of prevailing theories by most reviewers. Thus, the band diagrams shown in Figure 1 did not appear in [7].

Using the results we obtained when we considered a physical model for a 2TD [8] that agrees with quantum physics [9], or better phrased, when we do not forget the physics of the device used to extract information (e.g., to measure), and being aware of the weak EL (electroluminescence) recently found in n-GaN field-effect transistors (FET) [10, 11], we decided to write this paper to communicate the other proposal we had in 1997 for the weak YB found in the PL of n-GaN samples. This radical proposal unifies the PC data of [3], the YB of the PL emission of n-GaN samples [7], and

the weak EL of [10, 11] in a cogent model that explains these phenomena. Therefore, we consider the strong influence of the GaN surface in measurements, which we expected from the strong influence of the surface of GaAs devices [1, 2, 12]. The surface band bending (SBB) of n-GaN surfaces, which is roughly twice that we measured in n-GaAs surfaces [2], is able to collapse GaN field-effect transistors (FETs) [13], hence the reason to expect its strong influence in PL experiments. Therefore, let us pay attention to the device linked to the surface of n-GaN material under photoluminescence (PL) conditions.

The key role of devices in measurements must be considered before assigning any property to their inner material. References [1, 2, 4–6] demonstrate the benefits obtained when we do not assume naively that the conductance of a 2TD reflects the conductivity of its inner material. However, this is a common assumption that is reflected in the title of [3] and in the first sentence of [14], which cites only two examples among the thousands that appear in physics and engineering journals. As in GaAs devices, this misconception about conductivity (in $\Omega^{-1} \text{cm}^{-1}$) mirroring (e.g., being proportional to) the conductance (in Ω^{-1}) of photoresistors will also fail in GaN-based devices because their conductive volume is not equal to the whole volume of the GaN material. There are depleted regions under their surfaces because n-GaN tends to hold electrons in surface states (SEs). The SBB is derived from the double layer (DL) formed by the negative charges trapped in occupied SEs and the positive charges of a depleted region of thickness W . The collapse of GaN FETs is a dramatic effect of this behaviour of n-GaN surfaces that is capable of forming a negative floating gate on the surface of these devices [13, 15].

Although the manner in which the SBB invalidates the aforementioned proportionality was described in [1, 2], it was so deep rooted in our minds that we wrote in the introduction of [2]: “... *thus modulating the effective volume that takes part in the electrical conductivity of the samples.*” It is clear that we meant “*in the electrical Conductance of the samples,*” which are the 2TDs in which these frequency-resolved PC measurements were taken. Only from these conductance data and with some care can the conductivity of these materials be deduced. We apologise for making this mistake, which shows that we ourselves found it very hard to abandon our prejudices regarding conductivity modulation, which most people assume. Given the ease with surface devices in 2TDs are overlooked, this error is more likely to occur for devices without terminals such as the samples used in PL experiments. To demonstrate the misleading effects of this error, Section 2 will present a model for the surfaces of n-GaN samples that we will use to explain photoconductance (PC) measurements in n-GaN photoconductors. In Section 3, we will show how this model for the surface of n-GaN allows for the explanation of the YB of n-GaN samples under the optical driving to which they are submitted in PL experiments. Section 4 will demonstrate how this model allows for the prediction of the weak electroluminescence (EL) recently found in GaN-based transistors when holes reach their surfaces [10, 11], and some conclusions will be drawn at the end.

2. Surface-Induced Photoconductance in N-Type GaN Devices

Though authors of [3] did not use an appropriate title for the report, their photoconductance data (PC data) are valuable in accurately modelling Device no. 1 due to the surface of n-GaN. Due to its depleted region under the surface, a GaN epilayer of thickness d only offers a channel thickness ($d-W$) for the conductance of any 2TD using this epilayer as its channel between terminals. This was reported many years ago for GaAs [1, 2, 16]. Because a similar effect for the bottom interface between this epilayer and the substrate would roughly duplicate the reasoning at hand, it will not be dealt with at this moment. This bottom photo-FET reinforces our proposal regarding photoresistors presented in [3]: under a weak light source, the PC system will behave as a photo-FET, where photons will reduce the depleted thickness W of their SBB and not as photoresistors with noticeable conductivity modulation.

Thus, the name photoconductive detectors for the 2TD used in PC experiments is generally wrong because these photodetectors, which are made from two ohmic contacts on an epilayer, have two detection mechanisms G_S and G_B whose relative weight depends on the light power they receive (see Figure 6 of [1] for details). Under high illumination power, they show the expected conductivity modulation by the photogenerated carriers giving them their photoconductive gain G_B , which is linked to the ratio between the photocarriers' lifetime and their transit time between the terminals of the 2TD. This is the type of response (gain G_B) assumed in [3], which requires a hypothesis about the band tails of states to allow photons with energies lower than E_g to produce a PC response. At low illumination levels, however, these devices react as floating-gate photo-FETs whose associated SBB is reduced by photons. We attribute their upper surface (and bottom interface), whose DL looks like that of the gate of a FET, as being the source of their high gain G_S due to the photobackgating of space-charge regions around the channel [1, 2]. This gain G_S , which is proportional to the inverse of the illumination power P_L [1], largely exceeds the gain G_B assumed in [3], as we demonstrated in [1, 2] for GaAs with a similar but lower SBB.

Hence, under the low P_L of a PC system, the photoresistors of [3] will exhibit a PC response because G_S does not require the generation of electron-hole pairs because the emptying of SEs is enough to produce a PC response like that of GaAs [1, 2]. This PC response of the samples used in [3], which would not exist for photons with energy $h\nu < E_g$ without the band tails proposed in Figure 3 for the gain G_B , is perfectly possible without band tails for the photo-FET gain G_S by considering that photons with energy $h\nu < E_g$ empty occupied SEs without generating electron-hole pairs. This photo-induced SBB reduction and the shrinkage of W it induces (light-induced backgating effect) will increase the conductance $G = 1/R$ of the photoresistors described in [3], which under this weak illumination are photoconductance detectors of gain G_S and not photoconductive detectors of gain G_B .

Hence, we propose that the PC signal exhibited by the devices described in [3] for photons with energy $h\nu < E_g$ is due to photons emptying the SEs of their GaN surface. To investigate this possibility, let us consider the band diagram shown in Figure 1(a) as we approach the surface of a sample of n-GaN in TE, thus in the dark. The flat part of Figure 1(a) is the band diagram of an infinite bulk n-GaN (Device no. 0) in TE. When Device no. 0 is “cut,” the surface appears; thus, a density of $N_S \text{ cm}^{-2}$ SE is exposed on this surface, and Device no. 1 is created because N_S allows for new ways to store and exchange energy by those electrons that occupy SEs in Device no. 1. This leads to eigenstates of energy such as those handled in the quantum treatment of this exchange called “Generalised Noise” in [9]. Concerning the charge states of these SEs linked to electrical energies, let us assume two choices derived from [13]: (a) neutral when empty and (b) charged by a magnitude $-qC$.

With electric charges arranged in space, we can use thermodynamics to say that Device no. 1 has a degree of freedom to store electrical energy. By this we mean that electrical energy is stored by the double layer (DL) or space-charge region formed by a sheet of negative charge in the surface due to $N_F \text{ cm}^{-2}$ electrons occupying SEs and a thicker sheet of positive charge (depleted region) of $+qN_F C/\text{cm}^2$ compensating the $-qN_F C/\text{cm}^2$ sheet density of the surface. This proximity of the $+qN_F$ and $-qN_F$ sheet charges minimises the stored energy, and its dipolar nature prevents the existence of electric fields far from the surface that would absorb energy for the conduction currents they would produce in the GaN bulk, for example. Therefore, this DL has $-qN_F C/\text{cm}^2$ on the surface and a thicker slab of charge under the surface (a depleted region of thickness $W \approx N_F/N_d$ cm for a uniform doping $N_d \text{ cm}^{-3}$ of the n-GaN material). This DL creates the SBB shown in Figure 1(a), which becomes an energy barrier $\Delta E = q\phi \text{ eV}$ for those electrons in the conduction band (CB) of the n-GaN to reach the surface. This barrier selects those electrons of the CB liable to be trapped in SEs, thus constituting a capture barrier.

By viewing the surface as a planar trap with $(N_S - N_F) \text{ cm}^{-2}$ centres able to capture electrons from the GaN bulk, this capture process can be understood to be thermally activated [2] with energy $\Delta E = q\phi \text{ eV}$ because only those electrons surpassing the SBB barrier can be captured by one SE (tunnelling is not considered to simplify the process). This planar capture differs from the capture assigned to a bulk trap with $N_T \text{ cm}^{-3}$ centres embedded in the volume because it is not an “in situ” capture process that varies the $n \text{ cm}^{-3}$ electron concentration in the CB. Instead, it is an “ex situ” capture process in which each electron captured from the bulk GaN is not held within this bulk but at some distance on the surface. This distance, however, is crossed by some electrons of the CB, thus allowing thermal interaction by the exchange of particles and energy between the surface and the bulk. Hence, this capture by the surface does not vary the concentration of electrons in the bulk far from the surface as it would for a “bulk trap” with $N_T \text{ cm}^{-3}$ centres embedded in the GaN. This planar capture slightly modifies the thickness W of the depleted region next to the surface [2, 4].

In a planar channel with a thickness $(d - W)$ under its surface, the fluctuations ΔW due to these emission-capture fluxes of electrons at the surface (see Figure 1(a)) will lead to fluctuations ΔG in the conductance G measured between the two terminals of the channel. These fluctuations ΔG and those emanating from fluctuations in the conductivity of its material, provided its thickness W is constant, would be indistinguishable. Thus, assuming naively that W is constant, we will find in the conductance of the channel of the 2TD the trapping effects due to this planar trap, which will mislead us towards a deep “bulk trap” with thermal energy $E_T = q\phi \text{ eV}$ because emission-capture processes over an SBB are thermally activated with $E_T = q\phi \text{ eV}$ [2]. This feature allowed us to measure SBBs by photoconductance frequency resolved spectroscopy [2], which previously was considered photoconductivity frequency resolved spectroscopy (PCFRS). This planar trap in the surface leads us to consider that the data of [3] are excellent PC data that we will use to determine the PC gain G_S of these photoconductors operating as photo-FETs under low illumination (e.g., not conductivity data).

When photons with energy below E_g reinforce the thermal emission indicated by an arrow in Figure 1(a), the $(N_F/N_S)_{\text{TE}}$ ratio in TE (e.g., in the dark) is reduced to $(N_F/N_S)_{\text{PC}}$ by the weak light of the PC system. This is so because to sustain a higher (thermal + optical) emission in Device no. 1, we need more captures per second, which are only possible with a slightly lower SBB at the same temperature T . This lower SBB requires a lower N_F , which leads to a lower W , thus increasing the channel cross-section of the photoresistor and hence its conductance. This gain G_S gives the PC signals shown in [3], which the authors consider as being due to G_B , though without proof. Thus, the PC data for sample 511 that appear in Figure 1 of [3] will have to do with a band diagram like that of Figure 1(b) but without holes in its valence band (VB) near the surface because holes will not appear for photons with $h\nu < E_g$ in Device no. 1. Note that the SBB existing under illumination cannot be that in TE. If this were so, we would have $(N_F/N_S)_{\text{TE}} = (N_F/N_S)_{\text{PC}}$, but this is not possible. If emission from the surface is higher because the electrons trapped in SEs have a lower lifetime τ under a higher thermal + optical emission, this requires more captures per unit time than in TE to be counterbalanced. This lowers N_F , which in turn reduces the SBB or capture barrier. Thus, the capture rate is slightly increased until a dynamical equilibrium, with $(N_F/N_S)_{\text{PC}} < (N_F/N_S)_{\text{TE}}$, is reached under the weak light of the PC system.

Our simple interpretation of the PC data of [3] as a photo-backgating effect due to the n-GaN SBB allows us to test our model of Figure 1(a) with the help of Figure 2, which sketches the PC spectrum of sample 511 found in Figure 1 of [3]. To complete our model for Device no. 1, let us assume that the SBB of n-GaN is $q\phi \approx 1.2 \text{ eV}$ (roughly twice the value we measured for n-GaAs surfaces [2]) and that the photovoltage V_{ph} generated by photons with energy $h\nu < E_g$ of the PC system is small. In this case, Figure 1(a) would be mostly approximated for the sample under the weak light of the GE 1493 lamp filtered (thus attenuated) by a monochromator, as described in [3]. The absence of a PC signal for photons with $h\nu < 1.3 \text{ eV}$ in Figure 2 could mean that the light power

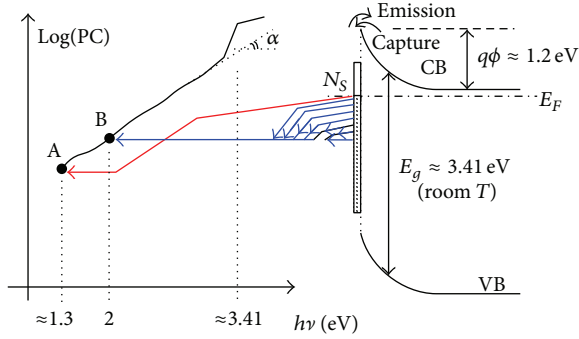


FIGURE 2: Diagram linking photoconductance signal (log axis) to photon energy for Device no. 1, whose band diagrams are shown in Figure 1. The PC signal at point A is due to electrons emitted from SE close to the quasi-Fermi level E_F , while the PC signal at point B accumulates the emissions of electrons trapped at SEs covering a band between E_F and 2 eV below the CB (see the text).

with photon energy $h\nu < 1.3$ eV was null in [3] or that the response of Device no. 1 (its gain G_B) for these photons was null. The first option is discarded because for p-doped GaN photoresistors such as sample AA1 of Figure 1 of [3], a PC response was measured for $h\nu < 1.3$ eV. Thus, the more likely situation is that Device no. 1 did not produce a PC signal for photons with $h\nu < 1.3$ eV.

This would be so if the SBB of the n-GaN were close to 1.2 eV because those SEs above the Fermi level in Figure 2 would be empty and would not produce any PC signal (e.g., no electrons could be emitted from empty SEs, and no change in W would take place). This confirms the $q\phi \approx 1.2$ eV obtained for Device no. 1, but it does not indicate the absence of SEs for energies closer to the CB than $q\phi$: it only means that SEs below the CB down to 1.2–1.3 eV are empty at room temperature. With this model for Device no. 1 on the n-GaN surface, we could say that the PC system of [3] detects that sample 511 has occupied SEs up to ≈ 1.3 eV below the CB, and from the slope of its PC curve around point A in Figure 2, we could say that this distribution of SEs would continue to decrease as we approach the CB. This behaviour, predicted from a trend (thus without data below the threshold energy $h\nu_t \approx 1.3$ eV), is only an attempt to predict what the SE density does near the CB. As the photon energy is increased from $h\nu_t \approx 1.3$ eV, the PC signal of sample 511 rises in a way that appears exponential from the semilog plot of Figure 2. This suggests an exponential increase in the density $N_S(E)$ as we go down in energy E towards the VB in the gap, although we have to consider the cumulative effect of photoemitted electrons as photon energy $h\nu$ increases. By this we mean that the PC photon flux with energy $h\nu \approx 2$ eV not only empties SEs lying at 2 eV below the CB (see the horizontal arrow in Figure 2) but also those SEs lying between 2 eV and 1.3 eV below the CB (see arrows indicating all of these contributions for photon energy $h\nu = 2$ eV in Figure 2).

For each photon energy $h\nu$, the PC response or gain G_B accumulates effects due to all of the occupied SEs from the uppermost SE close to the Fermi level E_F in Figure 1(a) (properly speaking, close to the surface imref E_{F_s} of Figure 1(b)) to

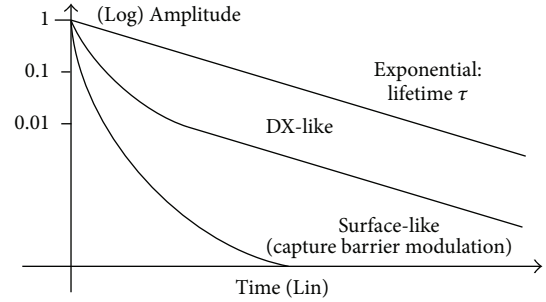


FIGURE 3: Semilog plots of net-capture transients derived from traps with the same emission lifetime τ but different boundary conditions during the transient. During the surface-like decay, the capture barrier increases as capture takes place (see text).

the lowest SE lying $h\nu$ eV below the CB that photons are able to empty. Because these types of calculations were published many years ago by one of the authors of [3] in an excellent book [17] (see its Section 3-A-5), we can confidently say that the band tails proposed in Figure 3 of [3] simply contribute $N_S(E)$, which is the energy distribution of SEs within the gap of n-GaN. From the PC data of [3], we obtain an $N_S(E)$ proportional to $\exp(h\nu/E_0)$ with E_0 between 230 meV and 280 meV [3]. Thus, the PC curve of sample 511 sketched in Figure 2 shows that there is a band of SEs from $h\nu \approx 1.3$ eV below the CB (at least) to the VB itself, whose $N_S(E)$ increases as $\exp(h\nu/E_0)$ as we approach the VB. The density of bulk states shown in Figure 3(a) of [3] would reflect this $N_S(E)$ of SEs, not the tails of states its authors believe are indicated by the deep-rooted “conductivity modulation” concept. To further prove this result, we will find in Section 4 empirical proof of the validity of this $N_S(E)$ derived from the PC data of [3] and our model for the surface of n-GaN.

Concerning the tails of states close to the VB proposed in [3], it is worth noting that the abrupt increase in PC data for $h\nu \approx E_g$ (close to 3.41 eV at room T) in Figure 1 of [3] (see Figure 2) may have to do with these types of tails. In this case, however, the response of the 2TD of [3] would start to show its response G_B in the bulk in addition to the response G_S linked to the surface we have considered up to this point. Thus, the title of [3] would not be as misleading because it might appear from the beginning of this section that its sample 511 has two devices generating its PC signal: Device no. 1, due to its surface, producing the main response for $h\nu < E_g$ at this low illumination power and Device no. 0, due to its bulk region, adding a PC response more closely linked to G_B for $h\nu > E_g$, both contributing to the PC signal measured between their two terminals. In any case, we can conclude that on the surface of n-GaN there is a band of SEs going from the VB up to ≈ 1.3 eV below the CB (and most likely up to the CB itself) with a density $N_S(E) \propto \exp(-h\nu/E_0)$. This band explains the great ability of n-GaN to trap electrons at SEs, which produces its high SBB and its harmful effects in GaN FETs [13, 15].

To show that the surface photovoltage v_{ph} under the weak illumination of the PC system is negligible, let us consider Figure 1(a), where the planar capture by the surface and

the planar emission from the surface in TE are mutually counterbalanced to maintain the average SBB of n-GaN devices. We use “average” because this SBB is derived from a dynamical equilibrium in which the fluctuation in W it endures is an undesired source of conductance noise [4, 12]. Therefore, let us consider this planar source of conductance fluctuations in channels such as those used by most solid-state devices today. Because the fluctuations in the conductance of a 2TD due to a planar trap and those expected for a bulk trap are indistinguishable, planar traps strongly suggest the existence of deep levels lying hundredths of meV below the CB. This notion is reinforced by the high thermal activation energy $E_T = q\phi$ eV the traps show, which is what we believed to be true before discovering that emission-capture processes over a SBB show a thermal activation energy $E_T = q\phi$ eV in PC experiments [2]. Thus, the planar traps on the surface perfectly mimic the effects expected for the handy carrier traps known as “deep levels.” This imitation of a nonexistent bulk trap goes beyond the appearance of a high thermal activation energy $E_T = q\phi$ eV in Arrhenius plots as soon as T varies by a few tens of K. This imitation is so good that the electron flux captured by the surface (CA in cm^{-2}/s) becomes

$$\text{CA} = c_n \times (N_S - N_F) \times n \times \exp\left(\frac{-q\phi}{kT}\right), \quad (1)$$

where k (J/K) is the Boltzmann constant, n (cm^{-3}) is the free electron gas concentration in the GaN bulk under the surface, $(N_S - N_F)$ (cm^{-2}) is the density of SEs able to capture electrons from the bulk, and C_n is a capture coefficient, which must be expressed in cm^3/s , the same units of the capture coefficient C_n of the “well-known” bulk traps. This means that C_n can be taken as the product of the mean thermal velocity v_{th} (cm/s) of electrons moving towards the surface and a capture cross-section σ_n (cm^2), which, when combined with the exponential term of the SBB barrier, leads to the idea of a thermally activated capture cross-section for a nonexistent deep trap in the bulk.

Therefore, let us gain deeper insight into this planar trap by considering the emission flux counterbalancing the capture flux expressed by (1) in TE. Using the concept of lifetime τ for the $N_F \text{ cm}^{-2}$ electrons occupying SEs, whose thermal activity will emit from time to time towards the GaN bulk, the emitted flux (EM in cm^{-2}/s) will be

$$\text{EM} = \frac{N_F}{\tau} = e_n N_F. \quad (2)$$

Equation (2) indicates that a pure emission transient from the GaN surface towards the GaN bulk without the counteracting capture that it uses to exist when trapping transients in devices will experience an exponential decay of N_F with lifetime τ . However, the boundary conditions during these transients lead to processes in which both emission and capture coexist in time t . A good example of such species are donor-related transients in AlGaAs, where a net-capture transient starting without electrons in donors at $t = 0$ (thus with null emission at $t = 0$) undergoes continually enhanced emission as the number of trapped

electrons in donors (DX centres) increases with time [18]. This means that a net capture process will have a negative feedback (NF) or “shutter” due to (i) increasing emission as the number of donors able to emit electrons to the CB increases with t and (ii) decreasing capture as the number of donors able to capture electrons from the CB decreases with t . The transient thus produced ends when the rising emission counterbalances the decreasing capture, the whole process being expressed by Equation (3) of [18]. This is a Riccati equation, where capture is proportional to the square of the free electron concentration $n^2(t)$ because the concentrations of free electrons $n(t)$ and empty donors are equal under the boundary condition of charge neutrality, preventing the electron gas from escaping during capture. In searching for the counterpart of this Riccati equation for the emission-capture processes, maintaining the average charge density $qN_F C/\text{cm}^2$ on the surface of GaN, we have

$$\frac{\partial N_F}{\partial t} = \text{CA} - \text{EM} \approx c_n \times N_S \times n \times \exp\left(\frac{-q\phi}{kT}\right) - \frac{N_F(t)}{\tau}. \quad (3)$$

Equation (3) has been simplified for clarity by considering an SE density that is much higher than the occupied SE density ($N_S \gg N_F$). Although we will not solve this nonlinear equation here, we will say that the emission-capture process it represents features an *NF* mechanism through which it is difficult to terminate its transients because, added to the increasing emission and decreasing capture during the transient, each electron captured at instant t increases the capture barrier, thus greatly reducing the ability of the system to make further captures. By this we mean that electrons captured at instant m do not linearly reduce the capture at instant $(m + 1)$ as reported in [18]. Capture at instant $(m + 1)$ is reduced exponentially, thus producing a more brusque termination of the emission-capture transient than that under the conditions described in [18]. We could say that the *NF* or shutter ending the transients of DX centres is “soft,” whereas the shutter ending the surface-related transients in Figure 1 is “very brusque.”

In the log-lin plot shown in Figure 3, whose slope shows the time departure of the aforementioned net-capture transients from pure exponential decays (straight lines in this plot), the “set of slopes” (instantaneous lifetimes) for (3) solved for an SBB $q\phi \approx 1.2$ eV is wider than those shown in Figure 2 of [18]. This has been sketched in Figure 3 to illustrate why surface-related transients in GaN devices such as HFETs have to be fitted by stretched exponentials [15]. This would be a typical signature of these planar traps, where charge neutrality must be maintained for their DL during the transient and the capture barrier is modulated by trapped electrons as the surface $N_F(t)$ increases with t . This leads to transients that recall the left side of the bathtub curve widely used in reliability engineering (see Figures 8 and 9 of [15] for example) when they are viewed with linear axis.

Equating (3) to zero means that the emission flux is counterbalanced by the capture flux on average because the exact balance at each instant is impossible when the emission and capture processes are uncorrelated at this level. Therefore,

the reduction in τ due to optical emission reinforcing thermal emission will reduce N_F , thus leading to a slightly lower capture barrier (e.g., a thinner DL), and the conductance of two-terminal devices using the GaN epilayer as their conducting channel will rise as we have assumed. This can be verified by reducing τ to $\alpha\tau$ ($\alpha < 1$). If we maintain the density N_F of occupied SEs in TE, the higher EM that results will require a lower capture barrier under illumination to be counterbalanced and thus a lower N_F as we have assumed. Therefore, the number of occupied SEs (N_F)_{PC} of the n-GaN device under the weak illumination of the PC system is $(N_F/N_S)_{PC} < (N_F/N_S)_{TE}$, which requires a lower depleted thickness W , which produces the PC signal. The low photovoltage V_{ph} we have assumed in Figure 1(a) as a good approximation of Figure 1(b) in PC experiments is derived from the fact that $V_{ph} \approx 18$ mV at room temperature would be enough to counterbalance twice the thermal emission at room temperature, which is hard to believe under the weak light of the PC system. Therefore, we can assume confidently that $V_{ph} \ll \phi$ for the SBB $q\phi \approx 1.2$ eV, which our model uses to explain the PC data of [3] and the YB of n-GaN in the next Section.

3. Surface-Assisted Luminescence in N-Type GaN Devices

The photoluminescence (PL) spectrum of n-GaN samples shows a rather weak yellow band (YB) centred approximately 2.2 eV, such as that shown in Figure 3(a) of [7], where this YB was explained as being due to transitions of electrons from the CB to a deep level lying at 1 eV from the VB. To explain the other proposal we had for this YB, Figure 1(b) shows the band diagram of Device no. 1 and Device no. 0 existing in an n-GaN sample used in PL experiments under the strong illumination of the PL laser. As it is quite well known, photons creating electron-hole pairs in GaN reduce its SBB [1, 2] (see also Section 18-B-2 of [17]). This barrier reduction, which will increase the flux of electrons from the n-GaN bulk towards the surface, is due to a smaller depletion thickness W that has a lower positive charge under the surface. Due to the dipolar nature of the DL, this requires a reduction in the negative charge at the surface, thus suggesting a lower occupation of the N_S SE at the surface than in TE: $(N_F/N_S)_{PL} < (N_F/N_S)_{TE}$.

This lower occupation of the SE contradicts the higher capture flux that appears when the SBB is reduced. This higher capture should produce the opposite result: the SE should be more occupied than in TE because the thermal capture over this weakened capture barrier (e.g., over the lower SBB) simply means that the rate of electrons spilling over SE is higher. ‘‘Spilling’’ reflects the ‘‘electron fall over empty SE’’ under these conditions, where, beyond the capture barrier, the high flux of electrons arriving at the surface can be trapped by any SE, including those between E_{F_S} and the bottom of the CB, which were ‘‘empty’’ under TE and under the weak illumination of the PC system for photons with energy $h\nu < E_g$. They are also empty in the PC system because the weak light power handled in PC experiments is likely unable to induce a noticeable ‘‘pumping action’’ over the thermal activity, which makes the imref E_{F_S} a kind of

sharp borderline that separates the occupied SEs below E_{F_S} from the empty SEs above E_{F_S} ; however, this will change under the strong illumination of the PL laser, as will be discussed.

Going back to the increased capture under PL conditions, let us consider how a higher occupation of SEs, as this capture suggests $(N_F/N_S)_{PL} > (N_F/N_S)_{TE}$, with a lower negative charge density at the surface is required to reduce the capture barrier or to flatten the SBB to some extent. The key element to achieve this in Device no. 1 is the screening effect of holes swept towards the surface by the electric field of the SBB. Taking N_H cm⁻² as the sheet density of holes accumulated at the surface, the negative sheet charge at the surface becomes $-(qN_F)_{PL} + (qN_H)$. In this way, the trapped charge at SEs can be higher than in TE if there are enough accumulated holes. This solves the electrostatic problem, making a reduction in SBB with a higher N_F possible, but it opens a new way to reduce N_F , which is through the possible recombination of these electrons trapped in SEs with those holes accumulated in the surface as well.

This recombination, or in better terms its radiative part observed in PL, is the other proposal we formulated in 1997 to explain the origin of the weak YB observed in [7], which we will now justify. From Figure 3 of [7], where this YB was magnified by 500 times, we can say that this recombination is very weak; otherwise, such yellow emission would be strong enough to make efficient yellow emitters from n-GaN material. We will later discuss the reason for this weakness. Therefore, we can assume that holes accumulated at the surface of n-GaN do not noticeably affect the lifetime of electrons trapped in SEs under PL conditions such that the increased capture would lead to the aforementioned $(N_F/N_S)_{PL} > (N_F/N_S)_{TE}$ condition by the screening effect of N_H . This accumulation of holes at the surface allows for the lower SBB shown in Figure 1(b) due to some photovoltage V_{ph} that reduces the capture barrier to $q(\phi - V_{ph})$ eV. In this way, the emission and capture fluxes mutually counterbalanced in a steady state during the PL experiment at the surface are higher than those in TE.

It is worth noting that the N_F electrons/cm² trapped at the surface can be higher than those in TE as explained or lower than those in TE because this depends on N_H and therefore on the laser illumination power. What matters is to realise that we have N_F and N_H in close proximity at the surface, and the next point to consider is the effect of the optical emission of the PL laser emptying SEs lying below the imref E_{F_S} in Figure 1(b). This has to do with the ‘‘pumping action’’ mentioned previously in this section. Under the strong light of the PL laser, we cannot assume that the pumping action is negligible with respect to the thermal activity, which we assumed under the weak light of the PC system. Under PL conditions, we could expect a noticeable pumping of electrons trapped in SEs under the imref E_{F_S} , which would become a less sharp borderline than in TE between occupied SEs below E_{F_S} and empty SEs above E_{F_S} . Instead, we should expect a broader transition band in energy, likely centred at E_{F_S} , separating the occupied SEs well below E_{F_S} from empty SEs well above E_{F_S} due to the aforementioned spillover of

electrons being captured over the new barrier (e.g., the SBB lowered by the PL laser light).

The strong illumination of the PL laser not only suggests a local heating of the sample but also the possibility of a high efficiency of the PL laser to empty SEs to achieve a flat band condition by greatly reducing N_F . If this were so, the SBB would disappear without the help of holes at the surface. In this case, the bands would be flat during the PL experiment, and we would only obtain the PL spectrum of GaN from to band-to-band transitions with energy close to the bandgap $E_g \approx 3.41$ eV at room temperature, and no YB would be found in this case. Under this hypothetical flat-band condition, the capture barrier would be null, and a huge flux of electrons would reach the surface from the GaN bulk to occupy SEs efficiently emptied by the laser pumping action. This is hard to believe, however, because photons can increase the energy of electrons trapped in SEs (e.g., vertical transitions in energy), but they are unable to transport the negative charge of all of these electrons accumulated at the surface.

The negative charge of electrons thus accumulated at the surface would produce an SBB sweeping them towards the GaN bulk, while other electrons from the bulk would be trapped over this SBB by SEs to be pumped subsequently by the laser. This would generate an SBB that contradicts the flat-band condition we have used as a starting point of this reasoning and will not be considered further, although a careful study of the power ratio P_{YB}/P_{PL} between the power of the yellow band P_{YB} and that of the PL spectrum expected for the n-GaN material could provide additional information about all of these processes related to Device no. 1 at the surface of n-GaN. Concerning the flattening of the SBB, we can say that V_{ph} will be low because the hole charge N_H accumulated at the surface cannot be increased without limit because as it increases, the depth of the well for holes at the surface diminishes, allowing holes to escape. If $V_{ph} \approx 18$ mV at room temperature, the net capture and net emission would be doubled. Assuming that $(N_F/N_S)_{PL} \approx (N_F/N_S)_{TE}$, this doubled emission would derive from $(N_F)_{PL} \approx 2(N_F)_{TE}$ (see (2)), which in turn would require $N_H \approx (N_F)_{TE}$ to keep a SBB close to that in TE. This N_H value starts to fill the well shown in Figure 1(b) for holes. In other words, the N_H charge able to accumulate at the surface is limited, and this fact together with the need for an appreciable SBB to transport electrons from the surface towards the bulk (recall that photons cannot transport them) limits V_{ph} during the PL experiment.

It is worth noting that the band diagrams of Figure 1 apply to our undoped wurtzite GaN layers of [7], whose residual doping was n-type in the 10^{17} – 10^{18} cm $^{-3}$ range. This means that the ratio $(N_F/N_S)_{PL}$ of [7] during the PL experiments was most likely higher than in TE or that the SEs of the n-GaN during our PL experiments were likely more occupied than in TE due to photogenerated holes swept towards the surface, as shown in Figure 1(b). Device no. 1 features many electrons in SEs and many holes in close proximity, which leads us to consider the emission with carrier interaction described in Section 6-D-2-e of [17], where a photon with energy $h\nu < E_g$

was produced when an electron of the CB made “a transition to a *virtual state* **a** at an energy ΔE below the CB by exciting an electron inside the CB to a higher-energy state (this causes a change in momentum). The first electron completes the transition from state **a** to the VB by emitting a photon $h\nu$.”

Again from [17], we “note that momentum-conservation rules make this process difficult to observe in pure direct-bandgap semiconductors since an additional phonon may be needed. . . then the transition becomes a three-step process having a very low probability of occurrence.” In Figure 1(b), however, we do not need a third electron promoted to a higher state of energy to have electrons in virtual states (VSs) because electrons trapped in SEs can reach VSs close to the surface by tunnelling through thin barriers whose heights are not far from the SBB (see Figure 1(b)). Hence, the small fraction of $(N_F)_{PL}$ electrons reaching VSs in a region abundant with holes would complete the transition to the VB by emitting photons with energy $h\nu < E_g$.

These photons would peak at an energy $E_{peak} \approx 2.2$ eV; this value is derived from the difference $E_g - q\phi \approx 2.21$ eV that appears by using $q\phi \approx 1.2$ eV for the n-GaN we obtained from the PC data of [2] in Section 2; moreover, the quasi-Fermi level of the SE system (E_{Fs}) will not vary much with respect to its value in TE (E_F) because V_{ph} is low, as explained previously, and N_S is much higher than N_F . This high N_S in GaN seems likely because if it was low, no relevant negative floating gate would appear in FETs [13] and no passivation of their surfaces would be required. The YB for energies higher than 2.2 eV would be due to those SEs filled above E_{Fs} in combination with the “pumping action” of the PL laser emptying some SEs below E_{Fs} and the filling of SEs above E_{Fs} by the enhanced capture. Those electrons in SEs above E_{Fs} would tunnel to VS with a higher probability than electrons in SEs below E_{Fs} , which are much more numerous, however, due to the exponential dependence of $N_S(E)$. From the product of this occupation density of SEs and the probability of electrons in these SEs of tunnelling to VS, a peak energy not far from E_{Fs} would result, thus giving rise to a peak in the YB around $E_{peak} \approx 2.2$ eV.

This would be the origin of the YB peak observed in the PL spectrum of n-GaN in Figure 3 of [7], whose oscillating character around E_{peak} could reveal an oscillating behaviour of the tunnelling probability of these electrons with respect to their corresponding virtual states or an interference-related phenomenon requiring further study. In any case, this surface-assisted luminescence (SAL) is the plausible reason we have formulated for the YB peaking at ≈ 2.2 eV in the PL of n-GaN samples. Because this SAL is due to electrons trapped in SEs like those forming the negative floating gate of n-GaN FETs in the dark [13], it allows for the prediction of surface electroluminescence (SEL) when holes are injected near the surface of GaN devices, as has been observed recently in n-GaN FETs [10, 11]. In these studies, the SEL has been attributed to “hot-electron effects” due to its decay with photon energy, which closely tracks the $N_S(E)$ that we obtained in Section 2 from the PC results of [3], as will be discussed in the next section.

4. Surface Electroluminescence in N-Type GaN Devices and Other Effects

The surface-related origin of the SAL known to explain the YB of GaN not only agrees with many studies linking this YB to the surface [19–23] but also allows for the prediction that if holes are brought near the surface in n-GaN devices, surface electroluminescence (SEL) proportional to the surface charge N_F will be observed. Let us show that this SEL is very likely the weak EL found recently in the FET devices of [10, 11], where it has been attributed to hot-electron effects. Using our model for Device no. 1 at the surface, we do not need hot-electron effects at all, in agreement with recent studies discarding these types of effects in the electrical degradation of GaN FETs [24]. Our model also predicts that this SEL will track the dynamics of the surface charge N_F in n-GaN devices and that this SEL will not be a yellow peak but a “redder” luminescence.

Recalling the role of Device no. 1 in the formation of the negative floating gate (NFG) that collapses these FETs [13], we can explain why this SEL is first observed in the gate side towards the drain of field-effect devices for moderate drain voltages V_{DS} [10] and why it moves towards the drain contact if the voltage V_{DS} is increased further [11]. Due to the positive feedback (PF) that underlies this electrical degradation and the subsequent collapse of GaN FETs [13], this SEL will appear near the drain only after some delay and after surpassing a threshold voltage V_{DS} representing the onset of the electrical degradation. This delay has been reported in [11], and the threshold was reported in [24]. These two features—a delay to allow the PF to build the collapse and a threshold to trigger this degradation—leading to collapse are familiar features of circuits with PF, such as the one proposed in [13] ten years ago for the electrical degradation collapsing GaN FETs. Thus, the time evolution of this SEL for large V_{DS} [11] gives strong support to our model based on surface Device no. 1, which applies to different phenomena such as the PC response of [3], the YB of [7], and the SEL of [10, 11].

Regarding its “colour,” this SEL will not peak like the YB because there is no “pumping action” of a laser in [10, 11] as it occurs in the PL when the YB appears. The FET-like devices of [10, 11] were placed in the dark to observe their weak EL, which only appears when holes are injected near the GaN surface. Therefore, the spectrum of their SEL will reflect the exponential increase in $N_S(E)$ as we go from the CB to the VB in Figure 4, which is the counterpart of Figure 2 for surface Device no. 1 acting as a photon emitter and not as the photon absorber it was in Figure 2. Hence, this SEL will not peak at $E_{\text{peak}} \approx 2.2$ eV as the YB of the PL does. Instead, it will show an exponential decay in intensity as the energy of the emitted photons increases. To be precise, this SEL has to show an intensity proportional to $\exp(-h\nu/E_0)$; thus, it will possess the same slope α shown in Figure 2, though decreasing with photon energy $h\nu$ because the density $N_S(E)$ in the GaN surface decreases as $\exp(-h\nu/E_0)$ when we go from the VB to the CB. This $N_S(E) \propto \exp(-h\nu/E_0)$ was obtained in Section 2 from the PC data of [3] obtained 17 years ago, and this SEL observed recently in [10, 11] is the empirical proof we promised in Section 2 of its validity, which is ensured

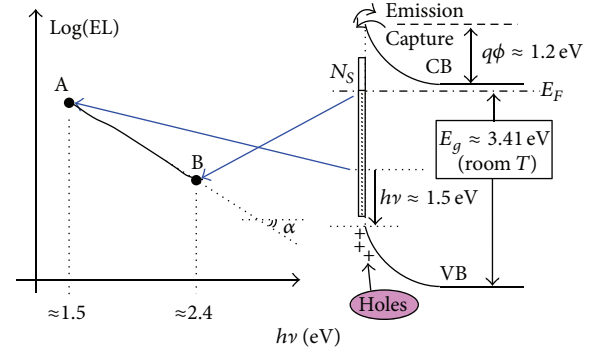


FIGURE 4: Semilog plot of the surface luminescence spectrum that must appear in n-GaN devices when holes are injected near their surface. Electrons in surface states (SE) using virtual states to accomplish radiative transitions to the valence band (see text) would reflect the exponential distribution with the energy of the SEs.

when we consider that E_0 was between 230 meV and 280 meV [3]. Figure 4 shows a sketch of the weak EL spectrum shown in Figure 3(b) of [10].

For $E_0 = 230$ meV, we have $E_0 \approx 2600$ K which means that the slope of Figure 4 will be $\text{tg}(\alpha) = -1/E_0$, as if this SEL was the EL derived from a hot-electron gas at $T_{\text{eq}} \approx 2600$ K. This is the explanation provided in [10] for the decay of the weak EL the authors observed with this T_{eq} . Unaware of the Device no. 1 existing at n-GaN surfaces, these authors propose that the weak EL they observe is derived from a hot-electron gas in the GaN channel at this $T_{\text{eq}} \approx 2600$ K, an effect that our model does not require at all. This T_{eq} in [10] confirms that the PC data of [3], with a proper model for Device no. 1, reveal the density of surface states at the surface of n-GaN devices, as we have proposed. This is good proof of the validity of the relationship $N_S(E) \propto \exp(-h\nu/E_0)$ derived using our model from the PC data obtained long ago [3], though it has not been well understood until now. Although the time evolution of this SEL moving from the gate contact to drain one after some delay from the application of a sufficiently high V_{DS} [11] provides additional proof about the origin and usefulness of this SEL as a marker for surface charge in n-GaN devices, we will consider this point further due to the space constraint of this paper.

5. Conclusions

The physical relevance of the devices used in measurements must be considered before assigning properties to bulk materials. All hypotheses used to assign the result of a measurement of a device to a property of a bulk material must be verified. This forces researchers to consider the devices associated with the surfaces and interfaces of actual materials, and only after having taken their effects into account can we consider their finite volume (Device no. 0) as a good model for a continuous medium or infinite volume of these materials.

The yellow band assigned to GaN is better understood if we consider it as the surface-assisted luminescence of n-GaN

due to the unintentional Device no. 1 existing at its surface. Device no. 1 also helps to understand the photoconductance response of 2TDs made from n-GaN materials, especially at low illumination levels. Finally, the same surface Device no. 1 allows for the prediction and thus the explanation of the weak electroluminescence found in n-GaN devices when holes are injected near their surfaces. Device no. 1 at the surface of GaN provides a unified view of the luminescence phenomena of this material, which is difficult to obtain using other models that are unaware of this surface device.

Acknowledgments

This work is supported by the Spanish CICYT under the MAT2010-18933 Project, by the Comunidad Autónoma de Madrid through its IV-PRICIT Program, and by the E. U. Project no. 304814 RAPTADIAG.

References

- [1] J. I. Izpura and E. Muñoz, "Epitaxial photoconductive detectors: a kind of photo-FET device," in *Proceedings of the Advanced Workshop on Frontiers in Electronics (WOFE '97)*, pp. 73–80, January 1997.
- [2] I. Izpura, J. F. Valtueña, and E. Muñoz, "Surface band-bending assessment by photocurrent techniques. Application to III-V semiconductors," *Semiconductor Science and Technology*, vol. 12, pp. 678–686, 1997.
- [3] C. H. Qiu, C. Hoggatt, W. Melton, M. W. Leksono, and J. I. Pankove, "Study of defect states in GaN films by photoconductivity measurement," *Applied Physics Letters*, vol. 66, pp. 2712–2714, 1995.
- [4] J.-I. Izpura, "1/f Electrical noise in planar resistors: the joint effect of a backgating noise and an instrumental disturbance," *IEEE Transactions on Instrumentation and Measurement*, vol. 57, no. 3, pp. 509–517, 2008.
- [5] J. I. Izpura, "On the electrical origin of flicker noise in vacuum devices," *IEEE Transactions on Instrumentation and Measurement*, vol. 58, no. 10, pp. 3592–3601, 2009.
- [6] J. I. Izpura and J. Malo, "Thermodynamical phase noise in oscillators based on L-C resonators (Foundations)," *Circuits and Systems*, vol. 3, pp. 48–60, 2011.
- [7] E. Calleja, F. J. Sánchez, D. Basak et al., "Yellow luminescence and related deep states in undoped GaN," *Physical Review B*, vol. 55, no. 7, pp. 4689–4694, 1997.
- [8] J. I. Izpura and J. Malo, "A fluctuation-dissipation model for electrical noise," *Circuits and Systems*, vol. 2, no. 3, pp. 112–120, 2011.
- [9] H. B. Callen and T. A. Welton, "Irreversibility and generalized noise," *Physical Review*, vol. 83, no. 1, pp. 34–40, 1951.
- [10] M. Meneghini, M. Scamperle, M. Pavese et al., "Electron and hole-related luminescence processes in gate injection transistors," *Applied Physics Letters*, vol. 97, no. 3, Article ID 033506, 3 pages, 2010.
- [11] M. Meneghini, C. de Santi, T. Ueda et al., "Electron and hole-related luminescence processes in gate injection transistors," *IEEE Electron Device Letters*, vol. 33, pp. 375–377, 2012.
- [12] J. I. Izpura and J. Malo, "1/f Noise enhancement in GaAs," in *Proceedings of the 18th International Conference on Noise and Fluctuations (ICNF '05)*, AIP Conference Proceedings, pp. 113–116, September 2005.
- [13] J. I. Izpura, "Drain current collapse in GaN metal-semiconductor field-effect transistors due to surface band-bending effects," *Semiconductor Science and Technology*, vol. 17, no. 12, pp. 1293–1301, 2002.
- [14] L. K. J. Vandamme and F. N. Hooge, "What do we certainly know about 1/f noise in MOSTs?" *IEEE Transactions on Electron Devices*, vol. 55, no. 11, pp. 3070–3085, 2008.
- [15] R. Vetury, N. Q. Zhang, S. Keller, and U. K. Mishra, "The impact of surface states on the DC and RF characteristics of AlGaIn/GaN HFETs," *IEEE Transactions on Electron Devices*, vol. 48, no. 3, pp. 560–566, 2001.
- [16] R. E. Williams, *Gallium Arsenide Processing Techniques*, Artech House, Dedham, Mass, USA, 1984.
- [17] J. I. Pankove, *Optical Processes in Semiconductors*, Dover, New York, NY, USA, 1975.
- [18] I. Izpura and E. Muñoz, "Electron capture by DX centers in AlGaAs and related compounds," *Applied Physics Letters*, vol. 55, no. 17, pp. 1732–1734, 1989.
- [19] I. Shalish, L. Kronik, G. Segal et al., "Yellow luminescence and related deep levels in unintentionally doped GaN films," *Physical Review B*, vol. 59, no. 15, pp. 9748–9751, 1999.
- [20] I. Shalish, L. Kronik, G. Segal, Y. Shapira, M. Eizenberg, and J. Salzman, "Yellow luminescence and Fermi level pinning in GaN layers," *Applied Physics Letters*, vol. 77, no. 7, pp. 987–989, 2000.
- [21] M. A. Reshchikov, "Strong suppression of the yellow luminescence in C-doped GaN in air ambient," *Applied Physics Letters*, vol. 89, no. 23, Article ID 232106, 3 pages, 2006.
- [22] Z. L. Fang, J. Y. Kang, and W. Z. Shen, "Surface modification and significant reduction of yellow/blue luminescence of gallium nitride," *Journal of Physical Chemistry C*, vol. 112, no. 45, pp. 17652–17656, 2008.
- [23] H. Chen, C.-H. Kao, Y.-C. Chen et al., "Passivation of yellow luminescence defects in GaN film by annealing and CF₄ plasma treatment," *Journal of Optoelectronics and Advanced Materials*, vol. 13, no. 8, pp. 973–975, 2011.
- [24] J. Joh and J. A. del Alamo, "Critical voltage for electrical degradation of GaN high-electron mobility transistors," *IEEE Electron Device Letters*, vol. 29, no. 4, pp. 287–289, 2008.

Research Article

Electronic Structure Calculations of $A_2Ti_2O_7$ ($A = Dy, Ho, \text{ and } Y$)

H. Y. Xiao

School of Physical Electronics, University of Electronic Science and Technology of China, Chengdu 610054, China

Correspondence should be addressed to H. Y. Xiao; hyxiao@uestc.edu.cn

Received 8 July 2013; Accepted 30 July 2013

Academic Editor: Liang Qiao

Copyright © 2013 H. Y. Xiao. This is an open access article distributed under the Creative Commons Attribution License, which permits unrestricted use, distribution, and reproduction in any medium, provided the original work is properly cited.

Ab initio calculations have been performed on titanate pyrochlores $A_2Ti_2O_7$ ($A = Dy, Ho, \text{ and } Y$) to investigate their electronic structures. The generalized gradient approximation (GGA) + U formalism has been used to correct the strong onsite Coulomb repulsion between the localized 4f electrons. The effects of effective U values on the structural and electronic properties of $A_2Ti_2O_7$ ($A = Dy, Ho, \text{ and } Y$) have been discussed. It is shown that $Dy_2Ti_2O_7$ and $Ho_2Ti_2O_7$ exhibit different electronic structures from $Y_2Ti_2O_7$. The strong interaction between Dy and Ho 4f electrons and O 2p orbitals may increase the covalency of (Dy–O) and (Ho–O) bonds and decrease their irradiation resistance.

1. Introduction

Materials with the $A_2B_2O_7$ pyrochlore structure have wide ranges of composition that lead to remarkable properties and wide variations in ionic and electronic conductivity, catalytic activity, and electrooptic and piezoelectric behavior [1]. Because they can be used to immobilize actinides [2–5], the pyrochlores have attracted significant attention both theoretically and experimentally [6–21]. In $A_2B_2O_7$ pyrochlore structure, the A and B cations occupy the 16d (0.5, 0.5, 0.5) and 16c (0, 0, 0) sites, respectively, and the oxygens are in the 48f ($x, 0.125, 0.125$) and 8b (0.375, 0.375, 0.375) positions (using the Wyckoff notation) [22]. Single crystals of the $A_2Ti_2O_7$ pyrochlores ($A = Sm \text{ to } Lu \text{ and } Y$) have been irradiated by 1 MeV Kr^+ ions, and their microstructural evolutions as a function of increasing radiation dose have been characterized [7]. A slight deviation from the monotonic trend of critical amorphization temperature T_c versus the ionic radius was observed for $Y_2Ti_2O_7$. T_c is frequently used as a measurement of the resistance of a material to amorphization, and lower values of T_c are the result of substantial dynamic annealing occurring during irradiation, which allows the materials to remain in the crystalline state. Generally, pyrochlores that are closer to the ideal fluorite structures are more susceptible to the radiation-induced pyrochlore-to-defect fluorite structural transition. The defect

fluorite structure results from disordering of the A- and B-site cations, as well as the anion vacancies. Thus, pyrochlore compositions that are more easily disordered to the defect fluorite structure are more “resistant” to ion-beam-induced amorphization [7]. On the other hand, theoretical investigations reported by Sickafus et al. [18] have demonstrated that compounds with very dissimilar cationic radii (e.g., closer to the ideal pyrochlore structure, $x_{O48f} = 0.3125$) should exhibit the greatest susceptibility to structural destabilization (e.g., amorphization), whereas compounds with more similar radii (e.g., closer to the ideal fluorite structure) should behave more robustly in a radiation environment. For $A_2Ti_2O_7$ ($A = Dy, Ho, \text{ and } Y$), the ionic radius ratio (r_A/r_{Ti}) decreases monotonically. According to Sickafus’ point of view, the compounds should become more radiation resistant as the cation A varies from Dy to Ho. However, the critical amorphization temperatures were measured to be 910, 850, and 780 K for $Dy_2Ti_2O_7$, $Ho_2Ti_2O_7$, and $Y_2Ti_2O_7$ compounds, respectively [7], meaning that of these three compounds, $Y_2Ti_2O_7$ is the most radiation resistant. It is clear that cation radius ratio alone cannot be used to explain the different responses of these compositions to radiation.

To resolve the discrepancy between experimental observations and theoretical predictions, it is important to fundamentally understand the electronic structures of A-site elements and their effects on the stability of the pyrochlore

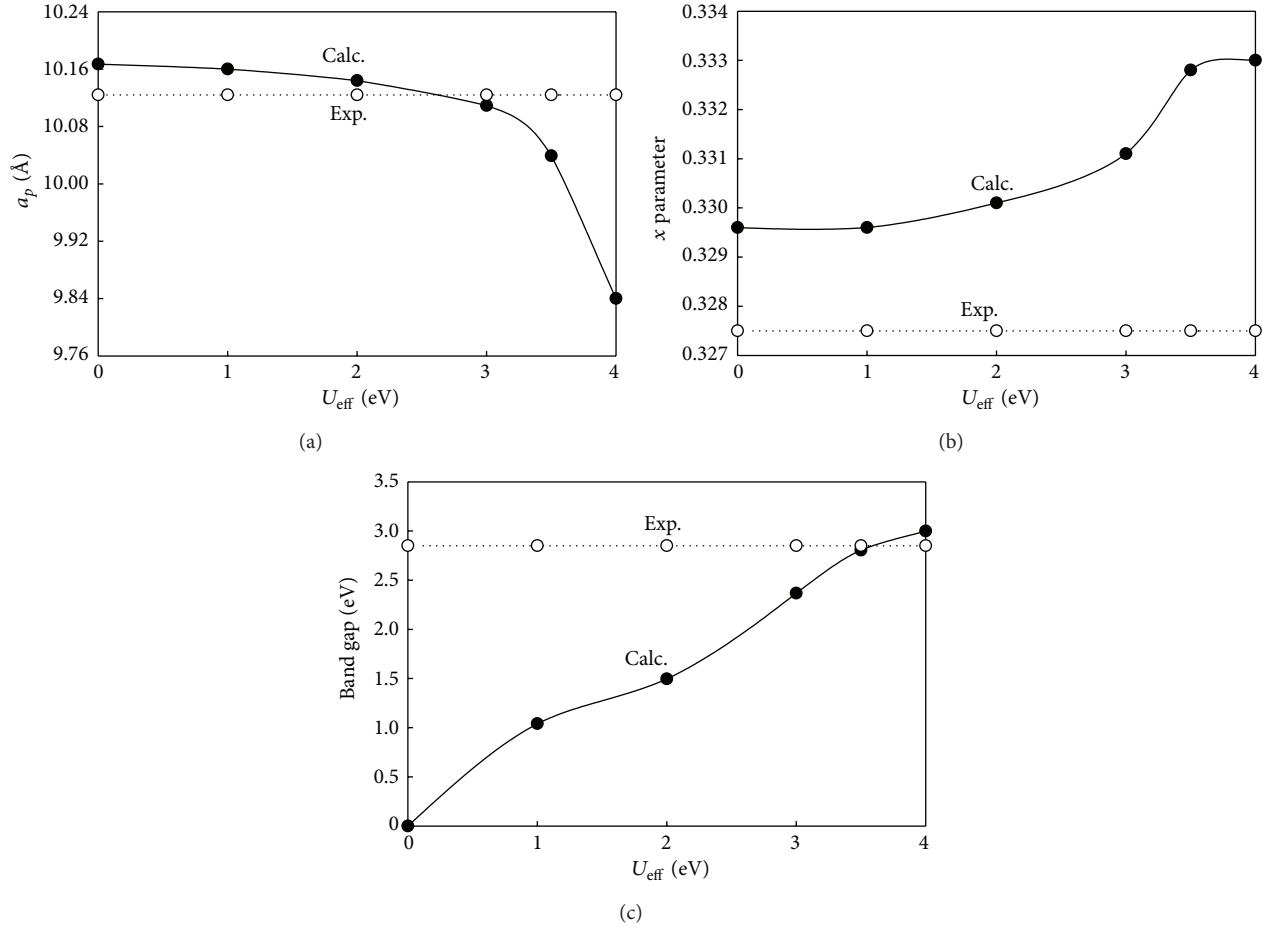


FIGURE 1: Dependence of the lattice parameter a_p (a), x (b), and band gap (c) of the $\text{Dy}_2\text{Ti}_2\text{O}_7$ on U_{eff} .

structure. In the present study, *ab initio* total energy calculations [17, 19, 23] based on density functional theory have been performed on $\text{A}_2\text{Ti}_2\text{O}_7$ ($A = \text{Dy}, \text{Ho}, \text{and Y}$) pyrochlores. GGA + U formalism has been used to account for the strong on-site Coulomb repulsion among the $4f$ electrons in $\text{Dy}_2\text{Ti}_2\text{O}_7$ and $\text{Ho}_2\text{Ti}_2\text{O}_7$. How the structural and electronic properties of $\text{A}_2\text{Ti}_2\text{O}_7$ ($A = \text{Dy}, \text{Ho}, \text{and Y}$) pyrochlores are affected by the choice of U is discussed. These calculations will provide significant insight into the effects of electronic configuration on the thermochemical stability of pyrochlore of different compositions.

2. Computational Method

All the calculations have been completed using the VASP code [24] with spin-polarized effects taken into account. A primitive unit cell containing 22 atoms was used for the present investigations, with a $4 \times 4 \times 4$ Monkhorst-Pack k -point mesh. The ion-electron interaction was described by PAW pseudopotentials with the following atomic valence configurations: Ti ($3s^2, 3p^6, 3d^2$, and $4s^2$), Y ($4s^2, 4p^6, 4d^1$, and $5s^2$), Dy ($5s^2, 5p^6, 4f^{10}$, and $6s^2$), and Ho ($5s^2, 5p^6, 4f^{11}$, and $6s^2$). The PBE functional within the generalized

gradient approximation was used to describe the exchange-correlation potential energy [25, 26], with the basis set for valence electrons consisting of plane waves with a cut-off energy of 400 eV. The calculations were performed based on ferromagnetic ordering of the magnetic moments and antiferromagnetic ordering, and spin ice model [27, 28] is not considered in the present work. The Hubbard U correction was introduced using the method proposed by Dudarev et al. [29], in which the Hubbard parameter U reflecting the strength of onsite Coulomb interaction and parameter J adjusting the strength of exchange interaction are combined into a single parameter $U_{\text{eff}} = U - J$.

3. Results and Discussion

3.1. Atomic and Electronic Structure of $\text{Dy}_2\text{Ti}_2\text{O}_7$. The pyrochlore structure can be completely described by the a -cell edge, a_p , and the $48f$ oxygen positional parameter, x . The dependence of the lattice parameter a_p , x , and band gap of the $\text{Dy}_2\text{Ti}_2\text{O}_7$ on U_{eff} is shown in Figures 1(a), 1(b), and 1(c), respectively. As shown in Figure 1, the structural parameter a_p decreases slightly for $U_{\text{eff}} \leq 3.0$ eV. Above this value, the parameter changes more significantly. A U_{eff} of 2.6 eV

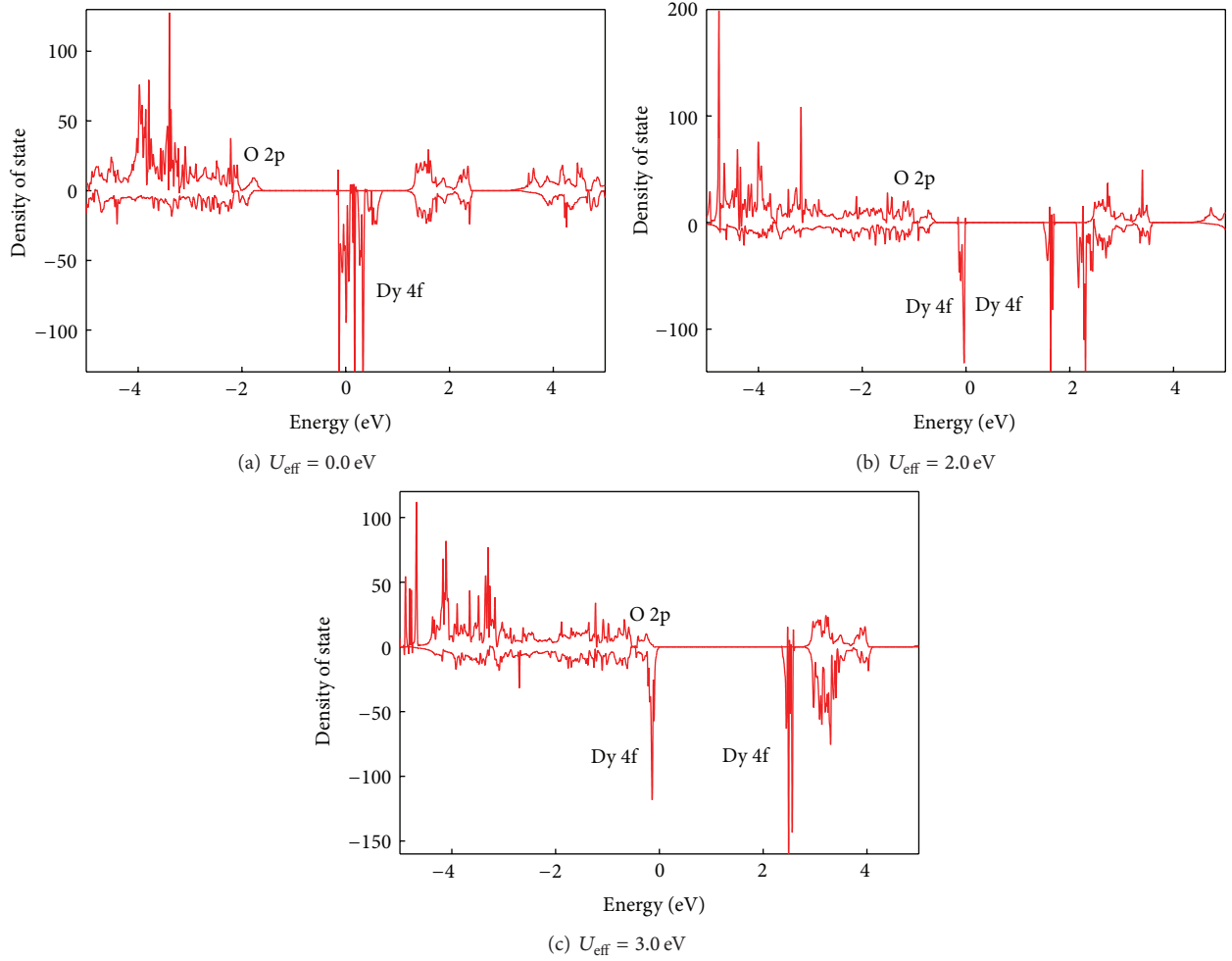


FIGURE 2: Total DOS distribution for $\text{Dy}_2\text{Ti}_2\text{O}_7$. (a) $U_{\text{eff}} = 0.0$ eV; (b) $U_{\text{eff}} = 2.0$ eV; and (c) $U_{\text{eff}} = 3.0$ eV. The upper and lower panels show the spin-up and spin-down channels, respectively.

yields a lattice constant of 10.12 \AA , in excellent agreement with experiments [7]. For O_{48f} positional parameter x , it deviates from experimental value of 0.3275 with increasing U_{eff} values; that is, introducing $U_{\text{eff}} > 0$ makes the deviation from the experiment larger. Concerning the band structure of $\text{Dy}_2\text{Ti}_2\text{O}_7$, a sharp increase of band gap value with growing U_{eff} is observed. For a certain U_{eff} value of around 3.5 eV, the band gap value of 2.85 eV matches the calculated optical band gaps performed by Nemoshkalenko et al. [30]. It is shown that the band gap of $\text{Dy}_2\text{Ti}_2\text{O}_7$ presents stronger dependence on the U_{eff} value than lattice parameters.

Figure 2 displays the total density of state (DOS) distribution of $\text{Dy}_2\text{Ti}_2\text{O}_7$ at $U_{\text{eff}} = 0, 2.0$, and 3.0 eV. The Fermi level is set to 0 eV. At the pure GGA level, the f band does not split but shows a large peak around the Fermi level, leading to a metallic ground state, which disagrees with experiments [31]. Obviously, the pure GGA calculation without modifying the intra-atomic Coulomb interaction gives wrong results. It is suggested that introduction of a penalty function which corrects the intraband Coulomb interaction by the Hubbard U parameter is necessary for strongly correlated systems

[32] such as $\text{Dy}_2\text{Ti}_2\text{O}_7$. If the U_{eff} is increased to 2 eV, the f bands undergo splitting, and a semiconducting solution with a finite separation of the occupied and unoccupied f band is found. The obtained band gap between the valence band edge (contributed by Dy $4f$) and the bottom of the conduction band (contributed by Dy $4f$) is 1.53 eV. In the case of $U_{\text{eff}} = 3$ eV, the unoccupied f bands shift toward higher energy level, resulting in a larger band gap value of 2.36 eV. A notable difference between the cases of $U_{\text{eff}} = 2.0$ eV and $U_{\text{eff}} = 3.0$ eV is that there is no mixture between the occupied f bands and the O $2p$ orbitals in the valence region at $U_{\text{eff}} = 2.0$ eV, whereas the occupied f bands become hybridized with the O $2p$ orbitals in the valence region at $U_{\text{eff}} = 3.0$ eV.

3.2. Atomic and Electronic Structure of $\text{Ho}_2\text{Ti}_2\text{O}_7$. Figure 3 shows the lattice parameters and band gaps of the $\text{Ho}_2\text{Ti}_2\text{O}_7$ as a function of U_{eff} . Generally, $\text{Ho}_2\text{Ti}_2\text{O}_7$ shows similar dependence on the effective U values to the case of $\text{Dy}_2\text{Ti}_2\text{O}_7$. The lattice constants decrease with increasing U_{eff} , and the reason for this behavior is a slight hybridization of Ho $4f$ and

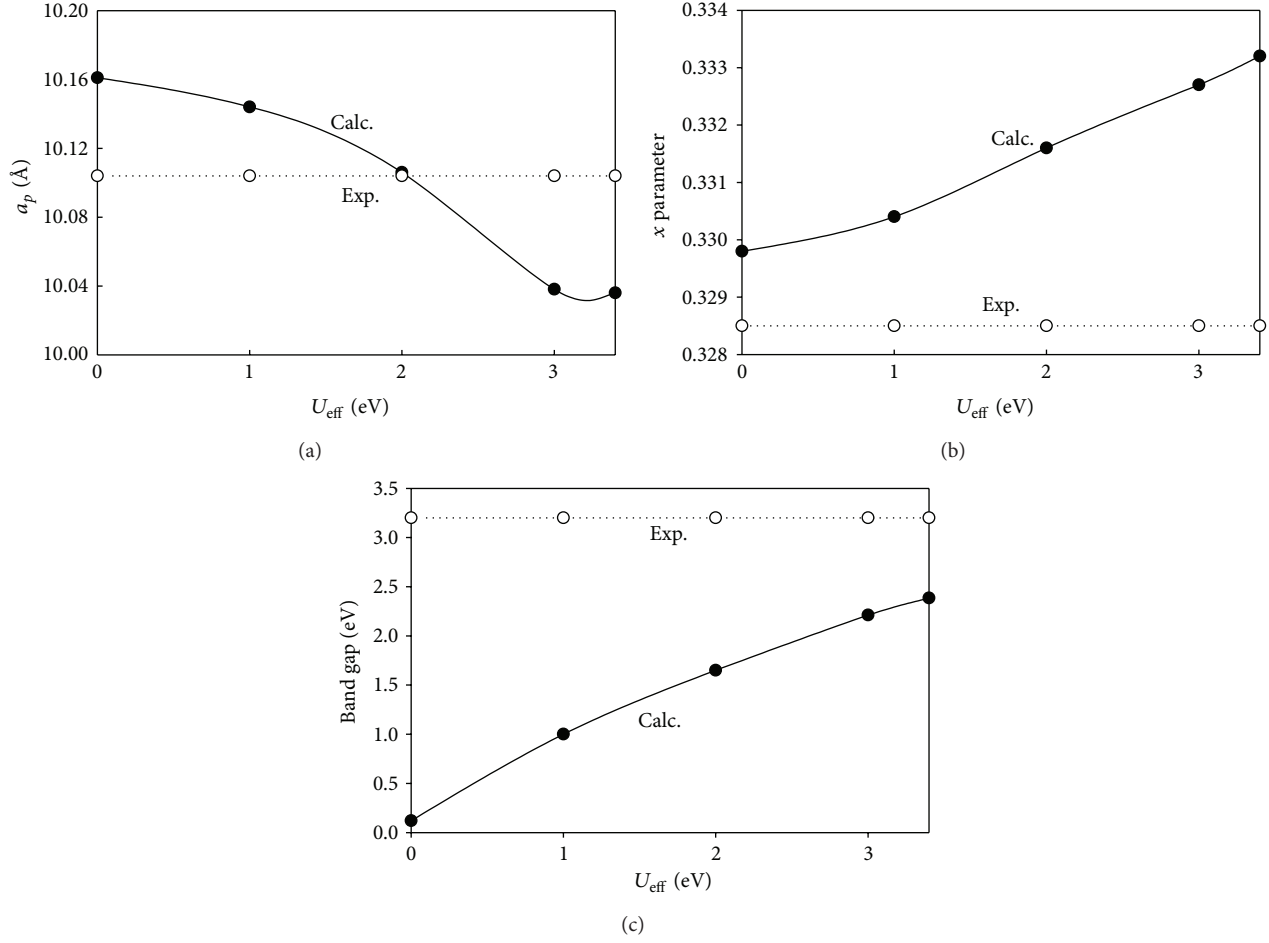


FIGURE 3: Dependence of the lattice parameter a_p (a), x (b), and band gap (c) of the $\text{Ho}_2\text{Ti}_2\text{O}_7$ on U_{eff} .

O 2p orbitals. The experimental lattice constant [7] of 10.104 Å is obtained for $U_{\text{eff}} = 2$ eV. For the O_{48f} positional parameter, it deviates from experimental value of 0.3285 with increasing U_{eff} values. As compared with $\text{Dy}_2\text{Ti}_2\text{O}_7$, the band gap value increases less significantly with U_{eff} . At $U_{\text{eff}} = 3$ eV, the band gap of $\text{Ho}_2\text{Ti}_2\text{O}_7$ is still 0.82 eV smaller than experimental measurement of 3.2 eV [33].

Figure 4 presents the total DOS of $\text{Ho}_2\text{Ti}_2\text{O}_7$ at $U_{\text{eff}} = 0, 2.0,$ and 3.0 eV. At $U_{\text{eff}} = 0$ eV, the pure GGA calculation without modifying the intra-atomic Coulomb interaction yields a metallic ground state, in contrast to experiments [33]. As the U_{eff} is increased to 2 eV, the f bands splits, and the occupied and unoccupied f band contributes significantly to the valence bands and conduction bands, respectively. The corresponding band gap between the valence band edge and the bottom of the conduction band is 1.65 eV. Different from the total DOS distribution of $\text{Dy}_2\text{Ti}_2\text{O}_7$ at $U_{\text{eff}} = 2$ eV, the occupied f bands hybridize with O 2p orbitals in the valence region. At $U_{\text{eff}} = 3$ eV, it is noted that the main effect of increasing U_{eff} value is to push the unoccupied f bands toward higher energy level, resulting in a larger band gap value of 2.38 eV.

3.3. Atomic and Electronic Structure of $\text{Y}_2\text{Ti}_2\text{O}_7$. Yttrium titanate pyrochlore is an important member of pyrochlore family, and it is often served as a model system for pyrochlores because of its simple electronic structure [12]; that is, no f electrons exist in $\text{Y}_2\text{Ti}_2\text{O}_7$. For this composition, GGA + U method has also been employed to study if the intra-atomic electron correlations are important for Y-4d states. In Figure 5, we plot the equilibrium lattice parameters and band gap value of $\text{Y}_2\text{Ti}_2\text{O}_7$ as functions of U_{eff} . As shown in the figure, the lattice constant a_p and O_{48f} positional parameter deviate from experimental values of 10.1 Å and 0.33 [7] with increasing U_{eff} values. Specially, the choice of U_{eff} values has almost no effects on the band gap values. It is indicated that the intra-atomic electron correlations are negligible for Y-4d states in $\text{Y}_2\text{Ti}_2\text{O}_7$.

The total DOS distribution of $\text{Y}_2\text{Ti}_2\text{O}_7$ at $U_{\text{eff}} = 0.0$ eV is presented in Figure 6. The valence bands mainly consist of O 2p orbitals with small contribution from Ti 3d states, and the conduction bands are mainly composed of Ti 3d states hybridized with O 2p orbitals. The corresponding band gap is 2.82 eV, in excellent agreement with the calculated value of 2.84 eV reported by Jiang et al. [34]. This value is 0.32 eV

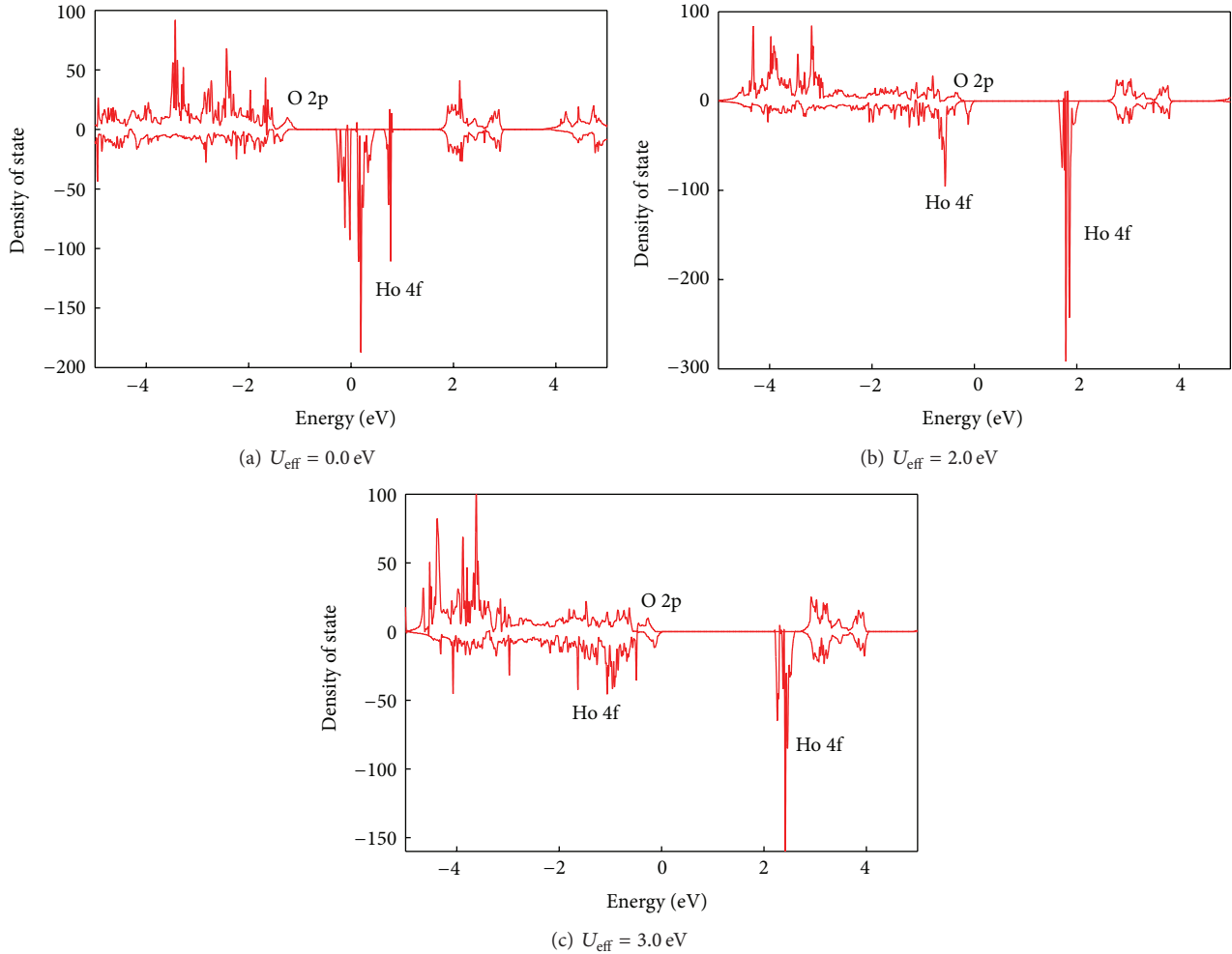


FIGURE 4: Total DOS distribution for $\text{Ho}_2\text{Ti}_2\text{O}_7$. (a) $U_{\text{eff}} = 0.0$ eV; (b) $U_{\text{eff}} = 2.0$ eV; and (c) $U_{\text{eff}} = 3.0$ eV. The upper and lower panels show the spin-up and spin-down channels, respectively.

larger than our previous work on $\text{Y}_2\text{Ti}_2\text{O}_7$ [10], as a result of different pseudopotential of Y employed.

3.4. Comparison of the Electronic Properties of $\text{Dy}_2\text{Ti}_2\text{O}_7$, $\text{Ho}_2\text{Ti}_2\text{O}_7$, and $\text{Y}_2\text{Ti}_2\text{O}_7$. The following discussions are based on the results obtained by $U_{\text{eff}} = 3.5$ eV for Dy, $U_{\text{eff}} = 3.4$ eV for Ho, and $U_{\text{eff}} = 0.0$ eV for Y. Comparison of the partial DOS distribution of these three compositions is presented in Figure 7. It is noted that the $\text{Dy}_2\text{Ti}_2\text{O}_7$ and $\text{Ho}_2\text{Ti}_2\text{O}_7$ have similar DOS results; in contrast, $\text{Y}_2\text{Ti}_2\text{O}_7$ shows a very different character. This is probably due to the fact that 4f electrons play an important role in $\text{Dy}_2\text{Ti}_2\text{O}_7$ and $\text{Ho}_2\text{Ti}_2\text{O}_7$. The electronic structures of a series of titanate oxides $\text{A}_2\text{Ti}_2\text{O}_7$ (A = Sm-Er, Yb, and Lu) have been studied by Nemoshkaleiko et al. [30] using X-ray photoelectron, emission spectroscopy, as well as the first-principles band structure calculations, where the lanthanide 4f states are assumed not to be hybridized with the other states. The calculations in the present work show that A-site 4f electrons do take part in the chemical bonding. For $\text{Dy}_2\text{Ti}_2\text{O}_7$ and $\text{Ho}_2\text{Ti}_2\text{O}_7$, the most striking features are the hybridization

of Dy 4f and Ho 4f orbitals with O 2p orbitals, as shown in Figure 7. Especially, a strong hybridization occurs for $\text{Dy}_2\text{Ti}_2\text{O}_7$ in its upper valence region. The 4f electrons also contribute greatly to the lower conduction bands of $\text{Dy}_2\text{Ti}_2\text{O}_7$ and $\text{Ho}_2\text{Ti}_2\text{O}_7$. Unlike $\text{Dy}_2\text{Ti}_2\text{O}_7$ and $\text{Ho}_2\text{Ti}_2\text{O}_7$, $\langle\text{Ti}-\text{O}\rangle$ interaction is more significant in $\text{Y}_2\text{Ti}_2\text{O}_7$, since its valence and conduction bands are mainly contributed by O 2p states hybridized with Ti 3d states and Ti 3d orbitals hybridized with O 2p orbitals, respectively.

Under irradiation, $\text{Y}_2\text{Ti}_2\text{O}_7$ is the most radiation resistant and $\text{Dy}_2\text{Ti}_2\text{O}_7$ is the least [7]. Since the pyrochlore compositions that are more easily disordered to the defect fluorite structure are more “resistant” to ion-beam-induced amorphization [18], $\text{Dy}_2\text{Ti}_2\text{O}_7$ is the least probable to transform into defect-fluorite structure and $\text{Y}_2\text{Ti}_2\text{O}_7$ is the most. This means that of the three compositions investigated, $\text{Dy}_2\text{Ti}_2\text{O}_7$ is the most stable thermodynamically and $\text{Y}_2\text{Ti}_2\text{O}_7$ is the least. The cation radius ratio criteria, as proposed by Sickafus et al. [18], clearly cannot be used to explain the different responses of these compositions to radiation. The radiation tolerance of nonmetallic solids has been correlated with the

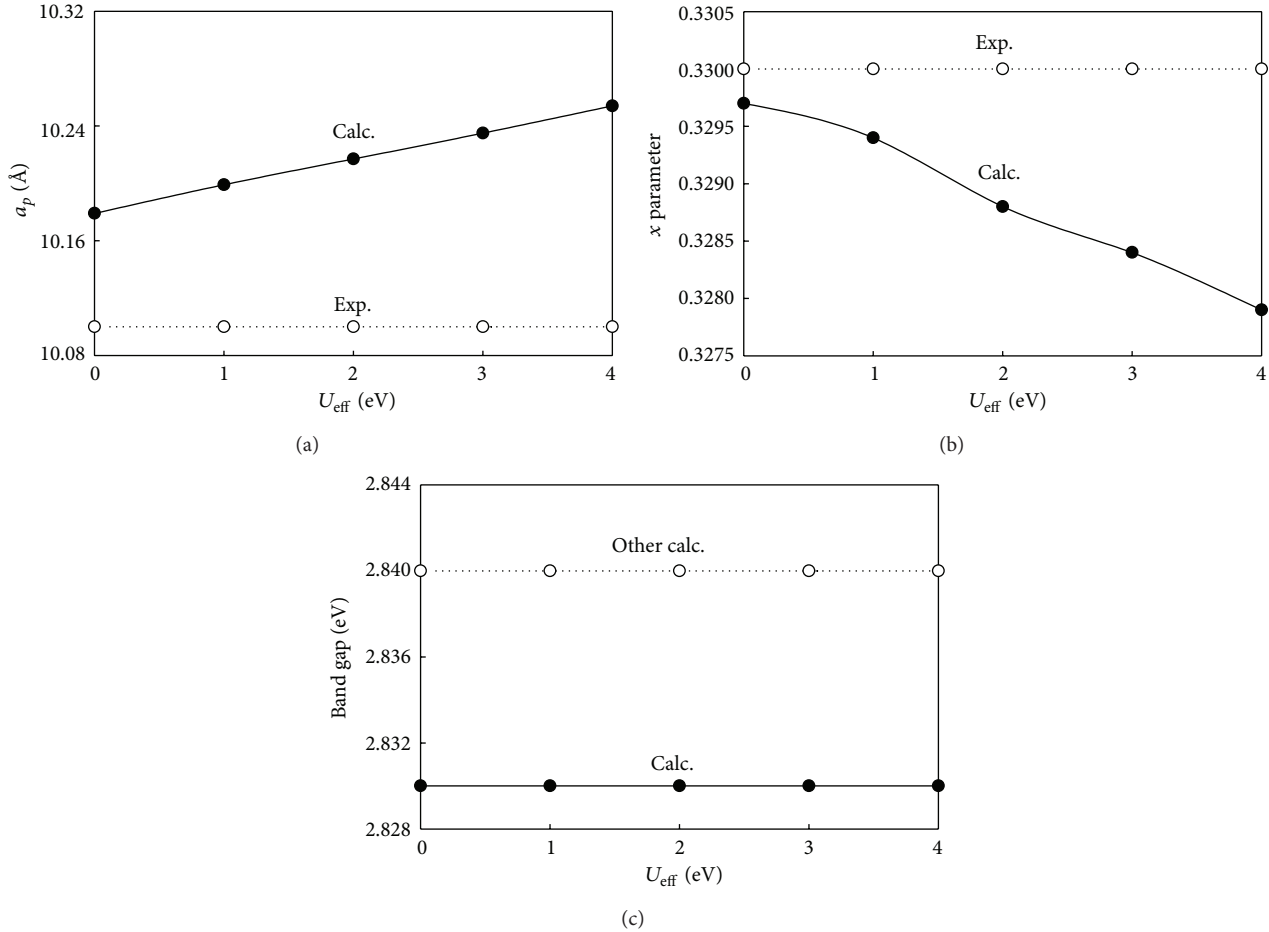


FIGURE 5: Dependence of the lattice parameter a_p (a), x (b), and band gap (c) of the $Y_2Ti_2O_7$ on U_{eff} .

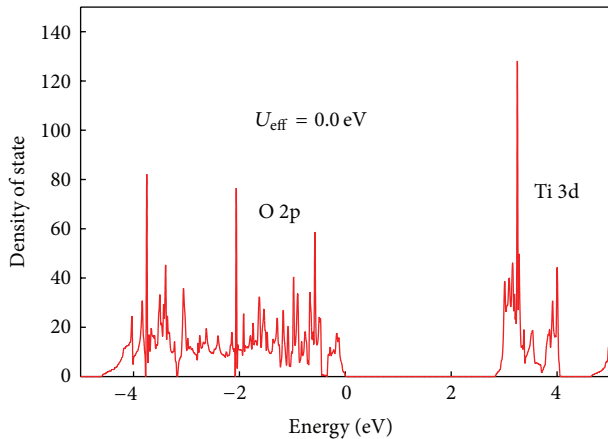


FIGURE 6: Total DOS distribution for $Y_2Ti_2O_7$ at $U_{\text{eff}} = 0.0$ eV.

nature of the chemical bond in earlier work [35–38]. They demonstrated that the more covalently bonded materials are more readily amorphized at lower temperatures under heavy ion irradiation. For pyrochlores, the less covalently

bonded compositions are more easily disordered to defect-fluorite structures [7], which are highly radiation resistant and remain crystalline at extreme radiation dose. In the present work, the strong interaction between Dy and Ho 4f electrons and O 2p orbitals may increase the covalency of $\langle \text{Dy-O} \rangle$ and $\langle \text{Ho-O} \rangle$ bonds and decrease the irradiation resistance of $Dy_2Ti_2O_7$ and $Ho_2Ti_2O_7$.

4. Conclusions

The electronic structures of $A_2Ti_2O_7$ ($A = \text{Dy}, \text{Ho}, \text{and Y}$) have been investigated using GGA + U method. The effects of effective U values on the structural and electronic properties of pyrochlores have been studied. It is shown that for strongly correlated systems such as $Dy_2Ti_2O_7$ and $Ho_2Ti_2O_7$, it is necessary to correct the intraband Coulomb interaction by the Hubbard U parameter. We suggest that the electronic structure can be reasonably described with U_{eff} of 3 ~ 4 eV for $Dy_2Ti_2O_7$ and $Ho_2Ti_2O_7$.

$Dy_2Ti_2O_7$ and $Ho_2Ti_2O_7$ have similar DOS distribution; in contrast, $Y_2Ti_2O_7$ shows a very different character. The DOS distributions of $Dy_2Ti_2O_7$ and $Ho_2Ti_2O_7$ show that A-site 4f electrons hybridize significantly with O 2p orbitals in the valence region. Since $Dy_2Ti_2O_7$ and $Ho_2Ti_2O_7$ are

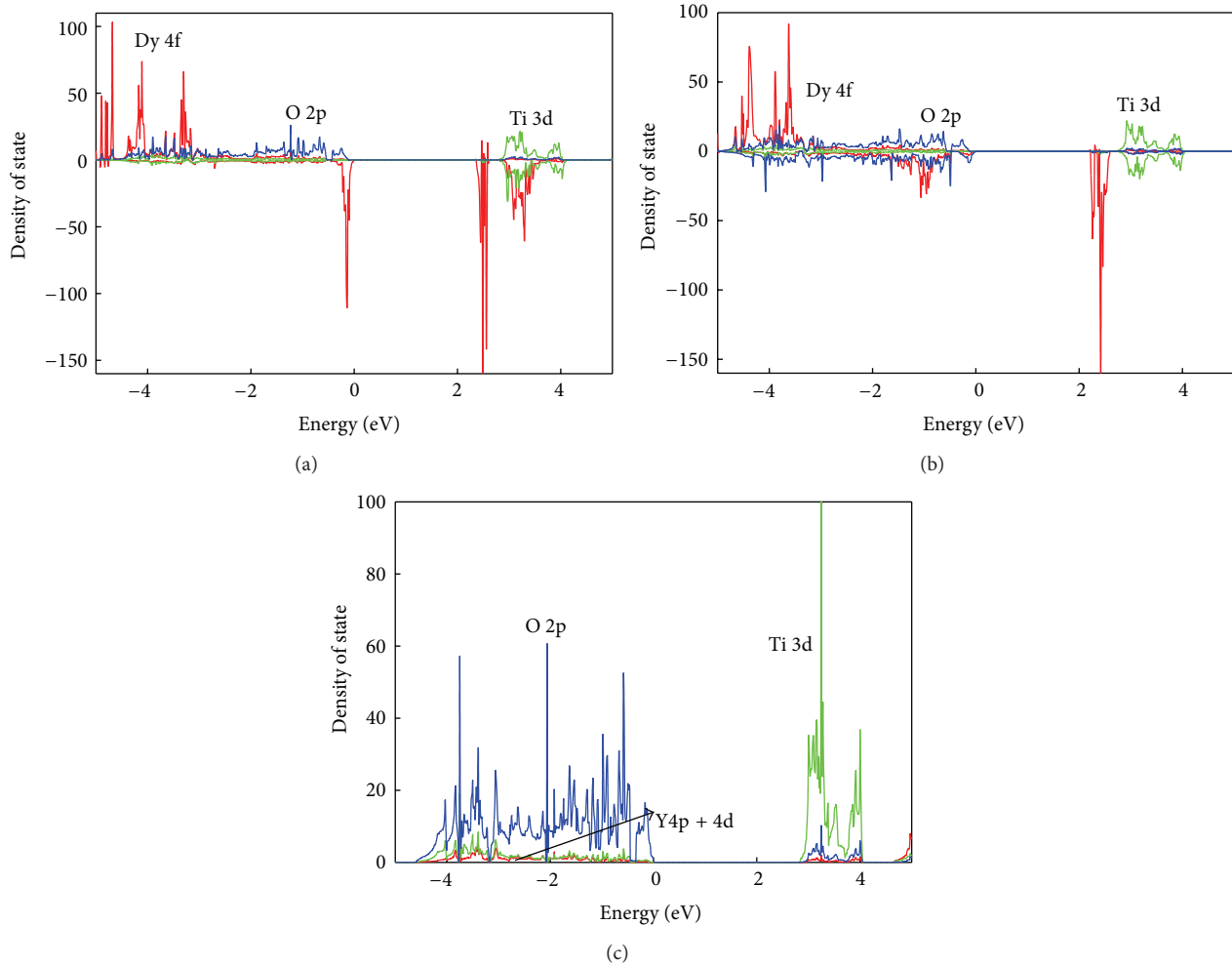


FIGURE 7: Partial DOS distributions of (a) $\text{Dy}_2\text{Ti}_2\text{O}_7$; (b) $\text{Ho}_2\text{Ti}_2\text{O}_7$; and (c) $\text{Y}_2\text{Ti}_2\text{O}_7$.

less radiation resistant than $\text{Y}_2\text{Ti}_2\text{O}_7$, it is suggested that the strong interaction between Dy and Ho 4f electrons and O 2p electrons may increase the covalency of $\langle\text{Dy}-\text{O}\rangle$ and $\langle\text{Ho}-\text{O}\rangle$ bonds and decrease the irradiation resistance of $\text{Dy}_2\text{Ti}_2\text{O}_7$ and $\text{Ho}_2\text{Ti}_2\text{O}_7$.

Acknowledgments

This work was supported by the National Natural Science Foundation of China (Grant no. 11004023) and by the Project Sponsored by the Scientific Research Foundation for the Returned Overseas Chinese Scholars, State Education Ministry.

References

- [1] B. J. Wuensch, K. W. Eberman, C. Heremans et al., "Connection between oxygen-ion conductivity of pyrochlore fuel-cell materials and structural change with composition and temperature," *Solid State Ionics*, vol. 129, no. 1, pp. 111–133, 2000.
- [2] R. C. Ewing, "Materials science: displaced by radiation," *Nature*, vol. 445, no. 7124, pp. 161–162, 2007.
- [3] W. J. Weber and R. C. Ewing, "Plutonium immobilization and radiation effects," *Science*, vol. 289, no. 5487, pp. 2051–2052, 2000.
- [4] R. C. Ewing, W. J. Weber, and J. Lian, "Nuclear waste disposal—pyrochlore ($\text{A}_2\text{B}_2\text{O}_7$): nuclear waste form for the immobilization of plutonium and "minor" actinides," *Journal of Applied Physics*, vol. 95, no. 11 I, pp. 5949–5971, 2004.
- [5] G. R. Lumpkin, K. P. Hart, P. J. McGlenn, T. E. Payne, R. Gier, and C. T. Williams, "Retention of actinides in natural pyrochlores and zirconolites," *Radiochimica Acta*, vol. 66–67, pp. 469–474, 1994.
- [6] A. Meldrum, C. W. White, V. Keppens, and L. A. Boatner, "Irradiation-induced amorphization of $\text{Cd}_2\text{Nb}_2\text{O}_7$ pyrochlore," *Physical Review B*, vol. 63, no. 10, Article ID 104109, pp. 1041091–10410911, 2001.
- [7] J. Lian, J. Chen, L. M. Wang et al., "Radiation-induced amorphization of rare-earth titanate pyrochlores," *Physical Review B*, vol. 68, no. 13, Article ID 134107, pp. 1341071–1341079, 2003.
- [8] J. Chen, J. Lian, L. M. Wang, R. C. Ewing, R. G. Wang, and W. Pan, "X-ray photoelectron spectroscopy study of disordering in $\text{Gd}_2(\text{Ti}_{1-x}\text{Zr}_x)_2\text{O}_7$ pyrochlores," *Physical Review Letters*, vol. 88, Article ID 105901, 4 pages, 2002.

- [9] H. Y. Xiao, X. T. Zu, F. Gao, and W. J. Weber, "First-principles study of energetic and electronic properties of $A_2Ti_2O_7$ ($A=Sm, Gd, Er$) pyrochlore," *Journal of Applied Physics*, vol. 104, Article ID 073503, 6 pages, 2008.
- [10] Z. L. Zhang, H. Y. Xiao, X. T. Zu, F. Gao, and W. J. Weber, "First-principles calculation of structural and energetic properties for $A_2Ti_2O_7$ ($A=Lu, Er, Y, Gd, Sm, Nd, La$)," *Journal of Materials Research*, vol. 24, no. 4, pp. 1335–1341, 2009.
- [11] H. Y. Xiao, L. M. Wang, X. T. Zu, J. Lian, and R. C. Ewing, "Theoretical investigation of structural, energetic and electronic properties of titanate pyrochlores," *Journal of Physics*, vol. 19, Article ID 346203, 2007.
- [12] H. Y. Xiao, F. Gao, and W. J. Weber, "Ab initio investigation of phase stability of $Y_2Ti_2O_7$ and $Y_2Zr_2O_7$ under high pressure-Physical Review B," vol. 80, Article ID 212102, 4 pages, 2009.
- [13] Z. J. Chen, H. Y. Xiao, X. T. Zu et al., "Structural and bonding properties of stannate pyrochlores: a density functional theory investigation," *Computational Materials Science*, vol. 42, no. 4, pp. 653–658, 2008.
- [14] N. Li, H. Y. Xiao, X. T. Zu et al., "First-principles study of electronic properties of $La_2Hf_2O_7$ and $Gd_2Hf_2O_7$," *Journal of Applied Physics*, vol. 102, Article ID 063704, 2007.
- [15] H. Y. Xiao, F. X. Zhang, F. Gao, M. Lang, R. C. Ewing, and W. J. Weber, "Zirconate pyrochlores under high pressure," *Physical Chemistry Chemical Physics*, vol. 12, no. 39, pp. 12472–12477, 2010.
- [16] H. Y. Xiao and W. J. Weber, "Pressure induced structural transformation in $Gd_2Ti_2O_7$ and $Gd_2Zr_2O_7$," *Journal of Physics*, vol. 23, Article ID 35501, 2011.
- [17] J. M. Pruneda and E. Artacho, "First-principles study of structural, elastic, and bonding properties of pyrochlores," *Physical Review B*, vol. 72, Article ID 085107, 8 pages, 2005.
- [18] K. E. Sickafus, L. Minervini, R. W. Grimes et al., "Radiation tolerance of complex oxides," *Science*, vol. 289, no. 5480, pp. 748–751, 2000.
- [19] R. Terki, H. Feraoun, G. Bertrand, and H. Aourag, "Full potential linearized augmented plane wave investigations of structural and electronic properties of pyrochlore systems," *Journal of Applied Physics*, vol. 96, no. 11, pp. 6482–6487, 2004.
- [20] A. Chartier, C. Meis, W. J. Weber, and L. R. Corrales, "Theoretical study of disorder in Ti-substituted $La_2Zr_2O_7$," *Physical Review B*, vol. 65, Article ID 134116, 11 pages, 2002.
- [21] R. E. Williford, W. J. Weber, R. Devanathan, and J. D. Gale, "Effects of cation disorder on oxygen vacancy migration in $Gd_2Ti_2O_7$," *Journal of Electroceramics*, vol. 3, no. 4, pp. 409–424, 1999.
- [22] X. J. Wang, H. Y. Xiao, X. T. Zu, Y. Zhang, and W. J. Weber, "Ab initio molecular dynamics simulations of ion–solid interactions in $Gd_2Zr_2O_7$ and $Gd_2Ti_2O_7$," *Journal of Materials Chemistry C*, vol. 1, p. 1665, 2013.
- [23] W. R. Panero, L. Stixrude, and R. C. Ewing, "First-principles calculation of defect-formation energies in the $Y_2(Ti,Sn,Zr)_2O_7$ pyrochlore," *Physical Review B*, vol. 70, Article ID 054110, 11 pages, 2004.
- [24] G. Kresse and D. Joubert, "From ultrasoft pseudopotentials to the projector augmented-wave method," *Physical Review B*, vol. 59, no. 3, pp. 1758–1775, 1999.
- [25] J. P. Perdew, J. A. Chevary, S. H. Vosko et al., "Atoms, molecules, solids, and surfaces: applications of the generalized gradient approximation for exchange and correlation," *Physical Review B*, vol. 46, no. 11, pp. 6671–6687, 1992.
- [26] J. A. White and D. M. Bird, "Implementation of gradient-corrected exchange-correlation potentials in Car-Parrinello total-energy calculations," *Physical Review B*, vol. 50, no. 7, pp. 4954–4957, 1994.
- [27] M. J. Harris, S. T. Bramwell, D. F. McMorrow, T. Zeiske, and K. W. Godfrey, "Geometrical frustration in the ferromagnetic pyrochlore $Ho_2Ti_2O_7$," *Physical Review Letters*, vol. 79, no. 13, pp. 2554–2557, 1997.
- [28] A. P. Ramirez, A. Hayashi, R. J. Cava, R. Siddharthan, and B. S. Shastry, "Zero-point entropy in 'spin ice'," *Nature*, vol. 399, no. 6734, pp. 333–335, 1999.
- [29] S. L. Dudarev, G. A. Botton, S. Y. Savrasov, C. J. Humphreys, and A. P. Sutton, "Electron-energy-loss spectra and the structural stability of nickel oxide: an LSDA+U study," *Physical Review B*, vol. 57, no. 3, pp. 1505–1509, 1998.
- [30] V. V. Nemoshkalenko, S. V. Borisenko, V. N. Uvarov et al., "Electronic structure of the $R_2Ti_2O_7$ ($R=Sm-Er, Yb, Lu$) oxides," *Physical Review B*, vol. 63, no. 7, Article ID 075106, pp. 0751061–0751068, 2001.
- [31] A. K. Pandit, T. H. Ansari, R. A. Singh, and B. M. Wanklyn, "Electrical conduction in $Dy_2Ti_2O_7$ single crystal," *Materials Letters*, vol. 11, no. 1-2, pp. 52–58, 1991.
- [32] V. I. Anisimov, F. Aryasetiawan, and A. I. Lichtenstein, "First-principles calculations of the electronic structure and spectra of strongly correlated systems: the LDA + U method," *Journal of Physics Condensed Matter*, vol. 9, no. 4, pp. 767–808, 1997.
- [33] S. T. Bramwell and M. J. P. Gingras, "Spin ice state in frustrated magnetic pyrochlore materials," *Science*, vol. 294, no. 5546, pp. 1495–1501, 2001.
- [34] Y. Jiang, J. R. Smith, and G. Robert Odette, "Prediction of structural, electronic and elastic properties of $Y_2Ti_2O_7$ and Y_2TiO_5 ," *Acta Materialia*, vol. 58, no. 5, pp. 1536–1543, 2010.
- [35] H. M. Naguib and R. Kelly, "Criteria for bombardment-induced structural changes in non-metallic solids," *Radiation Effects*, vol. 25, no. 1, pp. 1–12, 1975.
- [36] K. Trachenko, "Understanding resistance to amorphization by radiation damage," *Journal of Physics Condensed Matter*, vol. 16, no. 49, pp. R1491–R1515, 2004.
- [37] K. Trachenko, J. M. Pruneda, E. Artacho, and M. T. Dove, "How the nature of the chemical bond governs resistance to amorphization by radiation damage," *Physical Review B*, vol. 71, no. 18, Article ID 184104, 2005.
- [38] R. C. Ewing, W. J. Weber, and J. Lian, "Nuclear waste disposal-pyrochlore ($A_2B_2O_7$): nuclear waste form for the immobilization of plutonium and "minor" actinides," *Journal of Applied Physics*, vol. 95, no. 11 I, pp. 5949–5971, 2004.

Research Article

Catalytic Mechanism of Pd Adsorption on S-Terminated GaAs(001)-(2 × 6) Surface

Deng-feng Li, Zhi-cheng Guo, Bo-Lin Li, and Ming Luo

Department of Mathematics and Physics, Chongqing University of Posts and Telecommunications,
Chongqing 400065, China

Correspondence should be addressed to Deng-feng Li; phyldf@gmail.com

Received 29 May 2013; Accepted 24 July 2013

Academic Editor: Haiyan Xiao

Copyright © 2013 Deng-feng Li et al. This is an open access article distributed under the Creative Commons Attribution License, which permits unrestricted use, distribution, and reproduction in any medium, provided the original work is properly cited.

Structural and electronic properties of Pd adsorption on clean and S-terminated GaAs(001)-(2 × 6) surfaces are studied using first-principle simulations. Our calculations show that the Pd atom prefers to occupy the HH3 site. The Pd atom is lower than the S atom with 0.15 Å. The density of states analysis confirms that S-Ga bond plays an important role in Heck reaction. We also find that the Pd catalysis activity for Pd adsorption on clean GaAs(001)-(2 × 6) surface is weak while it is enhanced when the Pd atom is adsorbed on the S-terminated GaAs(001)-(2 × 6) surface, which is in good agreement with the experiments.

1. Introduction

Transition metals such as palladium (Pd) and platinum (Pt) are very important catalysts in the field of synthetic chemistry since they have favorable catalysis properties in Heck reaction [1–3]. Heck reaction plays an important role in drug discovery and pharmaceutical industries. However, the homogeneous Pd catalysis has some disadvantages, such as low reusability, difficulty of separating the catalyst from the products or solvents after reaction.

Recently, heterogeneous catalyst has been extensively investigated in order to reduce the waste of noble metal and develop the high yield of Heck reaction. For Pd adsorption on the sulfur-terminated GaAs(001) surface, experimental results show that the Pd catalyst is reusable [4–8]. Arisawa et al. prepare it with Pd(PPh₃)₄ [5]. They find that Pd is adsorbed on the S-terminated GaAs surface by X-ray photoelectron spectroscopy (XPS) and Pd can be reused at least 3 times. Takamiya et al. find that Ga-S bond fixes Pd on S-terminated GaAs(001)-(2 × 6) surface [6, 7], which plays an important role in Heck reaction. It effectively enhances the activity of the Heck reaction more than homogeneous Pd catalyst and could be recycled at least 10 times. In their further study [8],

using a new Pd source of Pd(OAc)₂ and another technique of heated washing, they obtain a higher catalysis activity and stability for Heck reaction than the sophisticated method of deposition organometallic Pd(PPh₃)₄ on S-terminated GaAs(001)-(2 × 6) surface. Recently, Konishi et al. report that S-GaAs(2 × 6) surface structure is preserved after deposition Pd(CH₃COO)₂ on its surface using reflection high-energy electron diffraction (RHEED) and scanning tunneling microscopy (STM) [9]. However, the detailed structure and micromechanism are unknown. Earlier theoretical study is focused on the system of Pd adsorption on S-terminated GaAs(001)-(2 × 1) surface [10], which is different from the experiments [7, 9, 11].

In this paper, in order to explain the intrinsic mechanism of Pd catalysis, we investigate the surface structure and electronic property of Pd adsorption on S-GaAs(2 × 6) surface, based on the density functional theory (DFT). We confirm that the S-Ga band is essential for catalytic reaction.

2. Calculation Method

All the calculations were performed using Vienna ab initio simulation package (VASP) with cutoff energy 500 eV.

The ion-electron interaction was described by the projector augmented wave method (PAW). Local density approximation (LDA) approach was used to deal with the energy of exchange correlation. The d electrons are included for Ga atom. Integration over an irreducible Brillouin zone was carried out using the Monkhorst-Pack grid of $5 \times 5 \times 1$. The unit supercell of S adsorption on GaAs(001)- (2×6) surface consists of 5 atomic layers and plus a vacuum layer equivalent to 5 atomic layers in thickness. The position of bottom layer As atoms was fixed. Hydrogenlike pseudoatoms with 0.75 charges were used to saturate the surface As dangling bonds at the bottom of slab. The optimized lattice constant was 5.610 Å, consistent with the experimental value of 5.653 Å [12].

3. Results and Discussions

3.1. Structural Parameters. To understand the important role of S atom in Pd catalyst on S-terminated GaAs(001)- (2×6) surface, we have investigated the atomic and electronic structures of Pd adsorption on pure GaAs(001)- (2×6) and S-terminated GaAs(001)- (2×6) surfaces. Nine possible adsorption sites, such as HH, HH2, HH3, B1, B2, B3, H1, H2, and H3, are considered, as shown in Figure 1. We obtain the most stable structure by the calculated adsorption energy. The adsorption energy is defined as $E_1 = E_{\text{Pd/GaAs}(001)} - E_{\text{GaAs}(001)} - E_{\text{Pd}}$ and $E_2 = E_{\text{Pd/S-GaAs}(001)} - E_{\text{S-GaAs}(001)} - E_{\text{Pd}}$ for Pd deposition on GaAs(001) and S-terminated GaAs(001) surfaces, respectively. $E_{\text{Pd/GaAs}(001)}$, $E_{\text{Pd/S-GaAs}(001)}$, $E_{\text{GaAs}(001)}$, $E_{\text{S-GaAs}(001)}$, and E_{Pd} denote the total energies of adsorbed system, the clean GaAs(001) surface, the S-terminated GaAs(001) and a free of Pd atom, respectively. The results show that Pd prefers to occupy the HH3 site both on clean and S-terminated GaAs(001)- (2×6) surfaces.

The detailed structures of Pd adsorption on GaAs(001)- (2×6) and S-terminated GaAs(001)- (2×6) surfaces are presented. We find that the position of Pd is lower than the surface As or S atom for both model cases, which is similar to the result of Pd adsorption on S-terminated GaAs(001)- (2×1) surface [10]. The height between Pd and underlying S layer is 0.15 Å and Pd-S bond length is 2.53 Å on S-terminated GaAs surface. Pd-As bond length is calculated to be 2.51 Å on clean GaAs surface, which is similar to the Au-As bond length of 2.50 Å for Au adsorption on GaAs(001) surface [13]. For Pd adsorption on S-terminated GaAs(001)- (2×6) surface, the S-S dimer remains on the substrate and the bond length is calculated to be 3.568 Å, which is consistent with the experimental findings that (2×6) reconstruction is preserved when Pd immobilized on the S-terminated GaAs from the RHEED and STM investigations [9].

3.2. Electronic Properties. Figure 2 shows the total density of states (TDOS) and local density of states (LDOS) of Pd adsorption on clean GaAs(001)- (2×6) surface at HH3 position. The calculated band gap is only 0.3 eV, which is remarkably smaller than that for clean GaAs surface (1.43 eV). The significant reduction of band gap induced by the adsorption of metal is also found in other systems, such

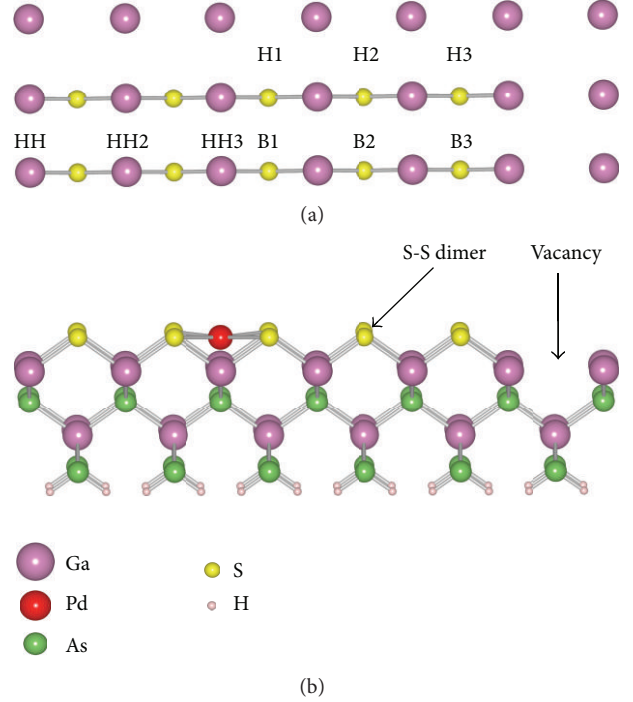


FIGURE 1: Top (a) and side views (b) structure of Pd adsorption on S-terminated GaAs(001)- (2×6) surface.

as Pd adsorption on TiO₂ and Au adsorption on MgO [14–16]. It is derived from the fact of charge polarization by metal adsorption and an increase of the potential in the adsorption layer. For Pd adsorption on the clean GaAs(001)- (2×6) surface, the catalyst activity of Pd is weak due to a few electronic states at the Fermi energy.

In Figure 3, the TDOS and LDOS of Pd adsorption on S-terminated GaAs(001)- (2×6) surface at HH3 site are presented. Compared with the TDOS of S-terminated GaAs(001)- (2×6) surface, we find that the Pd adsorption makes the DOS shift to lower energy, and the Fermi level exists above the conduction band, which is attributed to the strong interaction between Pd adatom and substrate. In addition, the band gap for Pd adsorption on S-terminated GaAs(001) surface is almost disappeared. It is because that the metal induced gap states (MIGS) are found in the energy gap, which is composed of Ga 4p and S 3p states. MIGS can lead to increasing the activity of chemical reaction due to the increase of the probability of getting electrons. It is consistent with the experimental result of important role for S-Ga bond in Heck reaction [7, 9]. On the other hand, comparing the DOS of Pd adsorption on clean GaAs(001) surface, we can see that the electronic state at the Fermi level is remarkably increased for Pd adsorption on S-terminated GaAs(001) surface. It indicates that the Pd catalysis activity is enhanced. Meanwhile, DOS at the Fermi level is mainly arisen from the contribution of Pd 4d and S 3p states, and the hybridization between Pd 4d and S 3p states both in valence band and conduction band is also found. Therefore, a strong Pd-S bond is formed on the surface.

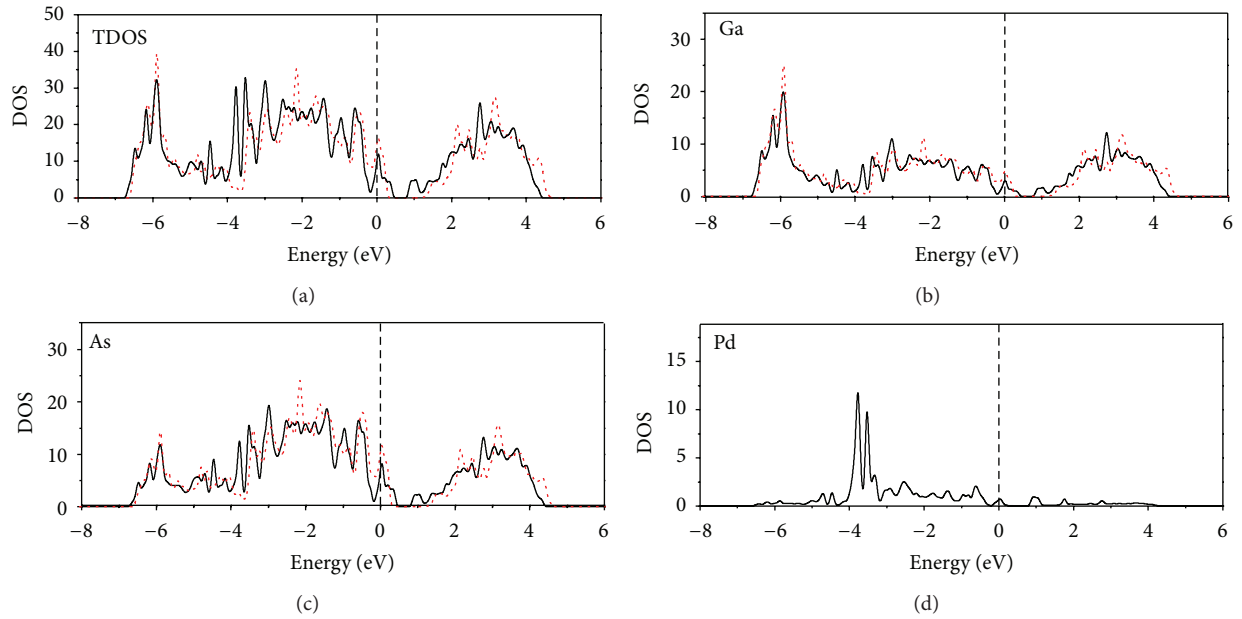


FIGURE 2: The total and local density of states (DOS) of Pd adsorption on clean GaAs(001)-(2 × 6) surface at HH3 site. The dashed line denotes DOS for the clean GaAs(001)-(2 × 6) surface without Pd adsorption. The dashed vertical line at zero represents the Fermi level.

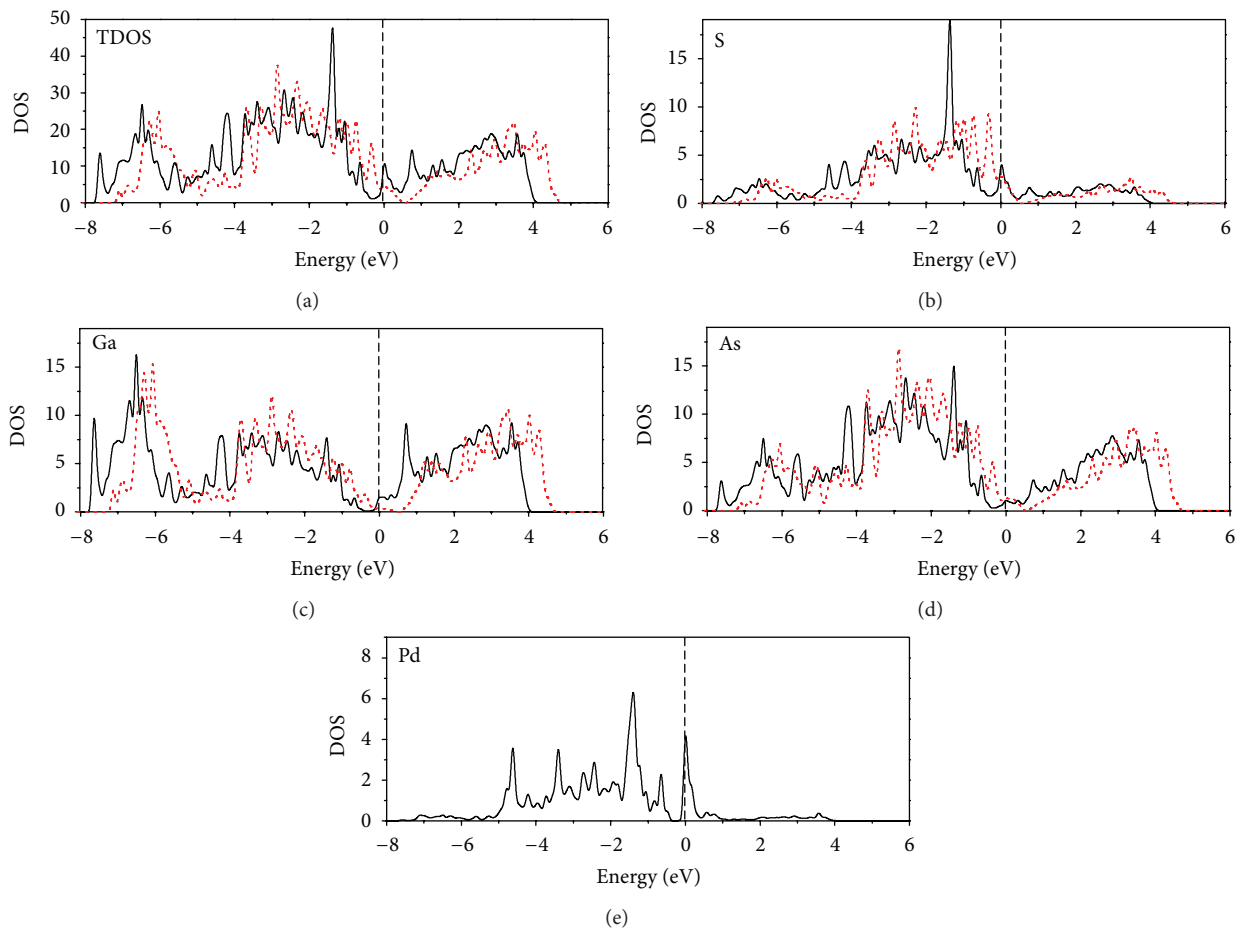


FIGURE 3: The total and local DOS of Pd adsorption on S-terminated GaAs(001)-(2 × 6) surface at HH3 site. The dashed line denotes DOS of S-terminated GaAs(001)-(2 × 6) surface without Pd adsorption.

4. Conclusion

We have investigated the structural and electronic properties of Pd adsorption on clean and S-terminated GaAs(001)-(2 × 6) surfaces using first-principle simulations. The calculated adsorption energy shows that Pd atom prefers to occupy the HH3 site. The detailed structure is presented and the Pd atom is lower than the S atom with 0.15 Å. The density of states demonstrates that S–Ga bond plays an important role in Heck reaction. We also find that the Pd catalysis activity for Pd adsorption on clean GaAs(001)-(2 × 6) surface is weak while it is enhanced when Pd atom is adsorbed on the S-terminated GaAs(001)-(2 × 6) surface, which is in good agreement with the experiments.

Acknowledgment

The authors acknowledge financial support from the Key Program of the Natural Science Foundation of Chongqing (cstc2012jjB50010).

References

- [1] M. Smiljanic, I. Srejic, B. Grgur, Z. Rakocevic, and S. Strbac, "Catalysis of hydrogen evolution on Au(111) modified by spontaneously deposited Pd nanoislands," *Electrocatal*, vol. 3, no. 3-4, pp. 369–375, 2012.
- [2] S. E. Bae, D. Gokcen, P. Liu, P. Mohammadi, and S. R. Brankovic, "Size effects in monolayer catalysis-model study: Pt submonolayers on Au(111)," *Electrocatal*, vol. 3, no. 3-4, pp. 203–210, 2012.
- [3] H. Y. Xu, Y. N. Guo, Z. M. Liao et al., "Catalyst size dependent growth of Pd-catalyzed one-dimensional InAs nanostructures," *Applied Physics Letters*, vol. 103, no. 20, Article ID 203108, 2013.
- [4] N. Nishiwaki, T. Konishi, S. Hirao, Y. Yamashita, H. Yoshikawa, and M. Shimoda, "Hydroxylated surface of GaAs as a scaffold for a heterogeneous Pd catalyst," *Physical Chemistry Chemical Physics*, vol. 14, no. 4, pp. 1424–1430, 2012.
- [5] M. Arisawa, S. Tsukamoto, M. Shimoda, M. Pristovsek, and A. Nishida, "Novel organopalladium material formed on a sulfur-terminated GaAs(001) surface," *Japanese Journal of Applied Physics, Part 2*, vol. 41, no. 11, pp. L1197–L1199, 2002.
- [6] I. Takamiya, S. Tsukamoto, M. Shimoda et al., "Novel palladium catalyst supported on GaAs(001) passivated by ammonium sulfide," *Chemistry Letters*, vol. 33, no. 9, pp. 1208–1209, 2004.
- [7] I. Takamiya, S. Tsukamoto, M. Shimoda, M. Arisawa, A. Nishida, and Y. Arakawa, "Highly reactive organopalladium catalyst formed on sulfur-terminated GaAs(001)-(2 × 6) surface," *Japanese Journal of Applied Physics, Part 2*, vol. 45, no. 17–19, pp. L475–L477, 2006.
- [8] M. Arisawa, M. Hamada, I. Takamiya et al., "Development of a method for preparing a highly reactive and stable, recyclable and environmentally benign organopalladium catalyst supported on sulfur-terminated gallium arsenide(001): a three-component catalyst, Pd-S-GaAs(001), and its properties," *Advanced Synthesis and Catalysis*, vol. 348, no. 9, pp. 1063–1070, 2006.
- [9] T. Konishi, T. Toujyou, T. Ishikawa, G. R. Bell, and S. Tsukamoto, "Organopalladium catalyst on S-terminated GaAs (001)-(2×6) surface," *Journal of Vacuum Science and Technology B*, vol. 27, no. 5, pp. 2206–2208, 2009.
- [10] A. Ishii, H. Asano, M. Yokoyama, S. Tsukamoto, S. Shuto, and M. Arisawa, "Structure determination of Pd-catalyst supported on S-terminated GaAs(001) using DFT calculation," *Physica Status Solidi (C) Current Topics in Solid State Physics*, vol. 7, no. 2, pp. 359–361, 2010.
- [11] S. Tsukamoto, T. Ohno, and N. Koguchi, "Scanning tunneling spectroscopy and first-principles investigation on GaAs(001)(2×6)-S surface formed by molecular beam epitaxy," *Journal of Crystal Growth*, vol. 175-176, no. 2, pp. 1303–1308, 1997.
- [12] V. Milman, B. Winkler, J. A. White et al., "Electronic structure, properties, and phase stability of inorganic crystals: a pseudopotential Plane-Wave Study," *International Journal of Quantum Chemistry*, vol. 77, no. 5, pp. 895–910, 2000.
- [13] S. Yang, L. Zhang, H. Chen, E. Wang, and Z. Zhang, "Generic guiding principle for the prediction of metal-induced reconstructions of compound semiconductor surfaces," *Physical Review B*, vol. 78, no. 7, Article ID 075305, 2008.
- [14] Z. Yang, R. Wu, and D. W. Goodman, "Structural and electronic properties of Au on TiO₂(110)," *Physical Review B*, vol. 61, no. 20, pp. 14066–14071, 2000.
- [15] J. F. Sanz and A. Márquez, "Adsorption of Pd atoms and dimers on the TiO₂ (110) surface: a first principles study," *Journal of Physical Chemistry C*, vol. 111, no. 10, pp. 3949–3955, 2007.
- [16] M. Amft and N. V. Skorodumova, "Catalytic activity of small MgO-supported Au clusters towards CO oxidation: a density functional study," *Physical Review B*, vol. 81, no. 19, Article ID 195443, 2010.

Research Article

Low-Resistivity p-Type Doping in Wurtzite ZnS Using Codoping Method

Deng-Feng Li, Min Luo, Bo-Lin Li, Cheng-Bing Wu, Bo Deng, and Hui-Ning Dong

Department of Mathematics and Physics, Chongqing University of Posts and Telecommunications, Chongqing 400065, China

Correspondence should be addressed to Deng-Feng Li; phyldf@gmail.com

Received 31 May 2013; Accepted 24 July 2013

Academic Editor: Haiyan Xiao

Copyright © 2013 Deng-Feng Li et al. This is an open access article distributed under the Creative Commons Attribution License, which permits unrestricted use, distribution, and reproduction in any medium, provided the original work is properly cited.

By using first principles calculations, we propose a codoping method of using acceptors and donors simultaneously to realize low-resistivity and high carrier concentration p-type ZnS with wurtzite structure. The ionization energy of single N_S can be lowered by introducing the $III_{Zn}-N_S$ ($III = Al, Ga, In$) passivation system. Codoping method in ZnS (2N, III) has lower formation energy comparing with single doping of N since III elements act as reactive codopants.

1. Introduction

Wide bandgap semiconductors, such as ZnX ($X = O, S, Se$), have attracted attention due to their potential application in short-wavelength light-emitting devices. Unfortunately, the doping unipolarity, that is, it can be doped either p-type or n-type, but not both, impedes the implementation of the materials [1]. Earlier researches show that ZnS and ZnO are difficult to be doped as p-type due to asymmetric doping limitation [1–3]. In order to obtain low-resistivity p-type ZnS, single doping and codoping methods are studied. Nakamura et al. fabricate Li-doped ZnS by a low-pressure metal organic chemical vapor deposition technique [2]. They find that it is p-type conductivity, and the acceptor ionization energy is about 196 meV, which is larger than the calculated results of 155 meV by Gai et al. [3]. Gai et al. calculated ionization energies for possible single doping method to obtain p-type ZnS [3]. The result shows that N-doped ZnS is promised to be p-type, but the ionization energy is calculated to be 144 meV, which is still deep acceptor level.

In recent years, codoping method was suggested to solve the unipolarity of semiconductor [1, 4, 5]. P-type doping in ZnO is realized by codoping with N acceptors and Ga donors in the ratio of $N:Ga = 2:1$ [6, 7]. For p-type ZnS, experimental researches realize it by codoping with N and Li dual acceptors, and the hole concentration is measured to be 10^{18} cm^{-3} [8]. Theoretical investigations show that the codoping method of acceptor-donor-acceptor is more efficient than

the single-doping method. They realize p-type ZnS by codoping with N acceptors and In or Al donors based on first principles calculations [9–11]. Codoping method makes the acceptor levels broaden and delocalize compared with the single doping of N. In addition, p-type ZnS nanocrystals can be obtained by codoping with N and Ga, In, or Al [12]. However, earlier researches about p-type ZnS with codoping method mainly focus on the density of state analysis. Quantifiable parameters, such as acceptor ionization energy and formation energy, are not presented. In addition, they have studied the zinc blende (ZB) ZnS. P-type ZnS with wurtzite (WZ) structure has not been investigated up to now. Therefore, the purpose of this study is to investigate p-type ZnS with WZ structure by codoping with N and Ga, Al, and In. Acceptor ionization energy, formation energy, and density of states are presented to analyze the effects of Ga, Al, and In codopant on p-type ZnS.

2. Calculation Method

We performed the calculations using the projector augmented wave method [13] within the generalization gradient approximation (GGA) [14], as implemented in the Vienna *ab initio* simulation (VASP) code [15]. $3d$ and $4s$ electrons of Zn are treated as valence electrons. The energy cutoff for the plane wave expansion sets with a 450 eV. For the Brillouin zone integration, we use Monkhorst-Pack special

k -points [16], equivalent to the $2 \times 2 \times 2$ mesh. Wurtzite supercells containing 96 atoms are used. For charged defect systems, a uniform background charge is added to maintain the global charge neutrality of the periodic system. All the geometries are allowed to relax until the Hellmann-Feynman force becomes less than 0.02 eV/\AA . The optimized lattice constants for ZnS is $a = b = 3.85 \text{ \AA}$, $c = 6.29 \text{ \AA}$, which are in good agreement with the experimental values $a = b = 3.81 \text{ \AA}$, $c = 6.23 \text{ \AA}$.

The ionization energy of an acceptor with respect to VBM is calculated as follows [1, 17]:

$$\begin{aligned} \varepsilon(0/-) = & \left[E(\alpha, -) - (E(\alpha, 0) + \varepsilon_D^k(0)) \right] \\ & + \left[\varepsilon_D^\Gamma(0) - \varepsilon_{\text{VBM}}^\Gamma(\text{ZnS}) \right], \end{aligned} \quad (1)$$

where ε_D^k and ε_D^Γ are the defect levels at the special k -points (averaged by weights) and at Γ -point, respectively; $E(\alpha, -)$ or $E(\alpha, 0)$ is the total energy of the supercell at charge state -1 or neutral for defect α ; $\varepsilon_{\text{VBM}}^\Gamma$ is the VBM energy of the host ZnS at Γ -point.

The formation energy of an isolated impurity α in charge state q is described as follows [1, 17]:

$$\Delta H_f(\alpha, q) = \Delta E(\alpha, q) + n_{\text{Zn}}\mu_{\text{Zn}} + n_{\text{S}}\mu_{\text{S}} + n_{\text{A}}\mu_{\text{A}} + qE_f, \quad (2)$$

where $\Delta E(\alpha, q) = E(\alpha, q) - E(\text{ZnS}) + n_{\text{Zn}}E(\text{Zn}) + n_{\text{S}}E(\text{S}) + n_{\text{A}}E(\text{A}) + q\varepsilon_{\text{VBM}}^\Gamma$. The n_i ($i = \text{Zn, S, and A}$) are the numbers of exchanged particles between the supercell, q is the defect charge state, μ_i is the chemical potential of constituent i referenced to elemental solid/gas with energy E_i . μ_{Zn} and μ_{S} in (2) are not independent but limited by the formation of stable ZnS compound, $\mu_{\text{Zn}} + \mu_{\text{S}} = \Delta H_f(\text{ZnS})$, where $\Delta H_f(\text{ZnS})$ is the formation enthalpy of solid ZnS.

3. Results and Discussion

We firstly determine the most stable structure of codoped ZnS with N and group III elements (Al, Ga, and In) based on minimizing the total energy. For ZnS (N, III), we discuss two possible configurations. One configuration is N_S -III $_{\text{Zn}}$ pair occupied the nearest-neighbor sites and the other is a pair separated certain distance away. The result shows that the formation of the first case is energetically favorable. When another N atom is doped in the ZnS (N, III), total energy calculations show that the N atom also prefers to locate at the nearest-neighbor site, as shown in Figure 1. For the stable ZnS (2N, III), the bond length of N-Al, N-Ga, and N-In is 1.9 \AA , 2.0 \AA , and 2.2 \AA , respectively, which is remarkably smaller than Zn-S bond length of pristine ZnS of 2.36 \AA .

The calculated acceptor ionization energy and formation energy of codoping with N and III elements in ZnS are presented in Table 1. The acceptor ionization energy denotes the provided hole in ZnS, and the formation energy controls the dopant solubility, which is important for p-type doping of semiconductor. When only N atom is doped in ZnS, the ionization energy is 103.9 meV , which is smaller than that of N doping in ZB ZnS (144 meV). This suggests that N doping generates a deep acceptor level above the valence band.

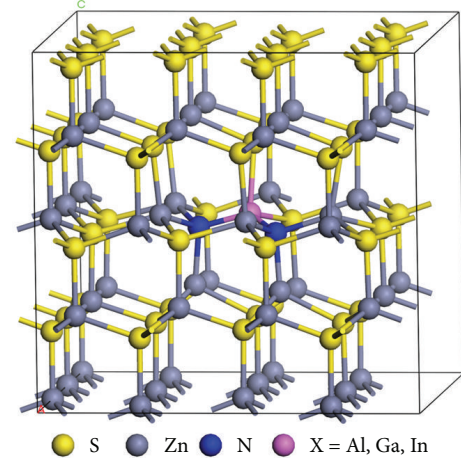


FIGURE 1: Schematic structure of codoping with N and X (Al, Ga, and In) in wurtzite ZnS.

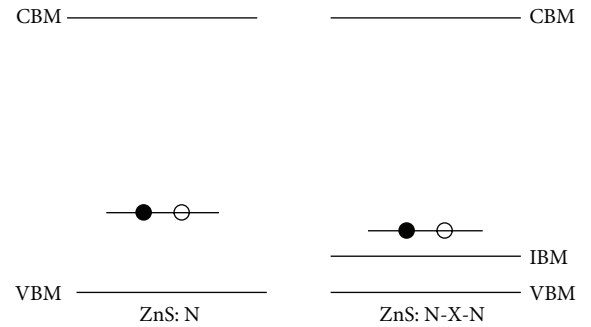


FIGURE 2: Schematic illustration of the energy level for single doping of N and codoping with N and X (Al, Ga, and In) in ZnS.

Fortunately, codoping with N and III elements in ZnS can remarkably reduce the ionization energy. Shallow acceptor level exists in ZnS, and the acceptor ionization energies of $\text{Al}_{\text{Zn}}-2\text{N}_\text{S}$ and $\text{Ga}_{\text{Zn}}-2\text{N}_\text{S}$ pairs are 40.1 meV and 37.5 meV , respectively. The lower ionization energy of codoping with N and III elements can be explained by Figure 2. ZnS (N, III) creates a fully unoccupied impurity band above the VBM. The N atom passivates the III elements to form the ZnS (N, III) passivated system. When excess N atoms are available, the impurity band is regarded as new VBM, and $\varepsilon_{\text{VBM}}^\Gamma(\text{ZnS})$ in (1) is replaced by the impurity band minimum (IBM). The acceptor transition occurs between the N energy level and the IBM rather than the original VBM. Thus, the ionization energy can be remarkably reduced.

The formation energies of 2N_S -III $_{\text{Zn}}$ complex and single doping of N for ZnS in neutral charge state and at $\mu_i = 0$ in (2) are also shown in Table 1. The low formation energy suggests this defect has high carrier concentration. Our calculations reveal that the formation energy of 2N_S -III $_{\text{Zn}}$ complex is smaller than that of single doping of N. This can be explained by the density of states (DOS) analysis. Figure 3 shows DOS of N-p state in ZnS (2N, Al) and ZnS (N). The DOS of the N atom in ZnS (2N, Al) is similar to that in ZnS (2N, Ga) and ZnS (2N, In), and we only present the representative result

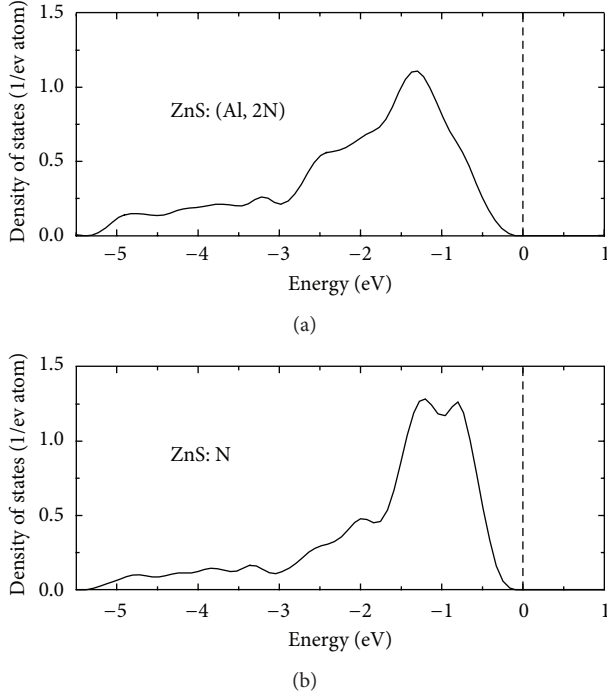


FIGURE 3: DOS of N-p states for (a) ZnS codoped with Al and 2N species and (b) ZnS doped with the N atom.

TABLE 1: Ionization energy $\epsilon(0/-)$ and formation energy ΔH_f of defect complexes in ZnS.

	$2N_S-Al_{Zn}$	$2N_S-Ga_{Zn}$	$2N_S-In_{Zn}$	N_S
$\epsilon(0/-)$ (meV)	40.1	37.5	44.1	103.9
ΔH_f (eV)	3.04	3.17	3.16	3.35

of ZnS (2N, Al). We observe that a narrow band forms near VBM in ZnS (N) due to the large electronegativity of N comparing with that of S. The localization of DOS for N atom results in high formation energy. Meanwhile, the N-impurity bandwidth in ZnS (2N, Al) is increased due to the interaction of N-p and Al-p orbitals, which indicates that the defect is easily formed. Therefore, we can see that the codoping using N as an acceptor and III elements (Al, Ga, and In) as reactive-codopant donor is very effective for materials design to obtain low-resistivity and high-concentration p-type ZnS.

4. Conclusion

In summary, our first principles calculations reveal that the codoping method with two acceptors and one donor is effective to realize low-resistivity and high carrier concentration p-type ZnS with WZ structure. The ionization energy of single N_S can be lowered by introducing the $III_{Zn}-N_S$ passivation system due to the acceptor transition between the N level and the IBM rather than the VBM. The codoping method in ZnS (2N, III) has lower formation energy compared with single doping of N since III elements act as reactive codopants with N.

Acknowledgment

The authors acknowledge financial support from the Key Program of the Natural Science Foundation of Chongqing (cstc2012jjB50010).

References

- [1] S.-H. Wei, "Overcoming the doping bottleneck in semiconductors," *Computational Materials Science*, vol. 30, no. 3-4, pp. 337-348, 2004.
- [2] S. Nakamura, J. Yamaguchi, S. Takagimoto, Y. Yamada, and T. Taguchi, "Luminescence properties of lithium-doped ZnS epitaxial layers grown by MOCVD," *Journal of Crystal Growth*, vol. 237-239, no. 1-4, pp. 1570-1574, 2002.
- [3] Y. Gai, J. Li, B. Yao, and J.-B. Xia, "The bipolar doping of ZnS via native defects and external dopants," *Journal of Applied Physics*, vol. 105, no. 11, Article ID 113704, 2009.
- [4] Y. Yan, J. Li, S.-H. Wei, and M. M. Al-Jassim, "Possible approach to overcome the doping asymmetry in wideband gap semiconductors," *Physical Review Letters*, vol. 98, no. 13, Article ID 135506, 2007.
- [5] O. K. Echendu, A. R. Weerasinghe, D. G. Diso, F. Fauzi, and I. M. Dharmadasa, "Characterization of n-Type and p-Type ZnS Thin Layers Grown by an Electrochemical Method," *Journal of Electronic Materials*, vol. 42, no. 4, pp. 692-700, 2013.
- [6] Y. Gai, J. Li, S.-S. Li, J.-B. Xia, Y. Yan, and S.-H. Wei, "Design of shallow acceptors in ZnO through compensated donor-acceptor complexes: a density functional calculation," *Physical Review B*, vol. 80, no. 15, Article ID 153201, 2009.
- [7] M. Kumar, T.-H. Kim, S.-S. Kim, and B.-T. Lee, "Growth of epitaxial p-type ZnO thin films by codoping of Ga and N," *Applied Physics Letters*, vol. 89, no. 11, Article ID 112103, 2006.
- [8] L. Svob, C. Thiandoume, A. Lussou, M. Bouanani, Y. Marfaing, and O. Gorochov, "p-type doping with N and Li acceptors of ZnS grown by metalorganic vapor phase epitaxy," *Applied Physics Letters*, vol. 76, no. 13, pp. 1695-1697, 2000.
- [9] T. Yamamoto, S. Kishimoto, and S. Iida, "Control of valence states for ZnS by triple-codoping method," *Physica B*, vol. 308-310, pp. 916-919, 2001.
- [10] T. Yamamoto, S. Kishimoto, and S. Iida, "Materials design for p-type ZnS with blue Ag emission by triple-codoping method," *Physica Status Solidi*, vol. 229, no. 1, pp. 371-375, 2002.
- [11] S.-Z. Li, J.-C. Liu, X.-D. Yang, and D.-Q. Jiang, "First-principles study of Al, N codoped p-type ZnS," *Chinese Journal of High Pressure Physics*, vol. 25, no. 6, pp. 519-525, 2011.
- [12] X. Ma, "Study of the P-type doping properties of ZnS nanocrystals," *Journal of Nanomaterials*, vol. 2011, Article ID 952616, 5 pages, 2011.
- [13] G. Kresse and D. Joubert, "From ultrasoft pseudopotentials to the projector augmented-wave method," *Physical Review B*, vol. 59, no. 3, pp. 1758-1775, 1999.
- [14] J. P. Perdew and W. Yue, "Accurate and simple density functional for the electronic exchange energy: generalized gradient approximation," *Physical Review B*, vol. 33, no. 12, pp. 8800-8802, 1986.
- [15] G. Kresse and J. Furthmüller, "Efficiency of ab-initio total energy calculations for metals and semiconductors using a plane-wave basis set," *Computational Materials Science*, vol. 6, no. 1, pp. 15-50, 1996.

- [16] J. D. Pack and H. J. Monkhorst, "Special points for Brillouin-zone integrations," *Physical Review B*, vol. 13, no. 12, pp. 5188–5192, 1976.
- [17] Y. Yan and S.-H. Wei, "Doping asymmetry in wide-bandgap semiconductors: origins and solutions," *Physica Status Solidi*, vol. 245, no. 4, pp. 641–652, 2008.

Research Article

Studies on AC Electrical Conductivity of CdCl₂ Doped PVA Polymer Electrolyte

M. B. Nanda Prakash,¹ A. Manjunath,² and R. Somashekar¹

¹ Department of Studies in Physics, University of Mysore, Manasagangotri, Mysore, Karnataka 570006, India

² Department of Studies in Physics, Government Science College, Chitradurga, Karnataka 577501, India

Correspondence should be addressed to R. Somashekar; rs@physics.uni-mysore.ac.in

Received 18 May 2013; Revised 5 July 2013; Accepted 9 July 2013

Academic Editor: Liang Qiao

Copyright © 2013 M. B. Nanda Prakash et al. This is an open access article distributed under the Creative Commons Attribution License, which permits unrestricted use, distribution, and reproduction in any medium, provided the original work is properly cited.

PVA-based polymer electrolytes were prepared with various concentrations of CdCl₂ using solvent casting method. Prepared polymer films were investigated using line profile analysis employing X-ray diffraction (XRD) data. XRD results show that the crystallite size decreases and then increases with increase in CdCl₂. AC conductivity in these polymer increases films first and then decreases. These observations are in agreement with XRD results. The highest ionic conductivity of $1.68E-08 \text{ Scm}^{-1}$ was observed in 4% of CdCl₂ in PVA polymer blend. Crystallite ellipsoids for different concentrations of CdCl₂ are computed here using whole pattern powder fitting (WPPF) indicating that crystallite area decreases with increase in the ionic conductivity.

1. Introduction

There is a continued interest in conducting polymers due to their properties like easy fabrication, low cost, leak proof, biodegradability, and good storage capacity. Conducting polymers find application in the development of advanced high energy electrochemical devices for example, batteries, fuel cells, electrochemical display devices, and photoelectrochemical cells. The development of conducting polymers involves several approaches: (i) dry solid state polymers, (ii) gel/plasticizer polymer, and (iii) composite polymer. Many lithium-based polymer electrochemical systems have been investigated earlier [1]. In our study we have chosen poly vinyl alcohol (PVA) as a host polymer doped with cadmium chloride (CdCl₂) for preparing polymer electrolytes. PVA is a water soluble polymer and has several interesting physical properties. PVA is having a good charge storage capacity and dopant-dependent electrical and optical properties [2, 3]. PVA is a semicrystalline polymer. Cadmium chloride is a white crystalline compound. It is a hygroscopic solid that is soluble in water. Cadmium chloride is also used for photocopying, dyeing, and electroplating.

The present study focused on the AC electrical conductivity of PVA doped with CdCl₂ blends which will be an

interesting study for being used as a final product in some technical applications like electrochemical applications, fuel cells, batteries, electrochemical display devices, and photoelectrochemical cells. The present study is also concerned with the correlation between crystallite ellipsoids and conductivity in CdCl₂-based polymer films. An explanation in terms of C–O and C–H bond stretching using FTIR data has been made in this paper. FTIR spectra are useful in identifying the change in functional groups due to the presence of cadmium ions. Cadmium ions have a tendency to break polymer network because of its reasonable positive charge behaviour which is indicated in our FTIR studies.

2. Experimental

2.1. Sample Preparation. Poly vinyl alcohol (PVA) was purchased from Loba Chemie, Mumbai, India, and was used without further purification. CdCl₂ was purchased from M/s SD fine chemicals, Bangalore, Karnataka, India. The polymer films were prepared by solvent casting method [4] for various concentrations of salt. The films were dried at room temperature for at least 7 days. The thicknesses of the films were 10 microns.

TABLE 1: Microstructural parameters of CdCl₂ doped with PVA polymer using exponential distribution function.

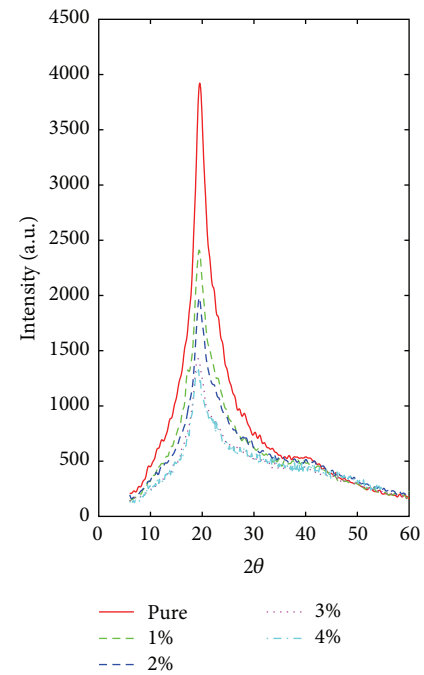
Samples	Bragg's reflections (hkl)	2θ (Deg)	<i>g</i> (%)	Surface density (S)/(nm) ²	⟨ <i>N</i> ⟩	<i>D_s</i> (nm)	α	Delta	Crystallite area (nm ²)
Pure	(012)	19.56	1.35	4.47	3.9	1.76	0.52	2.11E - 3	1.39
	(321)	41.56	1.35	2.14	3.65	0.79	0.73		
1%	(021)	19.40	1.35	4.51	4.05	1.85	0.47	2.39E - 3	1.32
	(114)	38.48	1.35	2.30	3.07	0.71	0.89		
2%	(012)	19.56	1.35	4.47	4.17	1.88	0.45	3.13E - 3	1.16
	(321)	41.46	1.35	2.14	2.85	0.61	1.24		
3%	(021)	19.24	1.35	4.54	3.66	1.68	0.56	3.12E - 3	1.07
	(114)	38.54	1.35	2.30	2.75	0.64	1.33		
4%	(021)	19.02	1.5	4.60	3.94	1.83	0.52	2.07E - 3	1.20
	(311)	37.24	1.5	2.38	2.73	0.65	1.20		

2.2. *X-Ray Diffraction Recordings.* X-ray diffraction patterns of the polymer films were recorded using Rigaku MiniFlex II Diffractometer with Ni filtered CuK α radiation of wavelength 1.5406Å and a graphite monochromator. The specifications used for the recordings are 30 kV and 15 mA. The polymer films were scanned in continuous mode in the 2θ range of 5°–60° with a scanning speed of 5°/min and step size of 0.02°.

2.3. *AC Conductivity and FTIR Measurement.* The AC conductivity of these polymer films was measured using Hioki (Japan) model 3532–50 computer interfaced digital LCR meter in the range of 50 Hz–5 MHz. The infrared spectra of these polymer films were recorded at room temperature in the (wave number) range of 4000 cm⁻¹ to 400 cm⁻¹ using JASCO FTIR 4100 type A spectrometer.

3. Results and Discussion

3.1. *X-Ray Diffraction Studies.* X-ray diffraction analysis is a very useful method in determining the microstructure of the material. The microstructural parameters like crystal size (⟨*N*⟩) and lattice strain (*g*) in polymer films were investigated by line profile analysis [5]. These studies also emphasize upon the importance of line profile analysis [6] and suggest that single-order method is a reasonably good approach to obtain microstructural parameters [7, 8]. The XRD pattern of pure PVA and CdCl₂ complexed PVA films is shown in Figure 1. From Figure 1, we observe a Bragg peak at 2θ = 19.56°. In salt added films, the intensity of the peak is found to decrease and width increases. This indicates that the addition of CdCl₂ salt causes a decrease in the degree of crystallinity of the polymer PVA up to a certain concentration and then increases. A casual glance at Table 1 indicates that the crystallite area decreases by 23% with the addition of CdCl₂ salt. This suggests that on the complementary side amorphous region has increased. This decrease is due to the amorphous nature of the film. The correlation between the intensity of the peak and the degree of the crystallinity is established by Hodge et al. [9]. We have developed in-house program for computation of crystallite size and lattice strain by simulating the whole powder pattern fitting and the details of the procedure are given in our earlier paper [10]. The simulated whole powder patterns

FIGURE 1: XRD pattern of pure PVA and (PVA + CdCl₂) polymer films.

of these polymer electrolytes are given in Figure 2. These microstructural parameters are given in Table 1. It is evident from Table 1 that crystallite size is different in different Bragg directions. Recently Leonardi et al. have remarked that the crystallite size is different along different Bragg angles [11]. In order to get a better perspective and understanding of these microstructural parameters, we have used cell parameters of PVA reported earlier [12] to plot unit cell crystallite shape using all the reported (hkl) reflections. With this crystallite which has a centre, we have plotted crystallite size (*D* in nm) for the two Bragg reflections (012) and (321) in Figure 3 which is not drawn to scale. This figure indicates the crystallite size and shape along various Bragg directions. Furthermore a lattice strain (*g* in %) given in Table 1 implies that a distance of *D* in nm along a direction perpendicular to Bragg plane results in a change in lattice spacing of this percentage.

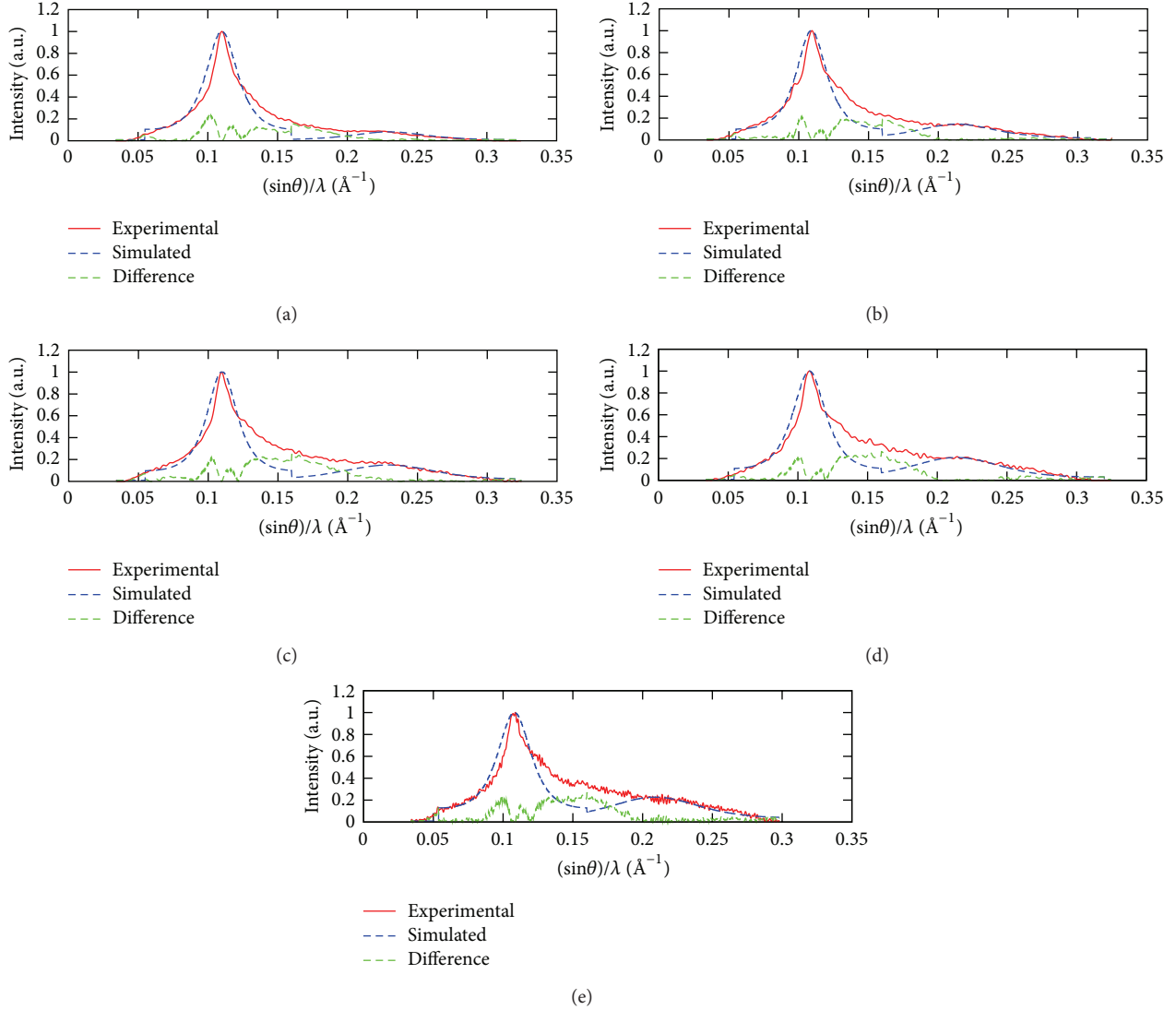


FIGURE 2: Experimental and simulated profiles using whole powder pattern fitting method.

With this understanding, we have projected the variation in crystallite size along different Bragg directions onto a plane for various CdCl_2 doped PVA polymer electrolytes which is given in Figure 4. It is evident from Figure 4 that the crystallite area decreases with increase in concentrations of CdCl_2 [13]. In Table 1, $\langle N \rangle$ indicates average number of unit cells counted in a direction perpendicular to the Bragg plane participating in the scattering process which is relatively small compared to perfect crystals. Furthermore, Table 1 also indicates that S (number of atoms/area = d_{hkl} /volume of the unit cell) increases on an average with the concentration of CdCl_2 for both the Bragg reflections. Alpha given in Table 1 determines the width of the crystallite distribution function used to simulate the whole powder patterns for these polymer electrolytes.

3.2. AC Conductivity and FTIR Analysis. The measured conductance $G(\omega)$ from 50 Hz to 5 MHz was used to

calculate the AC conductivity of the sample using the relation

$$\sigma = \frac{G(\omega)d}{A}, \quad (1)$$

where $G(\omega)$ is the measured conductance, A is the area of the sample, and d is the thickness of the sample. The variation of AC conductivity as a function of frequency for PVA composition of (PVA + CdCl_2) polymer electrolyte is shown in Figure 5. From Figure 5, it is observed that conductivity increases with increase in frequency. The increase in AC conductivity is due to increase in the composition of the salt in polymer matrix resulting in relatively more number of free ions. This will increase the mobile charge carriers as observed in Table 2. These charge carriers move in the amorphous polymer matrix and hence the conductivity increases. Thus there is a relation between the amorphous nature of the polymer film and the conductivity. In general, conductivity

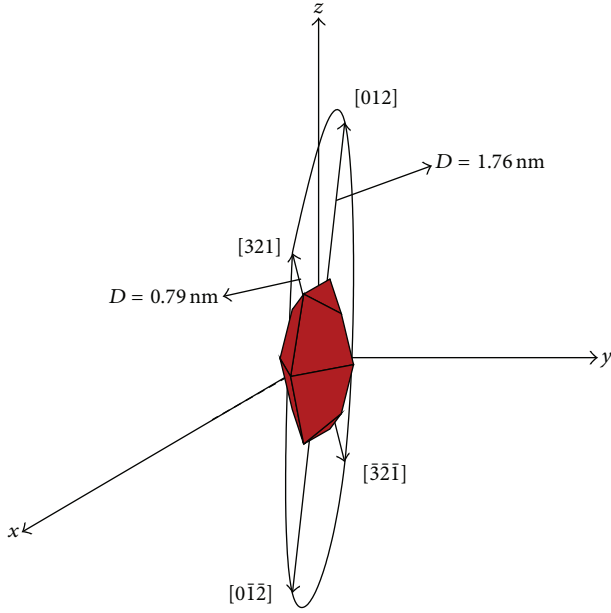


FIGURE 3: Unit cell crystallite shape and crystallite size along different Bragg angles.

TABLE 2: Microstructural parameters of CdCl₂ doped PVA films.

Sample	Crystallite size (D_s in Å)	Conductivity (Scm^{-1})
Pure PVA	1.76	$2.26E - 10$
	0.79	
1% CdCl ₂	1.85	$5.36E - 9$
	0.71	
2% CdCl ₂	1.88	$7.22E - 9$
	0.61	
3% CdCl ₂	1.68	$0.375E - 9$
	0.64	
4% CdCl ₂	1.83	$1.63E - 8$
	0.65	

increases as the degree of crystallinity decreases, as observed above, which is the compliment of increase in amorphous nature [14].

The recorded FTIR spectra are shown in Figure 6. From IR spectra, we have considered a few prominent bands around 3450 cm^{-1} which correspond to O-H stretching of the hydroxyl groups of PVA. Around 1200 cm^{-1} the bands corresponds to stretching of C-O groups. For pure PVA, the fundamental and first overtone transition of C-O bonds is centered at 1994 cm^{-1} and 3830 cm^{-1} , respectively. The nature of chemical bonds in polymers can be studied through the characterization of the vibration modes by infrared spectroscopy [15]. The equilibrium vibration frequency of this bond is calculated using the following relations [16].

Frequency of the fundamental transition = 1944 cm^{-1}

$$= \bar{\nu}_e - 2\chi_e \bar{\nu}_e. \quad (2)$$

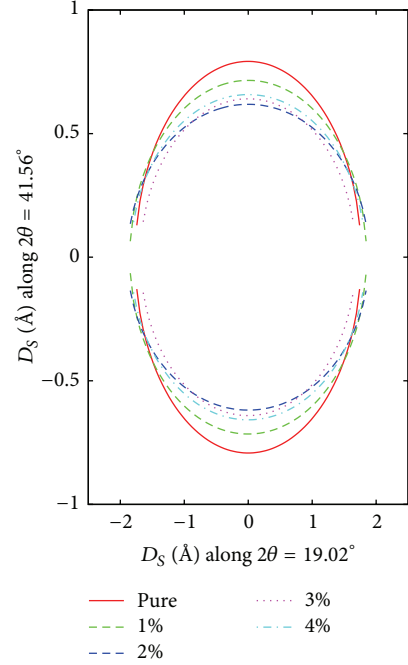


FIGURE 4: Crystallite ellipsoids in (PVA + CdCl₂) based polymer films. 1out: 1% CdCl₂, 2out: 2% CdCl₂, 3out: 3% CdCl₂; 4out: 4% CdCl₂; pureout: pure PVA.

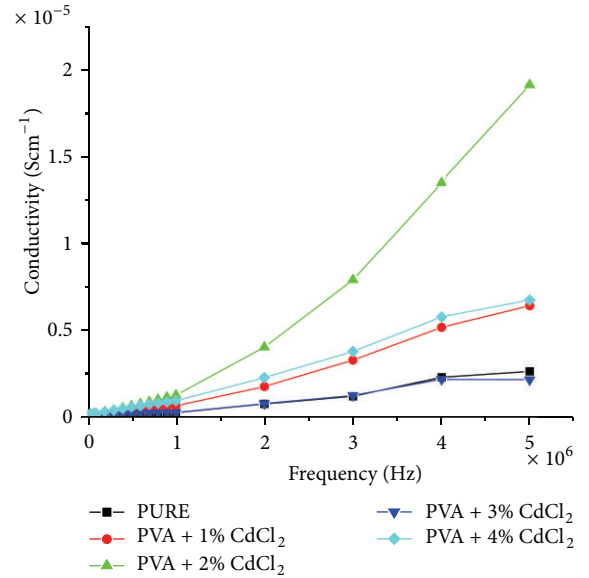


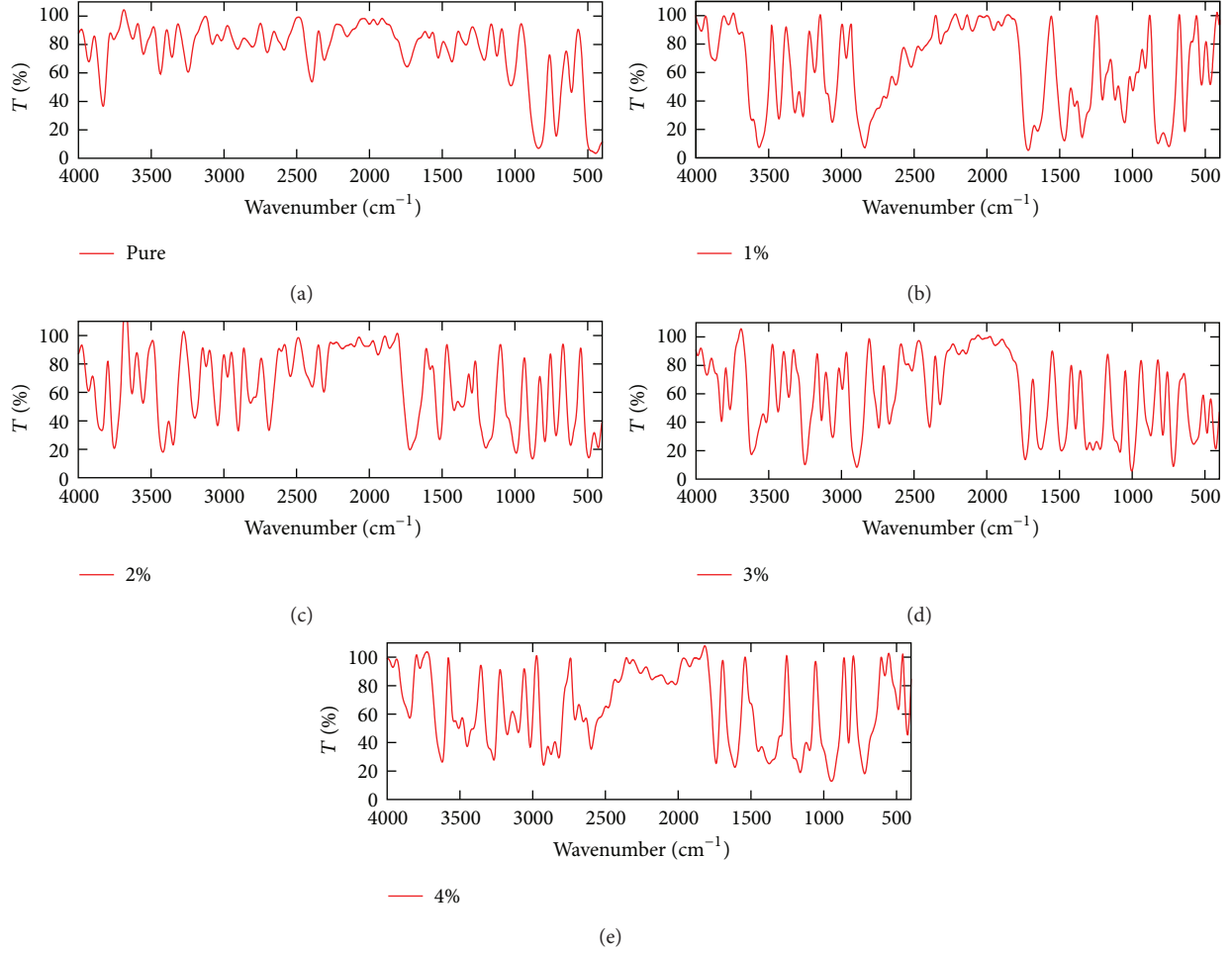
FIGURE 5: Variation of conductivity with frequency.

Frequency of the first overtone = 3830 cm^{-1}

$$= 2\bar{\nu}_e - 6\chi_e \bar{\nu}_e, \quad (3)$$

where $\bar{\nu}_e$ is the equilibrium vibration frequency and χ_e is the anharmonicity constant.

Solving these two equations, we get equilibrium vibration frequency and hence we can calculate anharmonicity constant. For pure PVA, the calculated equilibrium vibration

FIGURE 6: FTIR spectrum of pure PVA and various concentrations of CdCl_2 polymer films.TABLE 3: IR data of pure and CdCl_2 doped PVA polymer films.

Samples	Equilibrium vibration frequency ν_e (cm^{-1})	Anharmonicity constant χ_e (10^{-3})	ϵ_o (cm^{-1})	Force constant k (N/m)
Pure	2002	14.48	998.7	222.2
1% CdCl_2	1988	9.05	989.5	219.1
2% CdCl_2	1982	10.59	985.7	217.7
3% CdCl_2	1999	14.50	998.2	221.5
4% CdCl_2	1931	1.55	964.7	206.7

frequency and anharmonicity constant are 2002 cm^{-1} and 14.48×10^{-3} . The equilibrium vibration frequency decreases for various concentrations of CdCl_2 salt. Zero point energy is calculated for these samples using the following relation [16]:

$$\epsilon_o = \frac{1}{2} \bar{\nu}_e \left(1 - \frac{\chi_e}{2} \right). \quad (4)$$

The zero point for pure PVA sample is 993.7 cm^{-1} and it decreases for various concentrations of CdCl_2 salt. The force constant for all the samples is calculated using the following relation:

$$k = 4\pi^2 \mu c^2 \bar{\nu}_e^2, \quad (5)$$

where μ is the reduced mass of the system and c is the velocity of light. The calculated force constant for pure PVA is 222.2 Nm^{-1} and it decreases for various concentrations of CdCl_2 salt. The calculated values of equilibrium vibration frequency, anharmonicity constant, zero point energy, and force constant for pure PVA and for various concentrations are tabulated as shown in Table 3. It is evident from Table 3 that equilibrium vibrational frequency, anharmonicity constant, force constant, and zero point energy decrease with increase in CdCl_2 . This is due to interaction of the dopant with the polymer chain mainly with the hydroxyl group as observed in FTIR spectrum which results in more amorphous structure.

4. Conclusion

Polymer blend electrolytes were prepared with PVA for different concentrations of CdCl_2 and we observe the highest conductivity of $1.68E-08 \text{ Scm}^{-1}$ using solution casting technique at room temperature. Such polymer electrolyte is suitable for storing devices like batteries and other applications. XRD studies show complete complexation of CdCl_2 salt in the polymer network. Furthermore, for the first time we have presented unit cell crystallite shape and crystallite sizes for different Bragg reflections. From this study, we observe that the conductivity and XRD results are complementary to each other. With concentration, conductivity at 1 kHz increases, whereas on average the crystallite area decreases. This is in conformity with the earlier studies [17] wherein the authors mention that this is due to the inversion centre in polymer network which is created by the inorganic molecule CdCl_2 which reduces the overall crystalline domains in these polymer blends. These polymer films are also suitable for the use in electrochemical applications. IR studies also support this view.

Acknowledgment

The authors would like to thank UGC, India, for the grants under Centre with Potential of Excellence in Particular Area (CPEPA) and University for Potential of Excellence (UPE) research program for the University of Mysore, Mysore, Karnataka, India.

References

- [1] S. K. Tripathi, "Ashish gupta and Manju kumara," *Bulletin of Materials Science*, vol. 35, no. 6, pp. 969–975, 2012.
- [2] C. Uma Devi, A. K. Sharma, and V. V. R. Narasimha Rao, "Electrical and optical properties of pure and silver nitrate-doped polyvinyl alcohol films," *Materials Letters*, vol. 56, no. 3, pp. 167–174, 2002.
- [3] A. Krkljes, J. M. Nedeljkovic, and Z. Kacarevic-Popovic, "Fabrication of Ag-PVA hydrogel nanocomposite by γ -irradiation," *Polymer Bulletin*, vol. 58, no. 1, pp. 271–279, 2007.
- [4] T. Tanabe, N. Okitsu, A. Tachibana, and K. Yamauchi, "Preparation and characterization of keratin-chitosan composite film," *Biomaterials*, vol. 23, no. 3, pp. 817–825, 2002.
- [5] S. Divakara, S. Madhu, and R. Somashekar, "Stacking faults and microstructural parameters in non-mulberry silk fibres," *Pramana*, vol. 73, no. 5, pp. 927–938, 2009.
- [6] I. H. Hall and R. Somashekar, "Determination of crystal size and disorder from the X-ray diffraction photograph of polymer fibres. 2. modelling intensity profiles," *Journal of Applied Crystallography*, vol. 24, no. 6, pp. 1051–1059, 1991.
- [7] R. Somashekar, I. H. Hall, and P. D. Carr, "The determination of crystal size and disorder from X-ray diffraction photographs of polymer fibres.1. The accuracy of determination of Fourier coefficients of the intensity profile of a reflection," *Journal of Applied Crystallography*, vol. 22, pp. 363–371, 1989.
- [8] R. Somashekar and H. Somashekarappa, "X-ray diffraction-line broadening analysis: paracrystalline method," *Journal of Applied Crystallography*, vol. 30, no. 2, pp. 147–152, 1997.
- [9] R. M. Hodge, G. H. Edward, and G. P. Simon, "Water absorption and states of water in semicrystalline poly(vinyl alcohol) films," *Polymer*, vol. 37, no. 8, pp. 1371–1376, 1996.
- [10] S. Divakara, G. N. Siddaraju, and R. Somashekar, "Comparative study of natural and man-made polymers using whole powder pattern fitting technique," *Fibers and Polymers*, vol. 11, no. 6, pp. 861–868, 2010.
- [11] A. Leonardi, M. Leoni, S. Siboni, and P. Scardi, "Common volume functions and diffraction line profiles of polyhedral domains," *Journal of Applied Crystallography*, vol. 45, no. 6, pp. 1162–1172, 2012.
- [12] B. G. Colvin, "Crystal structure of polyvinyl alcohol," *Nature*, vol. 248, no. 5451, pp. 756–759, 1974.
- [13] H. Somashekarappa, S. S. Mahesh, R. Somashekar, and S. Sangappa, "Variation in crystallite shape ellipsoid in non-mulberry silk fibres," *Indian Journal of Fibre and Textile Research*, vol. 30, no. 3, pp. 309–314, 2005.
- [14] W. H. Hou, C. Y. Chen, and C. C. Wang, "Conductivity, DSC, and solid-state NMR studies of comb-like polymer electrolyte with a chelating functional group," *Solid State Ionics*, vol. 166, no. 3–4, pp. 397–405, 2004.
- [15] J. Davenas, X. L. Xu, G. Boiteux, and D. Sage, "Relation between structure and electronic properties of ion irradiated polymers," *Nuclear Instruments and Methods in Physics Research B*, vol. 39, no. 1–4, pp. 754–763, 1989.
- [16] G. Aruldas, *Molecular Structure and Spectroscopy*, Prentice-Hall of India, New Delhi, India, 2004.
- [17] L. C. Gui, F. S. Li, Z. M. Cen, X. J. Wang, and B. Li, "A coordination polymer of CdCl_2 with the novel zwitterionic dicarboxyl-ate ligand 2,2'-(2-methyl-benzimid-azol-ium-1,3-di-yl)diacetate (pda)," *Acta Crystallographica C*, vol. 64, no. 11, pp. m378–m380, 2008.